Copyright Declaration

Imperial College of Science, Technology and Medicine
Department of Chemical Engineering

Dynamics of Thin Liquid Films over a Spinning Disk

Kun Zhao

Submitted in part fulfilment of the requirements for the Imperial College degree of
Doctor of Philosophy in Chemical Engineering, January 2018

Dedication

The thesis is dedicated to my parents, wife, friends and all the wonderful things in my life...

‘The enchanting charms of this sublime science reveal only to those who have the courage to go deeply into it.’

Carl Friedrich Gauss

Statement of Originality

The work presented in this dissertation has been carried out at Imperial College between Nov 2013 and November 2017, under the supervision and guidance of Professor Omar K. Matar. I hereby declare that, except where previous work is acknowledged or stated otherwise, this thesis is a result of my own original research and that no parts of it have been submitted for a degree or any other qualification at Imperial College or any other institution.

Acknowledgements

First of all, I would like to express my ultimate gratitude to my supervisor, Professors Omar K Matar. Without his expertise, experience, patience guidance and constant encouragement, this thesis, amongst other commitments during my PhD study, could not have been achieved. He has given me endless opportunities to present and disseminate my work and have helped guide and critique it at every step. I fervently hope that the contents of this dissertation stand up to their exacting standards.

I also would like to thank my colleagues in Matar's Fluid Group, especially Dr Alex Wray and Dr Junfeng Yang. I was very fortunate to talk with them and learn the mathematics, numerical solutions and industrial applications involved with fluid dynamics. This has been an asset to me which is highly valuable.

Finally, my specific thanks to my parents and wife, who have been extraordinarily thoughtful and helpful during my life as a PhD. They have aided me in every aspect of my life, physically, emotionally and financially.

Abstract

Thin film dynamics over spinning disks is of central importance to a number of scientific research and industrial applications, such as heat/mass transfer, chemical reactions and chip devices. Although they have received a lot of attention in different applications, the key underlying dynamics governing the flow are not thoroughly understood, especially in terms of highly non-linear behaviour in free surface flows, in the presence of other physical forces or chemical reactions. The elucidation of the underlying mechanisms driving the flow is of utmost importance to both scientific research and industrial applications.

In this research the dynamics of a thin film flowing over a rapidly spinning, horizontal disk, in presence of first-order chemical reactions is considered. A set of non-axisymmetric evolution equations for the film thickness, radial and azimuthal flow rates is derived using a boundary-layer (IBL) approximation in conjunction with the Karman-Polhausen approximation for the velocity distribution in the film. Numerical solutions of these highly nonlinear partial differential equations are obtained from finite difference scheme which reveals the formation of large-amplitude waves that travel from the disk inlet to its periphery. The equations with non-axisymmetric condition were investigated where elimination of azimuthal dependence presents different wave regimes across the disk radius, and three dimensional wave structures over the entire disk. Apart from hydrodynamics, the influence of these waves on the concentration and temperature profiles is analysed for a wide range of system parameters. It is shown that these waves lead to significant enhancement of the rates of heat and mass transfer, as well as chemical reaction due to the mixing associated with the flow.

Additionally, due to the time-consuming implementation of the IBL model, the Neural Network (NN) technique is applied based on existing Finite Difference (FD) results, in order to predict the wave dynamics after initial times.The NN is trained on a dataset from various data points in space and time from IBL model, and then used to simulate the evolution of any wave characteristics of interest. Overall, the resulting NN model predicts the evolution of waves reasonably well when compared with the time-consuming finite difference scheme, and reduces the computation time significantly.

Contents

List of Tables

List of Figures

Nomenclature

Greek Symbols

α	Parameter controlling distance between spiral loop in Archimedean equation
α_1, α_2, $\beta_{11} - \beta_{51}$	Constant parameters used in the derivation of the IBL equations
β	Spiral deviation from a circle [$\beta = \arctan\left(\frac{1}{r}\frac{dr}{d\theta}\right)$]
ϵ	Aspect ratio [$\epsilon = \frac{H}{R}$]
η	Thermal diffusivity [m^2/s]
γ	Temperature dependence of surface tension [$N/(m \cdot K)$]
ι	Inclination angle of substrate
κ	Curvature [m^{-1}]
λ^2	Modified Weber number [$\lambda^2 = \frac{\sigma H}{\rho \Omega^2 R^4}$]
ν	Kinematic viscosity [m^2/s]
Ω	Rotational speed [rpm]
ω	Rotational speed [rad/s]
ρ	Density [kg/m^3]
σ	Surface tension [N/m]
σ_0	Surface tension scale [N/m]

Θ Dimensionless temperature profile $[\Theta = (T/T_0)(2\zeta - \zeta^2)^{-1}]$

ζ Normalised z coordinate $[\zeta = \frac{z}{h}]$

Roman Letters

ADI Alternating Direction Implicit

ANN Artificial Neural Network

Bi Biot number $[Bi = \frac{H\eta}{k}]$

c Dimensional concentration profile of reactant $[mol/m^3]$

C_0 Characteristic concentration scale $[mol/m^3]$

C_b Dimensionless concentration profile $[C_b = (c/C_0)(1 - \zeta^2)^{-1}]$

C_p Heat capacity $[J/(kg \cdot K)]$

CFD Computational Fluid Dynamics

D Modified Capillary number $[D = (3Ca)^{1/3} \cot \iota]$

D_i Diffusion coefficient $[m^2/s]$

D_o Diameter $[m]$

Da Damkohler number $[Da = k_0 e^{-\frac{E}{RT_0}}]$

DNS Direct Numeric Simulation

E Activation energy for chemical reactions $[kJ]$

f Dimensionless flow rate in radial direction $[f = r \int_0^h u dz]$

FD Finite Difference

g Dimensionless flow rate in azimuthal direction $[g = r \int_0^h v dz]$

H Characteristic thickness scale $[m]$

h Dimensionless film thickness $[h = h_C/H]$

h_C Physical film thickness $[m]$

h_N Film thickness in Nusselt solution $[m]$

I Integral of source term $[I = \int_0^h (c/C_0) e^{\frac{(T/T_0-1)}{T/T_0}} dz]$

IBL Integral Boundary Layer

k Thermal conductivity $[W/(m \cdot K)]$

k_0 Pre-exponential factor $[s^{-1}]$

M Marangoni number $[M = \frac{\gamma T_0 H}{\mu \eta}]$

MW Molecular Weights

NN Neural Network

Nu_{avg} Nusselt number averaged across the disk radius $[Nu_{avg} = \frac{2}{r^2}\left(\int_0^r \left(\frac{\partial \Theta}{\partial z}\right)_{z=0} s ds\right)]$

PDE Partial Differential Equation

Pe Peclet number $[Pe = \frac{\rho \nu C_p}{k}]$

q Additional heat term in energy conservation equation $[J/(m^3 s)]$

Q_C Flow Rate $[m^3/s]$

R Characteristic radius scale $[m]$

R_S Source term $[mol/(m^3 s)]$

R_{disk} Physical disk radius $[m]$

r_{disk} Dimensionless disk radius$[r_{disk} = R_{disk}/R]$

R_{in} Physical inlet radius $[m]$

r_{in} Dimensionless inlet radius $[r_{in} = R_{in}/R]$

Re Reynolds number $[Re = \rho U D_o/\mu]$

$RMSE$ Root Mean Squared Error

Sc Schmidt number $[\ Sc = \frac{\nu}{D_i}]$

SDR Spinning Disk Reactor

Sh_{avg} Sherwood number averaged across the disk radius $[Sh_{avg} = \frac{2}{r^2}\left(\int_0^r \left(\frac{\partial C_b}{\partial z}\right)_{z=0} sds\right)]$

T Dimensional temperature profile of reactant $[K]$

T_0 Characteristic temperature scale $[K]$

U Characteristic velocity scale $[m/s]$

W Dimensionless interfacial waviness $[W = \sqrt{\int_0^{t_{end}} \int_{r_{in}}^{r_{disk}} r(h - h_N)^2 dr dt}]$

Chapter 1

Introduction

1.1 Motivation and Objectives

Thin liquid films are accompanied by large-amplitude waves and complex interfacial dynamics, whether they are falling under gravity [1] or flowing over a spinning disk [2]. Due to the features of thin liquid films, a substantial enhancement of mass and heat transfer can be achieved, which is commonly referred as "process intensification". Thus it is not surprising that such flows can have wide industrial applications, ranging from atomization [3] to spinning disk reactor (SDR) [4] to produce pharmaceuticals and fine chemicals.

The above-mentioned applications lead to immense motivation for experimental, theoretical and numerical studies on the thin film dynamics. And the subject of this thesis was originally motivated by the gap between theoretical research and the experimental studies: while many early experiential research [5, 6, 7] has been conducted on the hydrodynamics and the heat/mass transfer increase due to the mixing effect in the spinning disk reactor, most the the theoretical research focuses on the one-dimensional film thickness and associated heat/mass transfer and chemical reactions [8, 4, 9, 10], instead of non-axisymmetric transient wave evolution profile. This is a surprising absence for a number of reasons. First of all, it is not, mathematically difficult to derive the non-axisymmetric evolution equations as the same geometry and same analytical method (Integral Boundary Layer) are applied. More importantly, this approach

gives us more comprehensive measure of intensification due to the waves generated and also produces results which are then directly used to compare with existing experimental findings e.g. flow structure over the entire disk [6, 7, 11] and measurement of film thickness across the disk [5].

In addition, it is clear that the incorporation of chemical reactions in the theoretical analysis is desirable given that one of the most widely used applications is Spinning Disk Reactor (SDR) and fewer theoretical studies have accounted for the presence of chemical reactions in the flow [12]. Falling film dynamics has drawn attention to most of the researchers: Trevelyan and Kalliadasis [13, 14] show that heat generated from chemical reaction exert influences on the development of thermocapillary stresses. More specifically, an exothermic reaction is stabilizing and dampens the disturbances on the free surface while an endothermic reaction has destabilizing effect. Prieling and Steiner [15, 16] studied the thermal characteristics of thin films over a spinning disk applying the integral boundary layer method. In this research, a comprehensive mathematical model is built for the dynamics of thin film flow over a spinning disk, taking into account the hydrodynamics, mass and heat transfer, chemical reactions (Chapter 5) using integral boundary layer method for coupled differential equations, as well as the extension to non-axisymmetric model with azimuthal dependence (Chapter 4), which are naturally extensions for existing literature, as no researchers have investigated the full three-dimensional Navier-Stokes equation in the spinning disk model and few studies [12] have focused on the modelling the chemical reaction in SDR. Numerical solutions are obtained using the finite difference method in space and time, demonstrating the evolutionary profile of the film thickness, concentration and temperature, indicating the enhancement of heat/mass transfer due to the large-amplitude waves. However, a more comprehensive understanding of chemical reaction within the thin film over spinning disks is desirable, especially taking into account of azimuthal dependency via developing and solving the three-dimensional Navier Stokes, diffusion-convection and energy equations.

Finally, one of the interesting applications is using artificial neural network (ANN) technique to obtain the results from the evolution model. Artificial Neural Network has been used in early literature to solve ordinary and partial differential equations [17] and recently widely

used in assistance with Direct Numerical Simulation result as a much computational cheaper alternative. However, it has not been applied to the IBL model even if the three-dimensional version of IBL model still consumes significant computational resources. Thus, it is of great interest to apply the feedforward neural network to obtain the wave profile using the results from a finite difference numerical scheme, which takes days to compute.

1.2 Outline of Thesis

The thesis is organised as follows:

- Chapter 2 gives a comprehensive overview of existing studies on the subject of thin film dynamics which lays the basis of this thesis.
- Chapter 3 outlines fundamental concepts on lubrication theory and integral boundary layer (IBL) methods followed by the derivation of typical evolution equations of non-axisymmetric thin film flow with chemical reactions.
- Chapter 4 demonstrates the special case when we consider the hydrodynamics of non-axisymmetric thin film flow and associate it with the waves regimes and interfacial waviness studied in earlier literature.
- Chapter 5 studies the one-dimensional dynamics of heat/mass transfer, with the presence of gas-liquid chemical reaction at the interface. This framework is different from previous research, in that the source term in the convection-diffusion equation is exploited with a new set of parametrisation applied where physical impacts are studied.
- In Chapter 6, a modern neural network approach is applied in order to obtain the wave profiles, using the solutions of the coupled partial differential equations which were initially generated by IBL model. Compared to the traditional finite difference numerical approach, neural network provides reliable and less computationally expensive results.

- Finally, in Chapter 7 some concluding remarks and discussions over potential future work are given.

Chapter 2

Background

Thin film flow has drawn huge attention in industry and been studied in a number of theoretical, numerical and experimental researches. This chapter aims to provide background knowledge of thin liquid films and applications, as well as relevant previous studies and research findings, including lower order modelling using lubrication theory (§2.1), thin film over spinning disks (§2.2), and neural network technique (§2.3).

2.1 Thin Film Flows

Thin liquid film flows are accompanied by large-amplitude waves and complex interfacial dynamics whether they are falling under gravity[1] or flowing over a spinning disk[2]. Due to these features of thin liquid films, a substantial enhancement of heat and mass transfer can be achieved, which can be exploited for "process intensification". Thus it is not surprising that such flows can have wide industrial applications [8], ranging from atomization to spinning disk reactors (SDR) used in the production of pharmaceuticals and fine chemicals [4, 10, 18].

In our research, the interest is confined to single-layer, free-surface thin film flow, instead of multi-phase flows. Such systems are a subject of numerous researcher and major reviews papers [19, 20, 21] because of their fascinating behaviour and a wide range of industrial applications.

For example, it is of huge interest to many physicists, mathematicians and engineers to study complex dynamics of thin films, such as formation of regular waves, periodic waves, shocks and fronts, "fingering" behaviour with surfactants [22]. These systems are key to understand many of the physical process, from large-scale avalanches [23] and ice sheets [24], to something as trivial as the blink of eye involving corneal fluid film [25]. Also, they are important in many industrial applications, such as heat and mass transfer enhancement [26], and emerging areas of microfluids [27] and nanofluids [28] technology.

2.1.1 Gravitational effects

One of the main well-studied category of thin film dynamics is the flow of thin films down an inclined plane with gravitational force, which has been widely examined in many experimental and theoretical researches [29, 30, 31, 32]. Inertia effect is a very important factor to take into consideration with regards to the dynamics of falling film. In the region of low Reynolds number, i.e. $Re < 1$, corresponding to weak inertia effects, a flow is predominately driven by viscous forces. At moderate range of Reynolds numbers, $1 < Re < 300$, long interfacial waves emerges due to the combination of capillary and gravitational effects. Within slightly higher range of Reynolds numbers, $300 < Re < 1000$, we observe non-decaying short waves led by long interfacial waves due to vortex shedding mechanism [33]. At higher region of Reynolds number, $Re > 1000$, we find the transition from laminar to turbulent where external pertubations are transformed into internal disturbances due to Tollmien-Schichting waves [20].

The spatial structure of characteristic waves and the effect of inducing disturbance are of particular interest. The pioneering work on falling films was carried out by Kapitza [34] who studied the flow of viscous fluids experimentally. Such flows are associated with the formation of surface waves (as in Fig. 2.1) and can be classified into two categories according to the structures and shape: one includes short-wavelength waves with sinusoidal shapes, the other includes small-amplitude capillary waves.

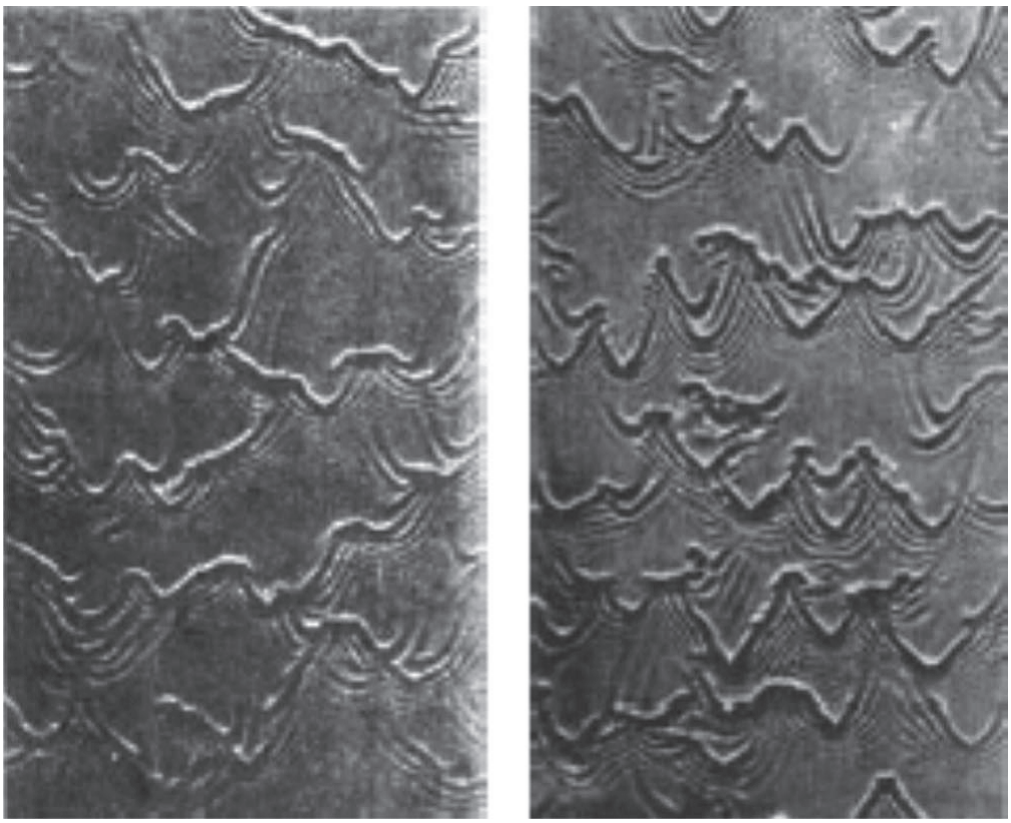

Figure 2.1: Waves formation of water-ethanol mixture falling down an inclined plane, with increasing inertia effect; the Reynolds number is 16 and 45 on the left and right, respectively reproduced from Alekseenko *et al.* [35]

Liu *et al.* [36] demonstrate that the transition between two-dimensional (2-D) structures to three-dimensional (3-D) patterns due to an increased Reynolds number in an experimental study of falling films down an inclined plane. The 2-D waves structures initially emerges and then because the instability of 2D effects grow faster than 3-D, 3-D patterns begin to form. Park *et al.* [37] studied the effect of Reynolds number on the 3-D instabilities: with higher Reynolds number $Re > 1000$, a more rapid onset of such 3D disturbances. Periodical forcing plays an important role in the wave formation downstream, as studied by Alekseenko *et al.* [35], who elucidate that large forcing amplitudes give rise to the formation of large-amplitude waves at the onset, and the wavelength corresponds to the frequency of induced forcing.

From a mathematical point of view, the falling film dynamics have been well studied in the past few decades. Linear stability analysis are often used to predict the system regarding infinitesimal perturbations to base-state flow. For example, consider a differential equation of

the form:

$$\frac{\partial \mathbf{x}}{\partial t} = f(\mathbf{x}) \tag{2.1}$$

The linearlisation of the system at fixed point $\mathbf{x_0}$ where $\mathbf{x} = \mathbf{x_0} + \delta\mathbf{x}$, leading to the matrix system

$$\frac{\partial(\delta \mathbf{x})}{\partial t} = A\,(\delta \mathbf{x}) \tag{2.2}$$

And this will be translated into an eigenvalue problem: if the spectrum matrix $\mathbf{A}$ has any eigenvalue with positive real part, the system is considered linearly unstable; if $\mathbf{A}$ contains eigenvalue with negative real part, we consider the system linearly stable. Otherwise, the system is neutrally stable.

In the case of Navier-Stokes equation in fluid dynamics, the fixed point $\mathbf{x_0}$ corresponds to the base state while the disturbance $\delta\mathbf{x}$ corresponds to perturbation which will grow in time, leading to Orr-Summorfeld (OS) equation [38, 32]. The growth rate is associated with system parameters, such as Reynolds number and wavenumber.

The problem of instability of liquid films flowing down an inclined plane under gravity, has been the focus of the work conducted by Yih [167, 168] and Benjamin [10] who carried out a stability analysis of the waveless solution of the Navier-Stokes equations for a laminar viscous liquid layer. Yih and Benjamin studied the stability of surface waves on liquid films and found that the perturbed base state (obtained from the waveless solution) admits flow instability in the long-wave limit (small wavenumbers). Their analysis also showed that there exists a Reynolds number above which disturbances to the flow are amplified, given by $Re = (5/6)\cot(\theta)$ where θ is the angle of inclination to the horizontal.

The nonlinear behaviour of the thin film system cannot be explained by the linear stability analysis. Therefore, it is desirable to investigate the mechanisms of thin film flow since it is challenging to resolve the full Navier-Stokes equations due to the intractability. A common and useful method towards the analysis of this system, of which we make extensive use in the thesis and on which most of our results are based, is called low order modelling. The essence of this approach is to reduce the dimension of the system, by eliminating the cross-stream co-ordinate,

which leads to significant simplification of original Navier-Stokes equations. Generally, we make use of the disparity between the length scales and come up with a small parameter ϵ, known as aspect ratio or lubrication parameter. In the system of falling film down a plane, $\epsilon = H/L$, where H is the characteristic length in the cross-stream direction (film thickness) and L is the characteristic length scale in the streamwise direction (wavelength). Under the assumption of *long-wave* or *thin film*, the characteristic length scale in streamwise direction is much greater than the thickness, i.e. the system has a small (negligible) aspect ratio ϵ.

Having achieved the long wave equation from the original Navier-Stokes, they can be solved in gradient expansion approach [9], which is one way of regular perturbation. This leads to a uncoupled single evolution equation accounting for interfacial film thickness. For example, Benny [39] started with the leading order equations in ϵ for the dynamics of thin film down an inclined plane in 2-D rectangular coordinate, and applied the appropriate boundary conditions both at wall (no-slip and no-penetration) and interface (kinematic, normal and tangential stress balance), which lead to the final single partial differential equation accounting for the interfacial film thickness h, referred to as the Benny equation:

$$h_t + \left[\frac{h^3}{3} + \epsilon\left(\frac{16Re}{15}h^6 h_x - \frac{2}{3}\cot\theta h^3 h_x + \frac{h^3 h_{xxx}}{3\hat{Ca}}\right)\right]_x = 0 \tag{2.3}$$

where Ca is the Capillary number representing the relative significance of viscous forces versus surface tension across two fluids. Equations of this form are usually referred as Benny Equations. Although it is a decent model to capture the wave dynamics via relatively simple PDE, it suffers finite time "blow-up": the interfacial film thickness will become infinite in finite time.

We note that, through the normal stress balance at the interface, capillary effects, parametrised by Ca, enter the equation in the order of ϵ^2 and it follows that this term would be omitted from the leading order equations implying that mean surface tension effects are small. However, as is often not the case, it is essential to re-scale the capillary number such that it can be retained in the $O(\epsilon)$ equations; the aforementioned boundary conditions and appropriate re-scalings are discussed in further detail in Chapter 3.

In the follow-up study, the approach is to apply the Karman-Poulsman method to the leading order long-wave equations. Under the assumption that velocity profile is assumed parabolic in the film, Shakdov [40] derived a system of partial differential equations accounting for film thickness and volumetric flow rate, by employing the similarity parameter δ. This leads to a coupled partial differential equation in terms of interfacial height h and the volumetric flow rate q

$$h_t + q_x = 0, \tag{2.4}$$

$$q_t + \frac{6}{5}\left(\frac{q^2}{h}\right)_x - \frac{1}{5\delta}\left(hh_{xxx} + h - \frac{q}{h^2}\right) = 0, \tag{2.5}$$

where all the subscripts denote partial derivatives, specifically 'x' and 't' represent differentiation with respect to spatial and temporal coordinate. The similarity parameter defined as $\delta = \left(\rho h_N g^4/\sigma\right)^{1/3}/(45\nu^2)$ was introduced on the basis that in thin films, viscous, capillary and gravitational forces are of the same order [41], h_N is the equilibrium (Nusselt) film thickness, the flow rate q is defined as: $q = \int_0^h u(z)dz$, i.e. integration of stream-wise velocity (u) with respect to the wall normal coordinate (z). Equations (2.4) and (2.5) are a result of boundary layer method and integral theories, with semi-analytical z-dependent streamwise velocity profile, $u(z)$, assumed.

This approach is an improvement because, unlike Eqn. (2.3), the set of PDEs does not exhibit finite time "blow-up" behaviour due to the existence of higher-order terms [42]. Chang [20] concludes that the inclusion of the higher order terms in the reduced equations proves to predict correctly the wave evolution in the film under low Renoalds number $Re < 300$ and can therefore be considered a good approximation to the solution of the full Navier-Stokes equations. However, the theory is subject to the assumption of velocity profile, which is reasonable but not always consistent. This will be discussed in Chapter 4 as we apply similar IBL method to develop the model. An improvement over the IBL model is called Weight Residual Integral Boundary Layer (WRIBL) model by Ruyer-Quil *et al.* [30]. This approach is basically carefully weighing procedure in terms of computation of requisite integrals, together with a separate of variables, leading to a set of evolution equations for interfacial height h, flow rate q, and two subsidiary fields s_1 and s_2 as a measure for deviation of flow profile from parabolic Nusselt

solution. This model proves successful even when extended to three-dimensional model in that: no numerical finite time "blow-up" is exhibited; and the profile speed of solitary wave propagation is in agreement with numerical simulation in the drag-inertia regime (Fig. 2.2).

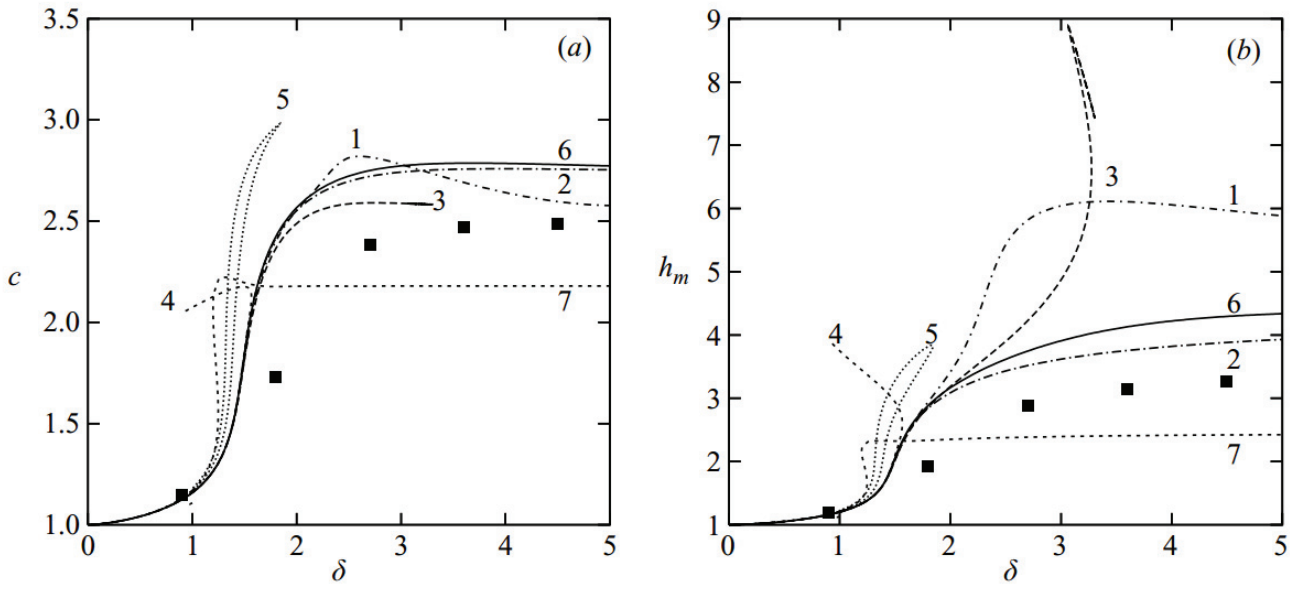

Figure 2.2: Wave speed c (left) and amplitude h_m(right) of the principal orbits as a function of reduced Reynolds number δ (reproduced from Schied *et al.* [9])

Numerical Simulations of the 2D Shkadov equations(2.4) (2.5) describing thin film falling down an inclined plane have also been carried out by Schied *et al.* [9]. They examined the 3D model from 2D and compared with experimental observations carried out by Park and Nosoko [37]. As can be seen from Fig. 2.3, horseshoe-like wave structures due to the interactions between waves were found from the numerical simulations, corresponding to the experimental setup in the study by Park and Nosoko [37].

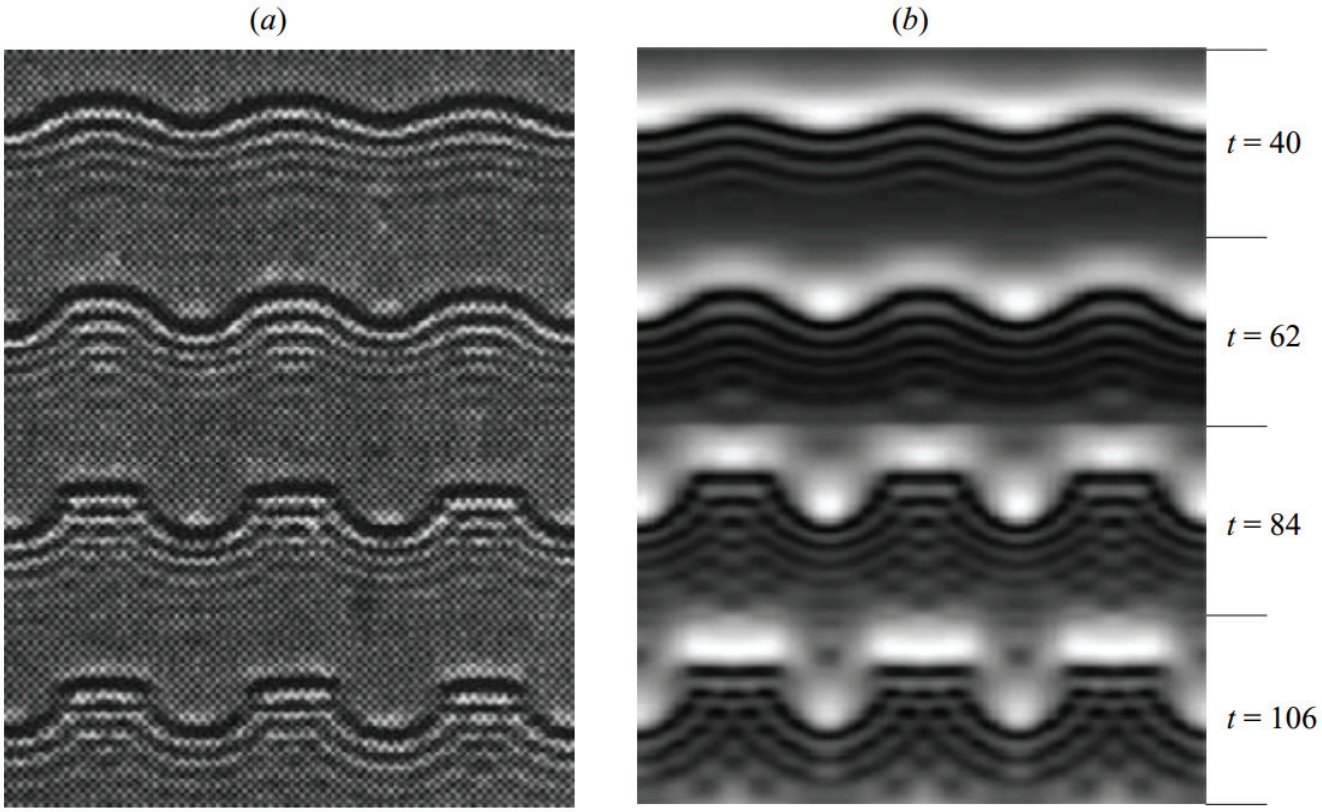

Figure 2.3: A comparison of wave structure between experimental observation (a) and numerical simulation (b) of falling film flow at different times (reproduced from Schied *et al.* [9])

Other dimensionless numbered were studied in the thin film flow. Apart from the inertial effect, viscous forces play an important role in the dynamics of thin film flows. In the cases where viscous forces are dominant, generally in slow-propagating flows, Reynolds numbers may be insignificant and negligible. For $Re << 1$, the governing mass and momentum conservation equations can be simplified significantly to Stokes equation. The viscous fluid flow is subject to the span-wise instabilities, leading to the film break-up into fingers and rivulets. This is an unattractive phenomena in industrial applications, such as coating, since it breaks the continuous and consistent film flow. The theoretical research of this dynamics can also be conducted by applying the long-wave approximation in the leading order equations from the original continuity and Navier-Stokes equations. A simple example in 2-D case (without span-wise dependency) is presented by Kondic *et al.* [43]:

$$h_t + (h^3)_x + \nabla \cdot [h^3 \nabla \nabla^2 h] - D\nabla \cdot [h^3 \nabla h] = 0 \tag{2.6}$$

where the t and x represent partial derivative with respect to temporal and spatial coordinates, $D = (3Ca)^{1/3} \cot \iota$ is a system parameter dependent on Capillary number Ca and incline angle ι of substrate. The 1-D solutions to the equation (2.6) show the formation of a capillary ridge.i.e. travelling wave with a constant velocity as in Fig. 2.4. The amplitude of the waves is dependent on parameter D, which measures the significance of hydrostatic effect. The absence of hydrostatics produces more pronounced waves, where $D = 0$ in panel (a).

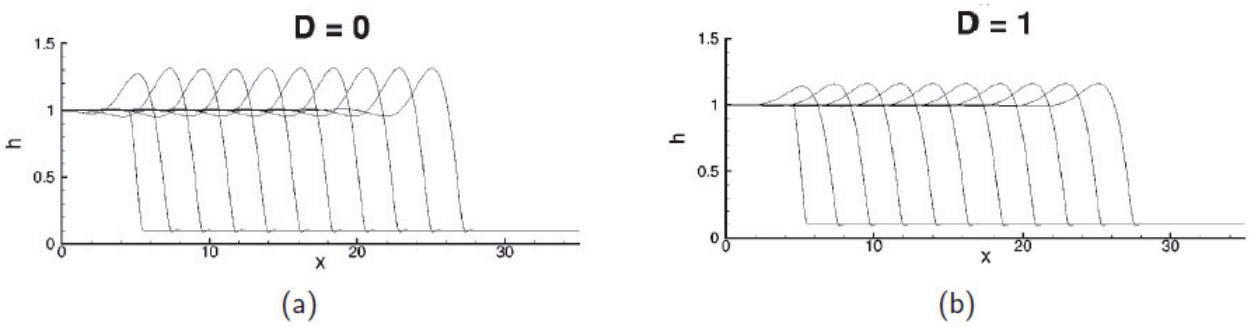

Figure 2.4: 1-D Spatial-temporal evolution of interface a time inteval of 2 dimensionless units, with system paratemer (a) $D = 0$ and (b) $D = 1$ on the capillary ridge, reproduced from [43]

In the engineering applications of thin film under gravity, the fluids of interest often exhibit complex thermal-physical properties, especially the non-Newtonian fluids. The behaviour of these fluids includes flow of lava in geophysical research, shear-thickening, thinning or visco-plastic pattern in coating flow technology [44]. Fingering patterns associated with the flow of visco-plastic fluids exhibit stabilizing effects with higher yield strength, as shown in experiment conducted by Balmforth *et al.* [45]. As can be seen in Fig. 2.5, with increasing concentration of kaolin (visco-plastic fluid) in silicon oil (Newtonian fluid) from top to bottom panels, the wave formation is suppressed and more stable flow is formed by spreading towards the span-wise direction.

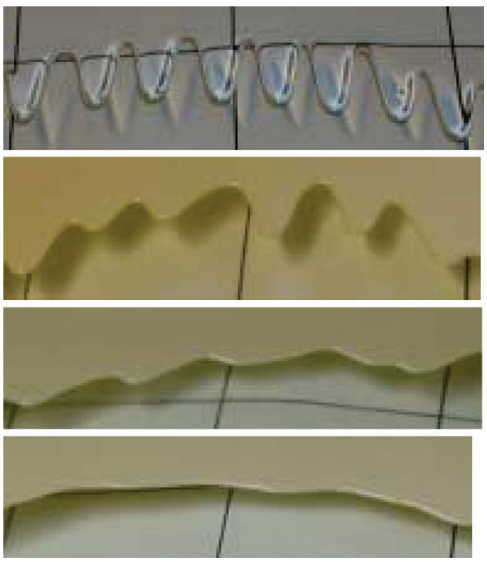

Figure 2.5: Fingering patterns of fluids flowing down an inclined plane(25 degree angle). The topmost fluid is pure silicon oil (Newtonian fluid) and the lower pictures show a mixture of kaolin and silicon oil, with increasing concentration of kaolin from top to bottom (reproduced from Balmforth *et al.* [45])

2.1.2 Thin film over spinning disks

Compared with dynamics of thin film under gravitational force, understanding of the related problem, thin film over spinning disks, and validation of the models against experimental observations have fallen behind, in spite of its widespread applications in industry. This sub-chapter lays the foundation of our theoretical work in this thesis (Chapters 4,5) as it specifically focuses on the flow characteristics over spinning disks.

Similar to falling film dynamics, the film thickness and wave structures have been investigated by early researchers [5, 46, 47, 48]. Espig *et al.* [46] is the first researcher to study the dynamics of thin film flow over a spinning disk experimentally, where they measured the film thickness by applying needles on the waves. Charwat *et al.* [6] have determined the structure of flow field and the existence of several flow regimes. They also studied the wave patterns were related to operating conditions of spinning disk (flow rate of the inlet and rotating speed of the disk) and fluid physical properties (surface tension and viscosity). According to Charwat *et al.* [6] concentric waves were formed under high flow rate and low rotational speed while spiral waves tend to occur under higher rotational speed and low flow rate for the same type of fluid (same

surface tension and viscosity), as seen in Fig. 2.6, which also shows that the transition between wave types is also dependent on the surface tension of fluids (methyl alcohol, iso-proppyl alcohol and water with wetting agent).

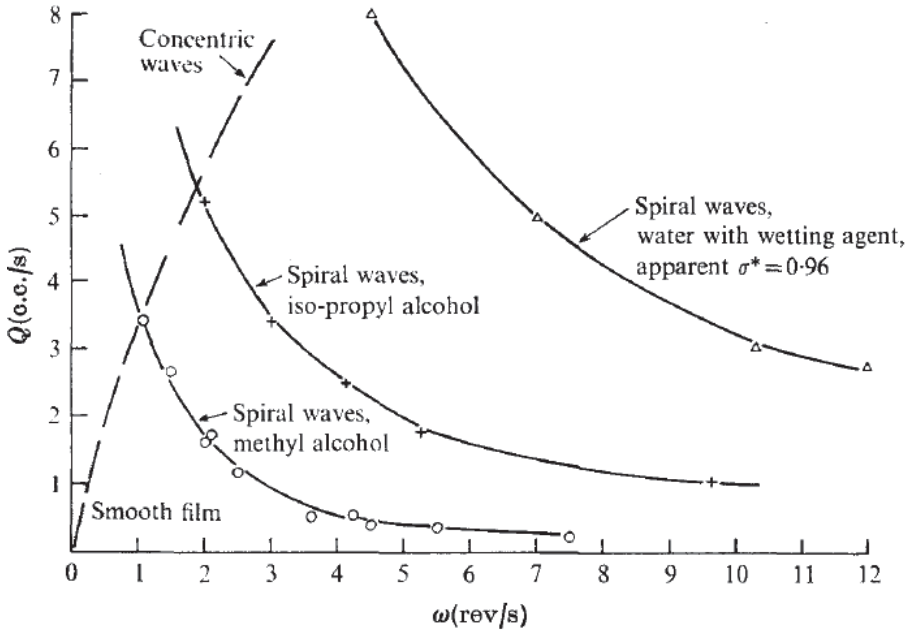

Figure 2.6: Wave regimes of fluids corresponding to different operation conditions: flow rate Q from inlet jet and rotational speed ω (reproduced from Charwat *et al.* [6])

Previous experimental studies involving thin film flows over a spinning disk [5, 46, 47, 48] have determined the structure of flow field and the existence of several flow regimes. Concentric, helical and spiral waves are apparent in the experiments according to [6, 7]. Butuzov and Puhovoi [7] have observed four flow regions across the disk: an inlet region having a smooth film surface (Inlet Region), followed by a region with axisymmetric waves (Region A), which was followed by a turbulent region exhibiting three dimensional travelling waves (Region B); and finally a region of laminar wave where the amplitude of waves decay (Region C), as shown in the schematic (Fig. 2.7)

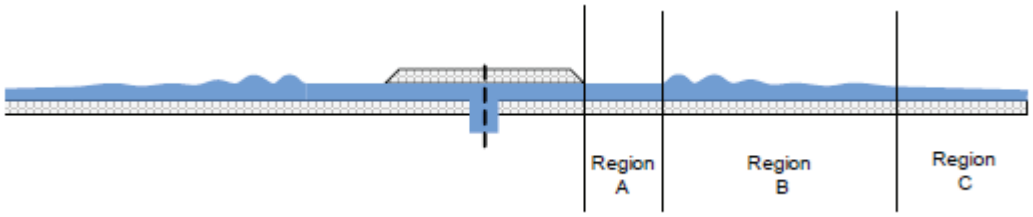

Figure 2.7: Schematic of flow regions from the centre of the disk to its edge [11]

Charwat *et al.* [6] also studied the wave patterns corresponding to different operating conditions and discovered that smooth film tends to occur with low rotating speed and flow rate while higher rotational speed leads to concentric waves and higher flow rate causes spiral waves. Woods [5] investigated extensively the wave formation over a spinning disk by photo-graphic evidence and studied the wave shapes associated with different parameters, as in Fig. 2.8.

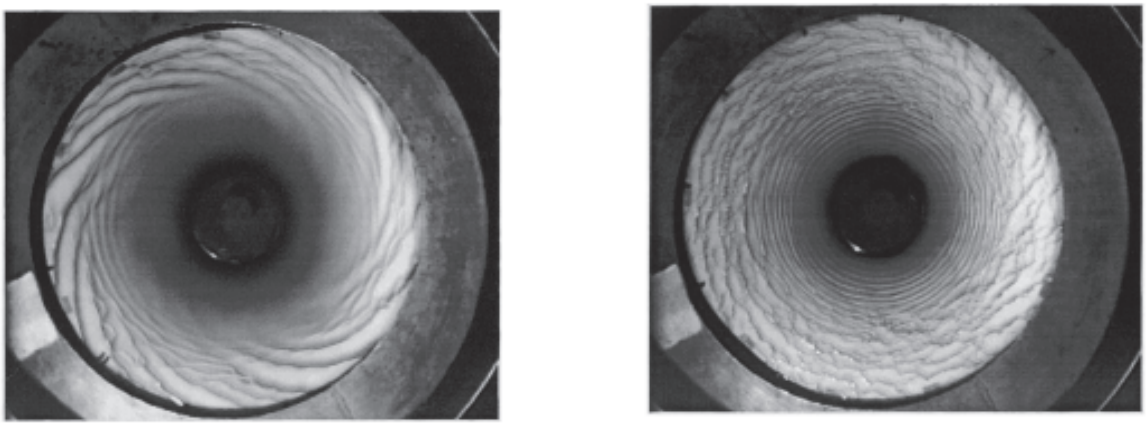

(a) Spiral waves

(b) Concentric waves

Figure 2.8: Wave propagation of thin film over a spinning disk, where the flow rate is 19ml/s and the rotational speed increases from (a) 100 rpm leading to spiral waves to (b) 200 rpm leading to concentric waves in inner region and rivulets at the edge of disk, reproduced from Woods *et al.* [5]

Recent work [11] use high speed camera to show flow characterisations and flow regime classification and discovered a different type of wave pattern: criss-cross under low rotating speed and flow rate, as in Fig. 2.9.

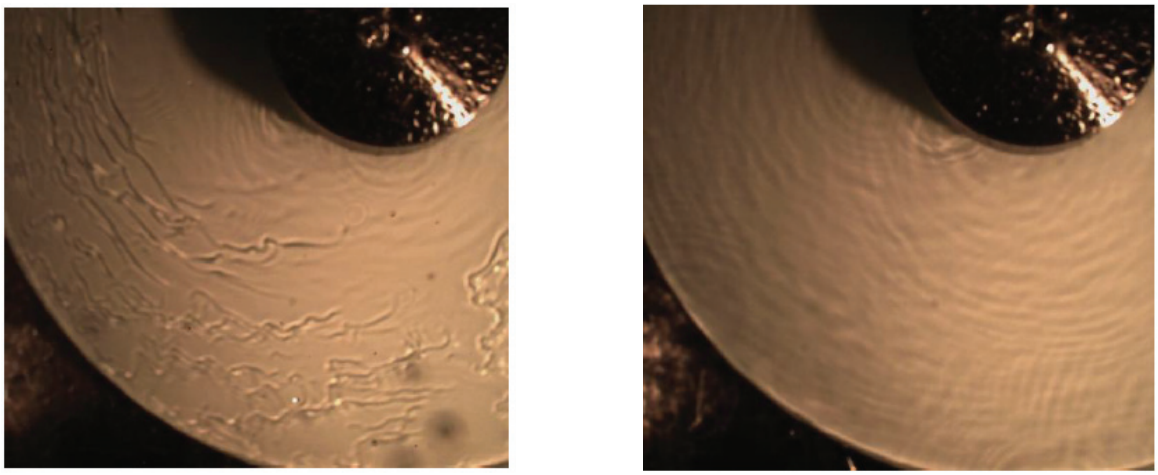

(a) Irregular waves (b) Criss-cross

Figure 2.9: Wave propagation of thin film over a spinning disk, where the flow rate is 19ml/s and the rotational speed increases from 100 rpm(a) to 200 rpm (b), reproduced from Boiarkina [11]

Apart from the observation of wave structures, many researchers focus on one of the most significant applications: the Spinning Disk Reactor (SDR), which exploits the centrifugal force to spread the liquid film onto a horizontal spinning disk, leading to higher heat and mass transfer rates [4, 10, 49, 50]. Boodhoo and Jachuck [4] and Vicevic *et al.* [51] studied the SDR (as seen in Fig. 2.10) for styrene polymerisation process, where conventional batch reactor runs into issues with wide Molecular Weights (MW), leading to the poor quality of polymer produced. The application of SDR showed an improvement of polydispersity index associated with the MW broadening, significant reduction in reaction time and one order of magnitude increase in the polymerisation rate. The improvement in the polymerisation rates and MW due to introduction of SDR was also discovered in the photo-polymerisation process by Boodhoo *et al.* [52] using n-butyl acrylate homo-polymer. Vicevic *et al.* [53] also investigated the performance of SDR compared with batch reactor, on the reaction rearranging the α-pinene oxide where two kinds of catalysts have been immobilised on the SDR as supporter. They concluded that the advantages of SDR include achievement of higher shear rate, more controllable selectivity of the process via changing the residence time on the disk, and elimination of the need for further purifications with catalyst staying longer time of activity.

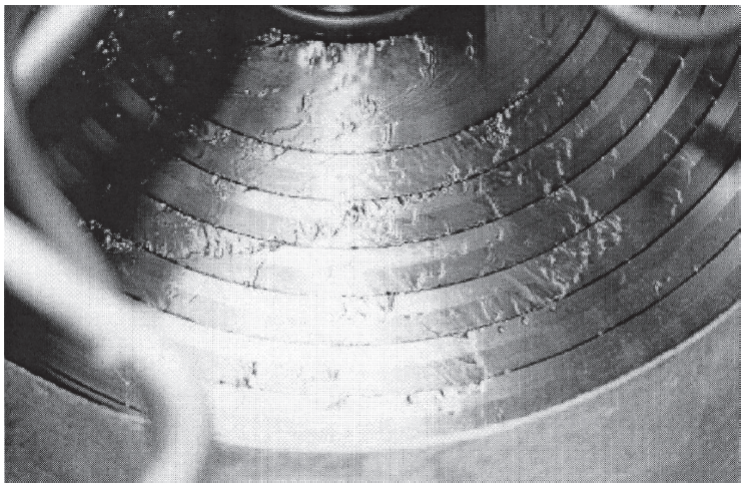

Figure 2.10: Surface waves observed on a rotating grooved disk [4]

The mathematical modelling of thin film flow driven by centrifugal force is analogous to that of falling films, where the concepts of approximation solutions are similar and based on same methodologies. Integral boundary layer (IBL) approximation was introduced by Shkadov [31] in the falling film model and provides a less computational costly alternative to Volume-of-Fluid (VOF) based computational fluid dynamics (CFD) simulations. This approximation is proved successful in various research [30], including the extension to spinning disk model [54, 55].

Shkadov analysed the nonlinear finite-amplitude wave regimes of thin film over a spinning disk by applying Karman-Polhausen method in the case of moderate Reynolds number and large Ekman number [31, 56], which is a measure of relative importance of viscosity compared to the Coriolis force. Investigations of Shkadov models [56] used extensive numerical methods to convert well-studied falling films under gravity into thin film over a spinning disk and obtained solutions of nonlinear PDE with thin layer approximation, which reveal the "wave families" that corresponds to non-unique wave solutions under the same disk parameters for a given frequency. Sisoev and Shkadov [57] observed the "dominating waves", with greatest wave velocity and largest peak height, which remain unaltered for initial conditions. Sisoev [2, 58] subsequently extended the work in concert with bifurcation theory, computed nonlinear waves of the second family of Shakdov model at large Ekman number, and validated the result against the experimental observations from Woods [5].

Matar *et al.* [26] applied the IBL method and obtained a set of non-linear PDEs, derived from

continuity and Navier-Stokes. The corresponding transient numerical simulations of the non-linear evolution equations were conducted for travelling waves over the disk surface (Fig. 2.11), as well as their interaction leading to coarsening and the emergence of long-wave, coherent structures. Matar *el al.* [59] also discovered the coincidence of maxima of averaged radial flow rate and the minima of averaged azimuthal flow rate, so that the Coriolis force exerts stabilizing effect on the flow. Sisoev and Matar [26] also carried out research on the intensifying effect of large-amplitude waves on the gas absorption into the thin liquid film over a spinning disk with measures of enhanced mass transfer coefficient. Following studies have been carried out in terms of additional conditions attached to the thin film over a spinning disk, including adding surfactants, electric field and wall topography [55, 60], which are motivated by intensification of transport rates and mixing. It is shown that electric fields are particular effective in destabilising the interface, including the normally waveless "spin-up" region near the inlet, surface topography can enhance the interfacial waviness and inlet forcing can be applied to control the wave evolution on the disk surface.

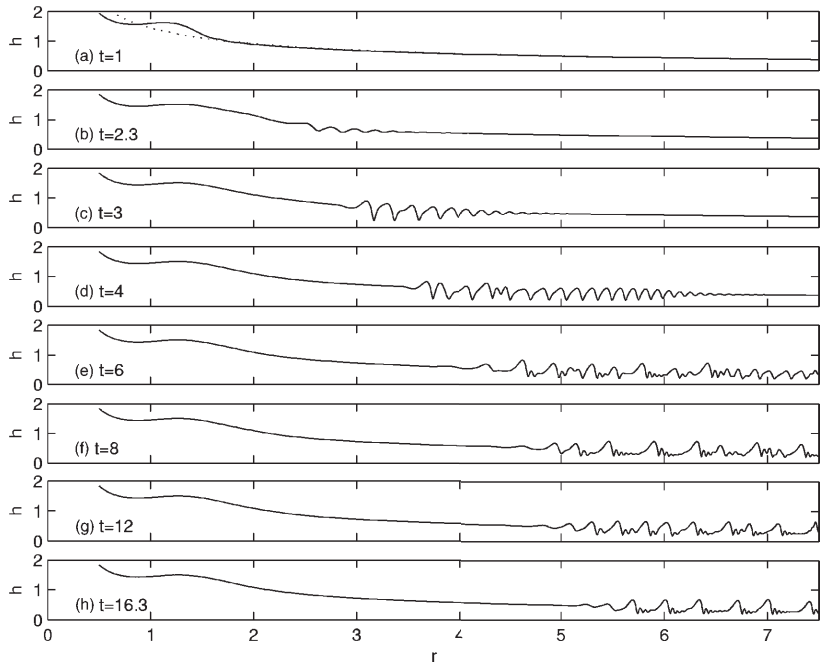

(a)

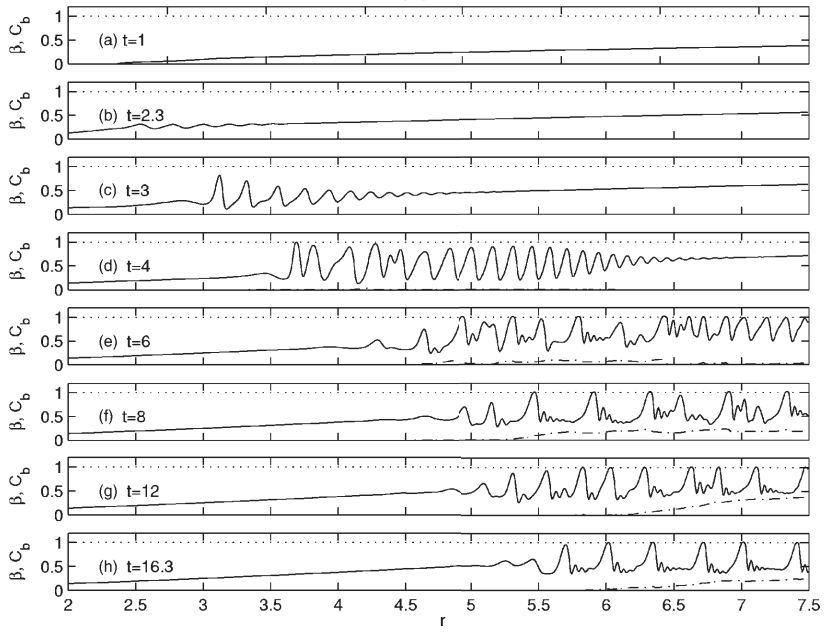

(b)

Figure 2.11: Evolution of interfacial height (a) and concentration (b) at different dimensionless time intervals [26]

Added complexity is brought with the presence of chemical reactions associated with the thin film flow, whether in the falling film flow [13, 14] or the thin film over a spinning disk [12], due to the instantaneous change in the concentration and temperature profile of the flow, which in turn affect interfacial conditions. In the context of thin film flow over a spinning disk, Prieling and Steiner [12, 16] also applied the Integral boundary layer method in the spinning disk model,

with the inclusion of chemical reactions and wall mass transfer in the associated coupled PDEs. It is found that the surface etching process (with potential industrial application silicon wafer manufacture) in the outer region in the radial direction increases with rotational speed as the film thickness decreases with increasing rotational speed, which in turn leads to thinner concentration boundary layers and increases the wall gradient and mass fluxes, resulting in the increase of etching rate.

Modelling work of non-axisymmetric waves include the characterisation of spiral waves [61] and inclination angle relative to the direction perpendicular to the radius was applied in order to characterise the spirals and they proposed that generation of spiral waves was due to an entrance effect and the surface waves generated by entrance perturbations acted as a periodic forcing on the liquid film and initiated a cascade of instability mechanisms. Sisoev *et al.* [62] came up with coupled PDEs of film thickness and volumetric flow rate using integral boundary layer method and assumption of parabolic velocity profiles under stationary conditions and was able to compare the spiral waves from the model to Archimedian spirals. In the regime of spiral waves, these waves were characterised by the deviation angle from the Archimedean spiral denoted by $r = \alpha(\theta - \theta_0) + r_0$, where the angle β characterising spiral deviation from a circle is:

$$\beta = \arctan\left(\frac{1}{r}\frac{dr}{d\theta}\right) = \arctan\left(\frac{\alpha}{r}\right) \tag{2.7}$$

According to Eqn. (2.7) above, a single parameter α is calculated by analytically approximating the deviation angle at different radial position for spiral waves. They also associated the α with Ekman number for each sprial waves, as seen in Fig. 2.12.

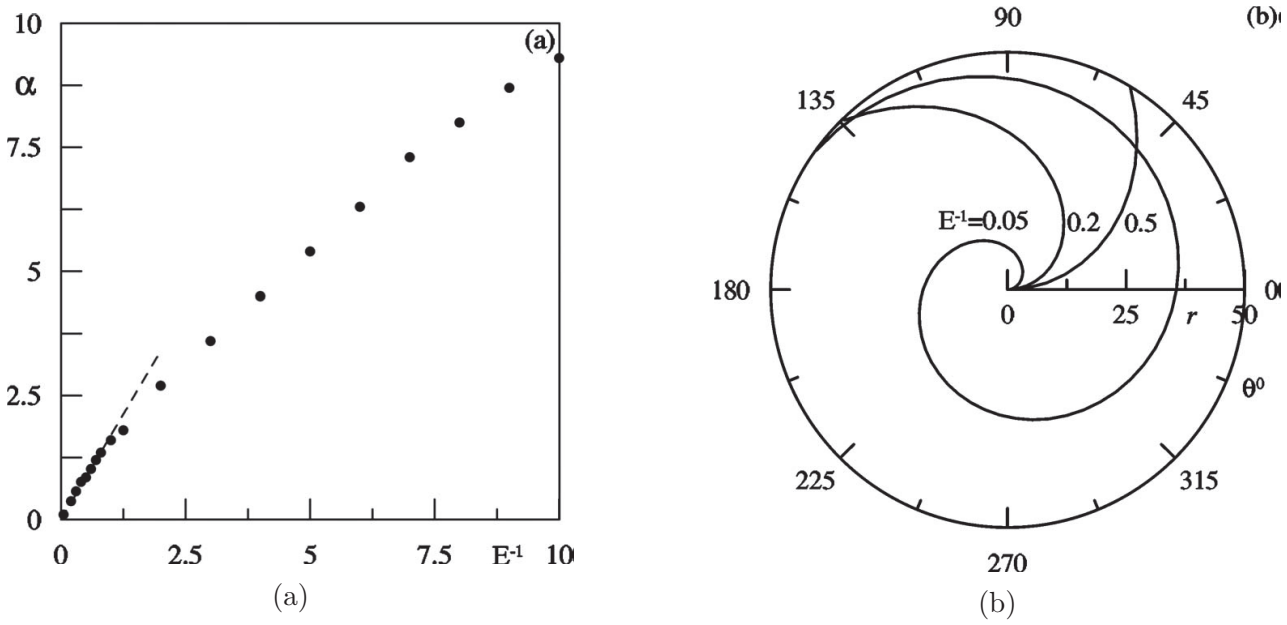

Figure 2.12: Deviation angle vs Ekman number, (a), and examples of spiral wave at different Ekman numbers, (b), reproduced from Sisoev *et al.* [62]

The previous study of thin film over spinning disks mostly assume that the flow is axisymmetric over the entire disk or steady state solutions with non-axisymmetric condition, while the experimental observation of various waves regime indicates that we need a more robust model accounting for non-axisymmetric, unsteady waves evolution. The present work attempts to extend the scope of these previous studies by covering the full radial and azimuthal extension of the rotating disk, and focus is on flow regimes and the effect of waves on the intensification.

Due to the complexity of developing and implementing a numerical model with custom code, commercial CFD packages are used to solve a variety of problems by implementing user-defined geometry and specifying the corresponding boundary conditions. Bhatelia *et al.* [63] were the first to investigate the CFD modelling of thin film across rotating disks using commercial CFD software, Fluent. Their CFD research was compared against experimental results by Burns *et al.* [48], and included a 2D axisymmetric model on a structured mesh and a 3D model on a rotating reference frame (instead of a moving disk). The flow was considered incompressible and laminar, with a uniform mesh size of 50 µm for both two and three dimensional models. They found out that the 2D model produced adequate results compared with experimental data from Burns *et al.* [48]. However, in the 3D model, dry spots appeared on the disk and

the full constant film was not generated accordingly. The film thickness results predicted by the 3D model do not agree well with experiment data from Burns *et al.* [48].

Caprariis *et al.* [64] also applied the CFD package Fluent to model the thin film flow over a rotating disk. They considered a Large Eddy Simulation (LES) model to simulate the flow over a rotating disk. The simulation results were validated against experimental data from Burns *et al.* [48], and showed good agreement. However, the validation was limited to one set of experimental data and the CFD results also agreed well with analytical Nusselt solution, with no major improvement from the simple analytical model.

More recent CFD study by Majnis *et al.* [65] focused on the mixing effects of thin film flow over a rotating disk, where hexahedral structured mesh with 24560 total mesh volumes were applied in the computational domain. In order to determine whether the flow was mesh independent, they carried out simulations with finer mesh and they compared well with courser mesh solutions. They measured the mixing performances of the flow by visualisation of the dye particle spatial distribution from both experiment and CFD simulation, and found out a good agreement was achieved. Also, quantitative measure of mass transfer coefficients under different rotational speeds from CFD simulation was compared well against the figures in the model by Tsibranska *et al.* [66].

2.2 Artificial Neural Network in Fluid Dynamics

Apart from traditional mathematical approximation and numerical simulation (reduced or full) investigation, Artificial neural network (ANN) has been applied in order to determine the profile of underlying velocity or stress condition associated with the flow, by integrating training data from existing numerical simulation, e.g. Computational Fluid Dynamics (CFD). In this way, we can obtain a faster solution to this problem since ANN can "learn" the behaviour from external data associated with the problem and predict reasonable results after the learning process is complete.

2.2.1 Neural Network Structure

Artificial Neural Network consists of a small number of elements, called neurons, which is inspired by our biological nervous systems. As in nature, the objective of a neural network is to determine the function through connections amongst all the neuron units. The neural network is trained to perform complex functions by adjusting the values of connections (weights) between various neurons, as shown in the schematic below Fig.2.13.

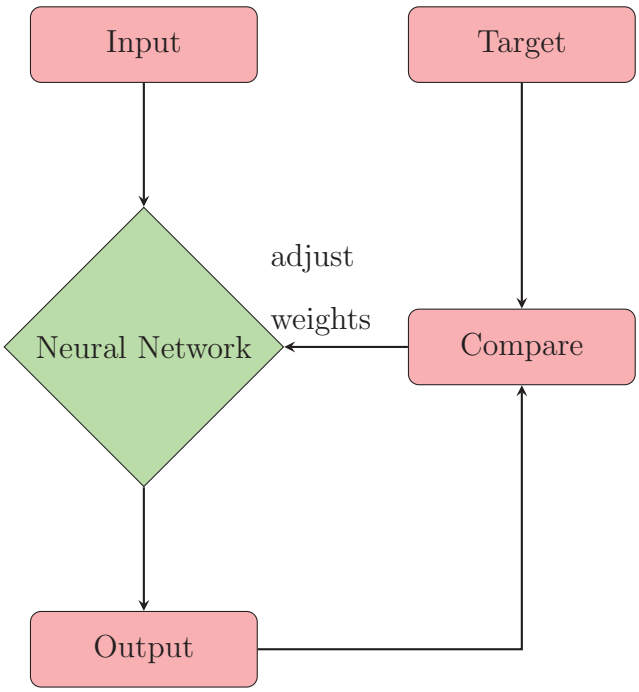

Figure 2.13: Sketch of neural network structure

Typically, a neural network is trained in a way so that a specific output (target) is obtained after an input is fed into the system. The system is continuously adjusted, based on the comparison between the target and the output from the network, until a small margin of error is accepted, as depicted in Fig. 2.14.

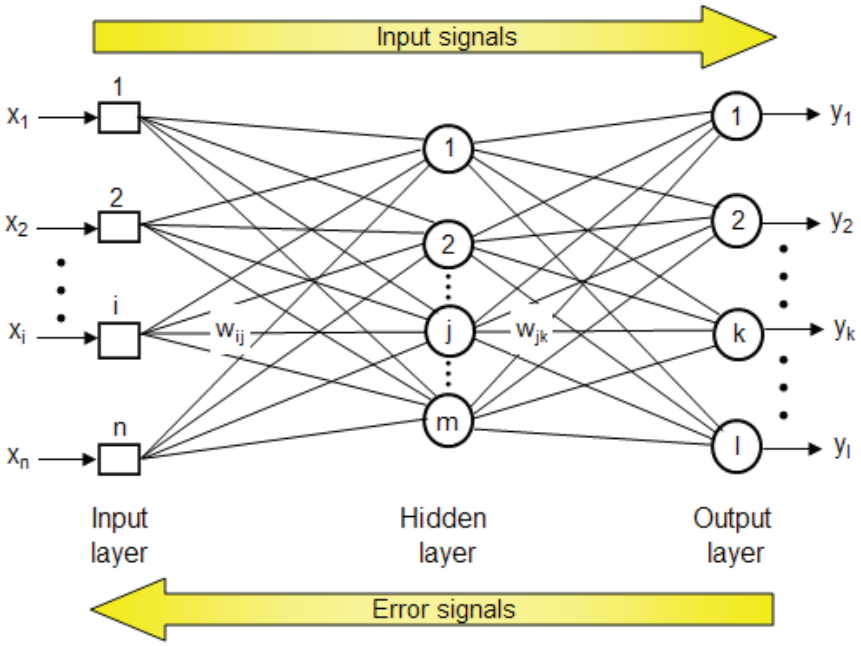

Figure 2.14: Feedforward neural network architecture [67]

The most commonly used framework in ANN is feed-forward network, consisting of three layers of neurons: an input layer, at least one intermediate hidden layer and an output layer. Back-propagation is the traditional optimization method to train the neuron network during which the neurons adapt their weight to acquire new knowledge, in order to minimise the cost function.

2.2.2 Applications in Fluid Dynamics

Due to the significance of neural network, it has been applied in various industries and the discussion of neural network in a broad environment is beyond the scope of this thesis. This study mainly focuses on the applications of ANN in the fluid dynamics related review.

Lagaris and Likas [17] presented a method using artificial neural network to solve ordinary and partial differential equations, where the trial solution is divided into two parts: the first part satisfies the initial/boundary conditions but contains only fixed parameters; the second part is constructed so as not to intervene with initial/boundary conditions but involves a feedforward neural network with adjustable weights. Thus, the neural network can be trained to satisfy the differential equations while the initial/boundary conditions are satisfied by construction.

Modern applications of ANN include the integration Direct Numerical Simulations (DNS), which can reveal the dynamics of complex geometry or flows of interest, e.g. multiphase flow [68, 69, 70], however, requires fine resolution and significant computational power. In many cases, the small scales can be modelled instead of fully resolved since their behaviour exhibits universality. Thus, it remains an emerging challenge to exploit existing DNS results and develop a reliable reduced model for industrial purposes, bypassing the large scale time-consuming DNS.

ANN has been applied in order to tackle the aforementioned challenge. For single phase turbulent modelling, Milano *et al.* [71] reconstruct near-wall turbulent flows with neural network technique ,and Rajabi and Kavianpour [72] used neural networks to interpolate DNS data for a backward facing step. Other examples includes the development of a subgrid model for Large Eddy Simulation (LES) by [73] Sarghini *et al.*, the optimal estimation of subgrid models for LES by Moreau *et al.* [74], the parametrization of surface features in coarse LES by Esau and Rieber [75], and the use of neural networks to optimize the model constants of the k turbulence model applied to simulations of data centers by [76]. Tracey et al. [77] used statistical learning to determine the functional dependency of the closure terms for data generated by Spalart-Allmaras turbulence model, rather than full DNS. On the other hand, Duraisamy *et al.* and Parish and Duraisamy [78] used inverse modelling to obtain spatially distributed functional terms to aid closure modelling, instead of inferring model parameters directly, and later Singh [79] have used the similar method for turbulent flows over airfoils involving flow separation, showing much improved predictions in lift and surface pressure.

Recently, due to the rapid development of machine learning techniques, increasingly efforts are focused on how to combine machine learning with turbulent modeling and how to generalize the RANS model with machine learning, Ling *et al.* [80] specifically addressed physical systems that possess symmetry or invariance properties by comparing two different methods for teaching a machine learning model an invariance property, and shows that embedding the invariance property into the input features yields higher performance with less computational cost. They present a method of using deep neural networks to train a model for the Reynolds stress anisotropy tensor from high-fidelity simulation data, demonstrating significant improvement over baseline RANS linear eddy viscosity and nonlinear eddy viscosity models, based on two

test cases. Gamahara [81] used neural network as a tool for exploring a new subgrid model of the subgrid-scale (SGS) stress for LES based on turbulent channel flow DNS database, and later applied the ANN approximation in the area of urban surface morphology, which behaves poorly in the LES due to the limitation of computer facilities.

For multiphase flows, Lu *et al.* [82] computed the response of fully-resolved particles to a shock and used a neural network to develop closure laws for macroscopic simulations of the gas-particle mixture. Sen *et al.* [83] discussed various techniques to bridge the scales between detailed microscopic simulations and macroscopic models, focusing on the convergence rate for various model problems. Ma *et al.* [84] trained a neural network to obtain the closure terms in the multiphase flow in a simple spherical bubble rising vertically in a periodic domain. The training data from existing DNS data can be used to construct a network that can be further applied to simulation of the system with other initial conditions, with good agreement with DNS data (Fig. 2.15). The specific implementation is via Matlab Toolbox that applied feed-forward back-propagation neural network and the Levenberg-Marquardt method to optimize the weight coefficients attached to the inputs, which connects the three inputs, ten neurons, and one output for each closure relation, as in Fig. 2.14

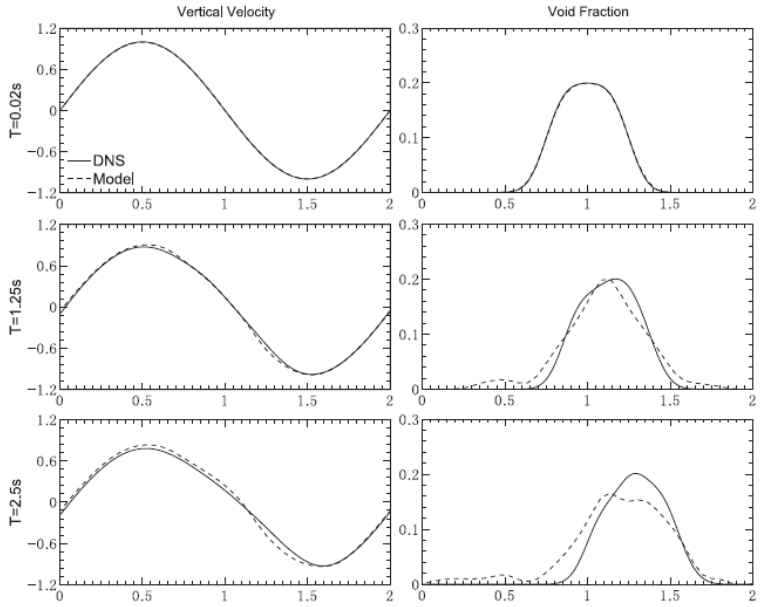

(a)

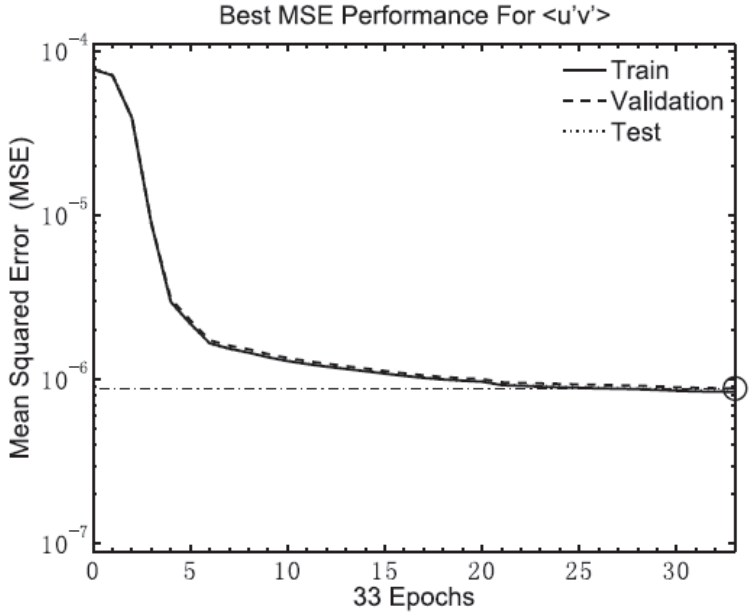

(b)

Figure 2.15: Profile of vertical velocity and void fraction from averaged DNS (solid line) data and neural network (dash line) prediction at different times (0.02s, 1.25s, 2.50s); and Mean Squared Error of streamwise stress, reproduced from Ma *et al.* [85]

What we want to achieve in the thesis is similar to the work in Ma *et al.* [85] following the feedforward neural network approach, implemented by Matlab Neural Network Toolbox. It is a lighter work load for computers and less time-consuming compared with the huge amount of DNS training data since our data is originated from the numerical solutions of PDEs (lower-

order modelling). However, our hypothesis is this will still improve our current numerical capabilities and allow us to extend to wide regions of parameter space without the expensive computation of the multi-dimensional PDE solver.

Chapter 3

Formulation

This thesis involves the mathematical modelling of single-layer thin liquid flow driven by centrifugal force, with the presence of first-order chemical reaction. In this chapter, we present an overview of the governing equations and boundary conditions which describe the dynamics of the aforementioned flow and explain the significance accordingly. Also, the choice of non-dimensionalisation and application of lubrication assumption are discussed. In subsequent chapters, equations derived in the following sections are referred in order to identify the distinct features of the various flows of interest.

3.1 Governing Equations

In Chapter 4, we consider the dynamics of single-layer thin liquid film flow over spinning disks, assuming non-axisymmetric everywhere over the entire disk. In Chapter 5, the addition of first-order chemical reaction is considered. In this chapter, we derive the leading order mathematical equations and boundary conditions for a single-layer thin films over spinning disks, where the fluids are assumed Newtonian, incompressible and immiscible. The aforementioned configuration is applied in both Chapter 4 and Chapter 5, and here we give fundamental concepts of mathematical modelling as a general case, which can be specified in Chapter 4 and 5.

We intend to describe the flow of thin liquid film over a spinning disk, with the presence of first-order chemical reaction at the gas-liquid interface. In particular, the schematic of the geometry is given in a three-dimensional (3D) cylindrical coordinate system, (r, θ, z), as shown in Figure 3.1. r,θ,z denote the stream-wise, span-wise and normal directions to the flow respectively. The disk is considered to be a rigid impermeable wall, with a rotational speed ω and the Newtonian incompressible fluid is injected onto the disk from a distributor at the disk centre. The ambient gas is saturated with reactant A which turns into product B at the interface, located at $z = h(r, \theta, t)$. Both reactant A and product B are assumed to have no effect on the flow field.

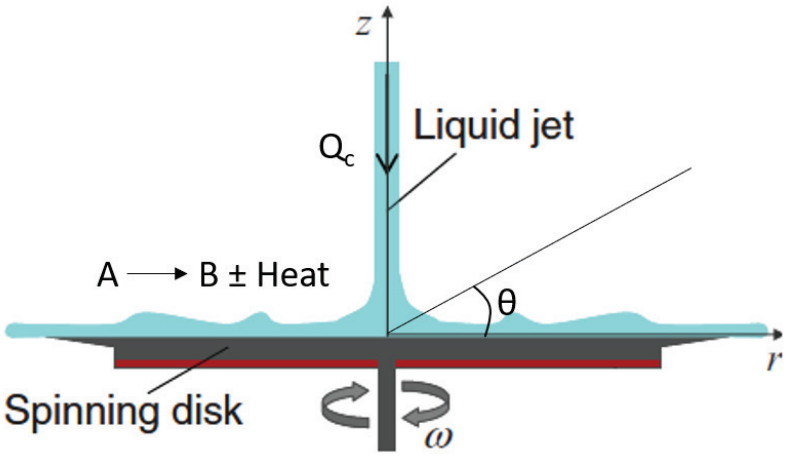

Figure 3.1: Schematic diagram of thin films flow over a spinning disk with a chemical reaction [86]

The equations governing the flow dynamics are 3D continuity, momentum, convection-diffusion and energy conservation equations; the momentum equations reduce to the well-known Navier-Stokes equations for incompressible Newtonian fluid in the cylindrical system:

$$\nabla \cdot \mathbf{u} = 0 \tag{3.1}$$

$$\rho \left(\frac{\partial \mathbf{u}}{\partial t} + \mathbf{u} \cdot \nabla \mathbf{u} \right) = -\nabla p + \mu \nabla^2 \mathbf{u} + \rho \mathbf{g} \tag{3.2}$$

$$\frac{\partial c}{\partial t} + \mathbf{u} \cdot \nabla c = D_i \nabla^2 c + R_S \tag{3.3}$$

$$\rho c_p \left(\frac{\partial T}{\partial t} + \mathbf{u} \cdot \nabla T \right) = k \nabla^2 T + \frac{1}{2} \mu \mathbf{e} : \mathbf{e} + q \tag{3.4}$$

where $\mathbf{u} = (u_r, u_\theta, u_z)$ and u_r,u_θ,u_z denote the radial, azimuthal and axial component of the velocity field, respectively; k represents thermal conductivity, R_S is the source term due to chemical reactions, q is associated with the heat generation (deduction) in the chemical reaction, p is the pressure in the fluid, and g is gravity vector which is negligible in this geometry. Solutions to Eqs. (3.1) and (3.4) are functions of both space and time, and subject to a suitable set of initial and boundary conditions.

Boundary conditions are an important factor in the solution of this problem and involve both wall condition and gas-liquid interaction at interface. It is noted that at the substrate $z = 0$, no-slip and no-penetration boundary conditions apply, which assumes that the radial and normal components of the fluid velocity are zero, the azimuthal component is associated with disk rotation. Also, no flux and perfect conducting solid wall assumptions are applied at the disk surface $z = 0$. These are the basic assumptions in the IBL model, widely used by researchers [2, 12, 26].

$$u_r = 0, u_z = 0, u_\theta = \Omega r,$$

$$\frac{\partial c}{\partial z} = 0, T = T_0 \tag{3.5}$$

At the interface $z = h(r, \theta, t)$, we assume the tangential and normal stress balance, along with conditions of constant concentration and no heat flux, assuming the interface is a poor conductor since the thermal conductivity of surrounding gas is much smaller than that of the liquid:

$$\mathbf{n} \cdot \tau \cdot \mathbf{n} = \sigma \kappa \tag{3.6}$$

$$\mathbf{n} \cdot \tau \cdot \mathbf{t} = \mathbf{t} \cdot \nabla \sigma \tag{3.7}$$

$$c = c_0 \tag{3.8}$$

$$\nabla T \cdot \mathbf{n} = 0 \tag{3.9}$$

where σ is the surface tension, $\mathbf{T} = -p\mathbf{I} + \mu(\nabla \mathbf{u} + \nabla \mathbf{u}^T)$ is the total stress tensor in which $\mathbf{I}$ is identity tensor; $\kappa = \nabla_s \cdot \mathbf{n}$ is the curvature with $\nabla_s = (\mathbf{I} - \mathbf{nn}) \cdot \nabla$; $\mathbf{n}$ and $\mathbf{t}$ are normal and

tangential component of stress which are defined as follows in the cylindrical coordinates:

$$\mathbf{n} = \frac{\nabla F}{|\nabla F|} = \frac{z - h_r r - \frac{1}{r} h_\theta \theta}{\left(1 + h_r^2 + \frac{1}{r^2} h_\theta^2\right)^{1/2}} \tag{3.10}$$

where $F = z - h(r, \theta)$ is a function that vanishes on the surface. Finally, at the interface, kinematic boundary condition in which the motion of the fluid is associated with the velocity at interface. It can be expressed as $F(r, \theta, z, t) = z - h(r, \theta, t) = 0$ for the interface and the kinematic boundary condition can be expressed as follows:

$$\frac{D}{Dt}\left(z - h(r, \theta, t)\right) = 0 \tag{3.11}$$

where D/Dt is a material derivative.

3.2 Non-dimensionalisation

We next use a set of scalings in order to non-dimensionalise our problem, which is considered to be a effective tool to transform the dimensional dependence of the problem into a series of dimensionless numbers governing the flow. These characteristic dimensionless groups represent physical forces, for example, the Reynolds number $Re = \rho U D_o / \mu$, defined as the ratio of inertia to viscous forces. Also, simplification of the system of equations can be achieved. In this case, the linear momentum equations, convection-diffusion and energy equations can be simplified with the applications of lubrication theory. In the geometry of this research, the film thickness is significantly smaller than the length scale, and the disparity between the length scales H and R introduces a small parameter ϵ, defined as $\epsilon \equiv \frac{H}{R}$. It can be seen in the chapter that using order-of-magnitude analysis for the system leads to simplification of the equations.

In particular, the following scalings, which are used to render the system of equations dimensionless, are consistent with in the subsequent investigations in the study:

$$r = R(\tilde{r}), (z, h) = H(\tilde{z}, \tilde{h})$$

$$u_r = U(\tilde{u}), u_\theta = U(r+\tilde{v}), u_z = U\epsilon\tilde{w}$$

$$t = (R/U)\tilde{t}, p = P\tilde{p}, \sigma = \sigma_0\tilde{\sigma}, c = C_0\tilde{c}, T = T_0\tilde{T} \tag{3.12}$$

where the quantities with a tilde are dimensionless temporarily. In order to make use of the disparity in length scales, $r \sim R$ while $(z, h) \sim H$, with $R = (\frac{Q_C}{2\pi})^{1/2}(\frac{\nu}{\Omega})^{-1/4}$ and $H = \sqrt{\nu/\Omega}$, same as in [26]. Here Q_C denotes the inlet flow rate and Ω represents the rotational speed of the disk. A characteristic velocity scale U is selected here in order to non-dimensionalise the velocity component, defined as $U = \Omega R$, which is a characteristic velocity appropriate in the cylindrical coordinates. It is noted that the radial, azimuthal and axial component of velocity field scale differently due to the fact that from the continuity equation $\frac{\partial u_r}{\partial r}$, $\frac{1}{r}\frac{\partial u_\theta}{\partial \theta}$ and $\frac{\partial u_z}{\partial z}$ are of the same order. Next, we apply appropriate scalings for pressure term. From the Eqn (3.2), a balance between deviatoric stress and pressure terms leads to $P = \frac{\sigma\epsilon}{R}$ which is appropriate when the gravitational forces are neglected in the spinning disk geometry. For additional concentration and temperature terms arisen from chemical reaction, they are scaled against reference concentration and temperature, i.e. $c = C_0\tilde{c}$, $T = T_0\tilde{T}$. Substitution of Eqn (3.12) into Eqns (3.1) - (3.11) leads to the set of leading order equations:

$$\frac{u}{r} + u_r + \frac{1}{r}v_\theta + w_z = 0 \tag{3.13}$$

$$u_t + uu_r + wu_z + \frac{r+v}{r}u_\theta - \frac{(r+v)^2}{r} = -\lambda^2\kappa_r + u_{zz} + \epsilon^2\left[\left(\frac{1}{r}(ru)_r\right)_r + \frac{1}{r^2}u_{\theta\theta} + \frac{2}{r^2}(r+v)_{\theta\theta}\right] \tag{3.14}$$

$$v_t + u(r+v)_r + \frac{u(r+v)}{r} + wv_z + \frac{r+v}{r}v_\theta = -\lambda^2\frac{1}{r}\kappa_\theta + v_{zz} + \epsilon^2\left[\left(\frac{1}{r}(rv)_r\right)_r + \frac{1}{r^2}(r+v)_{\theta\theta} + \frac{2}{r^2}u_{\theta\theta}\right] \tag{3.15}$$

$$c_t + uc_r + \frac{r+v}{r}c_\theta + wc_z = Sc^{-1}c_{zz} - Dac + \epsilon^2[...] \tag{3.16}$$

$$T_t + uT_r + \frac{r+v}{r}T_\theta + wT_z = Pe^{-1}\left(T_{zz} + Da\nu e^{\frac{c}{RT_0}\frac{T-1}{T}}c\right) + \epsilon^2[...] \tag{3.17}$$

where the dimensionless numbers in the equations are defined below:

$$\lambda^2 = \frac{\sigma H}{\rho\Omega^2 R^4}, \epsilon^2 = \frac{H^2}{R^2}, Sc = \frac{\nu}{D_i}, Da = k_0 e^{-\frac{E}{RT_0}}, Pe = \frac{\rho\nu C_p}{k}$$

The parameter λ^2 is modified Weber number which measures relative importance of surface tension compared with inertia, Da represents Damkohler number for chemical reaction rate compared with mass/heat transfer, Sc is Schmidt number measuring the ratio of viscous diffusion over molecular diffusion, Pe is the Peclet number defining a ratio of advection of physical quantity to diffusion. [...] stands for the term to be neglected due to the scalings with ϵ^2. The boundary conditions are given, at the wall $z = 0$:

$$u = v = w = 0, c_z = 0, T = 1 \tag{3.18}$$

and at the interface $z = h(r, \theta, t)$:

$$u_z = 0, v_z = 0 \tag{3.19}$$

$$h_t + uh_r + \frac{v}{r}h_\theta = w \tag{3.20}$$

$$c = 1, T_z = 0 \tag{3.21}$$

In terms of the pressure term, due to the simplification of vertical component of Eqn. (3.2) for thin films, i.e. $\frac{\partial p}{\partial z} = 0$, together with the normal stress balance at interface, it can be concluded that:

$$p = -\sigma \left(\frac{1}{r}(rh_r)_r + \frac{1}{r^2}\frac{\partial^2 h}{\partial \theta^2} \right) \tag{3.22}$$

Next, the dimensionless numbers are examined in order to derive the evolution equations. The dimensionless numbers above are all small, but we retain the inverse Schmidt number Sc^{-1}, inverse Peclet number Pe^{-1} and the square of wavelength λ^2, which neglecting the square of aspect ratio ϵ^2, which is common practice under lubrication theory. This means that we keep the capillary and cross-stream (azimuthal direction in cylindrical coordinates) diffusion terms while neglecting stream-wise (radial direction in cylindrical coordinates) diffusion terms, i.e. $\epsilon^2 \ll \lambda^2 \ll 1$

3.3 Evolution Equations

The scalings introduced above lead to the reduction of the original set of equations describing the dynamics of thin flow over a spinning disk. The objective of this section is to derive the evolution equations for film thickness,volumetric flow rates, concentration and temperature, subject to suitable wall and interfacial boundary conditions. Before proceeding the derivation, the ϵ^2 terms are neglected in Eqs.(3.13) - (3.17) under the assumption that the characteristic height is significantly smaller than the length scale.

Integration of the Eqs. (3.13) - (3.17) from $z = 0$ to $z = h(r, \theta, t)$, applying Leibniz integral rule, taking into account of wall and interfacial boundary conditions, yields

$$h_t + \frac{1}{r} f_r + \frac{1}{r^2} g_\theta = 0 \tag{3.23}$$

$$f_t + \left(r \int_0^h u^2 dz \right)_r + f_\theta - r h_\theta u|_{z=h} + \left(\int_0^h uv dz \right)_\theta - \int_0^h v^2 dz = \lambda^2 h r \kappa_r + r u_z|_{z=0} + r^2 h + 2g \tag{3.24}$$

$$g_t + r \left(\int_0^h uv dz \right)_r + 2 \int_0^h uv dz + g_\theta - r h_\theta v|_{z=h} + \left(\int_0^h v^2 dz \right)_\theta = \lambda^2 \kappa_\theta - r v_z|_{z=0} - 2f \tag{3.25}$$

$$\left(r \int_0^h c dz \right) + \left(r \int_0^h uc dz \right)_r + \left(\int_0^h vc dz \right) = Sc^{-1} r c_z|_{z=h} - r I Da \tag{3.26}$$

$$\left(r \int_0^h T dz \right)_t + \left(r \int_0^h uT dz \right)_r + \left(\int_0^h vT \right)_\theta = Pe^{-1} \left(h_r T_z|_{z=h} - T_z|_{z=0} \right) + DaPe\phi I \tag{3.27}$$

where f and g are radial and azimuthal flow rates respectively. I is integral of both concentration and temperature arising from the Arrhenius equation from chemical reaction:

$$f = r \int_0^h u dz, g = r \int_0^h v dz, I = \int_0^h c e^{\frac{(T-1)}{T}} dz \tag{3.28}$$

In the case of falling films and flows over spinning disks, the inertia plays a significant role. We employ a von Karman-Polhausen approach in conjunction with Integral Boundary Layer method to derive evolution equations that can describe the dynamics. In this theory, we assume the semi-parabolic velocity profile, satisfying wall and interfacial boundary conditions, adopted by Sisoev *et al.* [26] and Matar *et al.* [58, 2]:

$$u = \frac{3f}{rh}\left(\zeta - \frac{1}{2}\zeta^2\right) \tag{3.29}$$

From the Eq. (3.2) and by equation the second derivative of azimuthal velocity with radial velocity $v_{zz} = 2u$, we have

$$v = \frac{5g}{4rh}\left(2\zeta - \zeta^3 + \frac{1}{4}\zeta^4\right) \tag{3.30}$$

We normalize the height against the film thickness, i.e. $\zeta = z/h$. Substitution of Eq. (3.29)-(3.30) into the Eq.(3.24)-(3.25) leads to the evolution equation of radial and azimuthal flow rates.

$$\frac{\partial f}{\partial t} + \left(\beta_{11}\frac{f^2}{rh}\right)_r - \beta_{13}\frac{g^2}{r^2 h} + \frac{\partial f}{\partial \theta} - \frac{3f}{2h}h_\theta + \frac{17}{14}\frac{1}{r^2}\left(\frac{fg}{h}\right)_\theta = \lambda^2 rh\kappa_r - \frac{3f}{h^2} + r^2 h + 2g \tag{3.31}$$

$$g_t + \frac{1}{r}\left(\beta_{21}\frac{fg}{h}\right)_r + g_\theta + \frac{25}{16}\frac{g}{h}h_\theta + \frac{155}{126}\frac{1}{r^2}\left(\frac{g^2}{h}\right)_\theta = \lambda^2 h\kappa_\theta - \frac{5}{2}\frac{g}{h^2} - 2f \tag{3.32}$$

where the non-axisymmetric curvature in the cylindrical coordinates is:

$$\kappa = \frac{h_r + rh_{rr}(h_\theta^2 + r^2) + rh_{\theta\theta}(h_r^2 + 1)}{[r^2(h_r^2 + 1) + h_{\theta\theta}^2]^{3/2}} \tag{3.33}$$

According to the long wave theory, Eqn. (3.33) above is reduced to:

$$\kappa = \frac{1}{r}\left(rh_r\right)_r + \frac{1}{r^2}h_{\theta\theta} \tag{3.34}$$

Similarly, in order to derive the evolution equation for concentration and temperature, we assume the semi-parabolic profile for concentration and temperature, satisfying both the wall

and interfacial conditions in Eq. (3.21):

$$c = C_b(1-\zeta^2) \tag{3.35}$$

$$T = (2\zeta - \zeta^2)\Theta \tag{3.36}$$

Substitution of the concentration and temperature profiles in Eq.(3.35)-(3.36) into the integral equations (3.26)-(3.27), yields:

$$C_{b_t} + \frac{3\beta_{41}}{2rh} + C_{b_r} + \frac{3\beta_{41}-2}{2rh}C_b f_r + \left(\beta_{41}\frac{g}{rh}C_b\right)_\theta = -3Sc^{-1}\frac{C_b}{h^2} - \frac{3}{2}DaI \tag{3.37}$$

$$\Theta_t + \frac{3}{2rh}\beta_{51} f\Theta_r + \frac{3\beta_{51}-2}{2rh}\Theta f_r + \left(\beta_{51}\frac{fg}{rh}\Theta\right)_\theta = -Pe^{-1}\frac{3\Theta}{h^2} + \frac{3}{2}\frac{Da\Theta}{Pe}I \tag{3.38}$$

where C_b and Θ denote the dimensionless concentration and temperature profile respectively. Note here the upper-case Θ denotes the temperature while the lower-case θ indicates the angle in the spinning disk geometry. All the coefficients are defined as follows:

$$\beta_{11} = \frac{6}{5}\left(1 + \frac{\alpha_1}{24} + \frac{\alpha_1^2}{144}\right), \beta_{13} = \frac{155}{126}\left(1 - \frac{13}{5952}\alpha_2 + \frac{47}{3571200}\alpha_2^2\right), \beta_{14} = 3 - \alpha_1/2, \beta_{15} = \alpha_1$$

$$\beta_{21} = \frac{17}{14}\left(1 + \frac{19}{816}\alpha_1 - \frac{1}{1020}\alpha_2 + \frac{29}{97920}\alpha_1\alpha_2\right), \beta_{23} = \frac{5}{2} + \frac{\alpha_2}{48}$$

$$\beta_{41} = \frac{11}{20} - \frac{\alpha_1}{40}, \beta_{51} = \frac{4}{5} + \frac{\alpha_1}{60}$$

$$\alpha_1 = -\frac{\lambda^2 h^2 r}{f} MDa\phi\left(\Theta_r - Bi\Theta h_r\right), \alpha_2 = -\frac{\lambda^2 h^4 r}{g} MDa\phi\left(\Theta_r - Bi\Theta h_r\right)$$

where $Bi = \frac{H\eta}{k}$ represents the Biot number, which defines heat transfer resistance inside a body and at the surface of a body, where η is the thermal diffusivity ; $M = \frac{\gamma T_0 H}{\mu\eta}$. stands for the Marangoni number measuring thermal energy transported versus diffused, where γ is the rate of change of surface tension w.r.t temperature. We focus in the following chapter on the hydrodynamic associated with the flow.

Chapter 4

Three-dimensional Hydrodynamics

In this chapter, we discuss only the hydrodynamics associated with the flow, dropping the axisymmetric system assumption in the IBL solutions. Also, CFD simulations are performed, by courtesy of Dr Junfeng Yang, as references to validate the IBL solutions.

4.1 Governing Equations

Here, we focus on the hydrodynamic only and neglect all mass transfer related effects. Equations (3.37) and (3.38) are excluded and the evolution equations for the volumetric flow rates are reduced to a simpler form without the effect of chemical reactions:

$$\nabla \cdot \mathbf{u} = 0 \tag{4.1}$$

$$\rho \left(\frac{\partial \mathbf{u}}{\partial t} + \mathbf{u} \cdot \nabla \mathbf{u} \right) = -\nabla p + \mu \nabla^2 \mathbf{u} \tag{4.2}$$

subject to no-slip and no-penetration conditions on the substrate, and stress conditions at interface:

$$\mathbf{n} \cdot \tau \cdot \mathbf{n} = \sigma \kappa, \mathbf{n} \cdot \tau \cdot \mathbf{t} = 0 \tag{4.3}$$

After applying the same IBL method, we can obtain the following set of PDEs with dimension-

less dependent (and independent) variables:

$$h_t + \frac{1}{r} f_r + \frac{1}{r^2} g_\theta = 0 \tag{4.4}$$

$$f_t + \frac{6}{5}\left(\frac{f^2}{rh}\right)_r - \frac{155}{126}\frac{g^2}{r^2 h} + f_\theta - \frac{3f}{2h} h_\theta + \frac{17}{14}\frac{1}{r}\left(\frac{fg}{h}\right)_\theta = \lambda^2 r h \kappa_r - \frac{3f}{h^2} + r^2 h + 2g \tag{4.5}$$

$$g_t + \frac{17}{14}\frac{1}{r}\left(\frac{fg}{h}\right)_r + g_\theta + \frac{25}{16}\frac{g}{h} h_\theta + \frac{155}{126}\frac{1}{r^2}\left(\frac{g^2}{h}\right)_\theta = \lambda^2 h \kappa_\theta - \frac{5}{2}\frac{g}{h^2} - 2f \tag{4.6}$$

In practice, there is a limit on the dimensionless λ and r_{disk} values, in which the three-dimensional IBL solution are valid. The typical range of λ is 0.008 - 0.05, higher λ values typically produce smooth films without any waves and lower λ values lead to instability issues numerically when resolving higher order of derivatives. Here r_{in} and r_{disk} are the dimensionless radius boundaries defined as $r_{in} = R_{in}/R$ and $r_{disk} = R_{disk}/R$ respectively according to the scaling, where R_C and R_{disk} are physical radius of the inlet region and the whole disk. Typical range of r_{disk} is 2 - 14, as in similar modelling research [26], with higher r_{disk} resulting in wave break ups due to the implied viscous force. This limit of IBL model motivates the use of CFD simulation.

4.2 Numerical Solutions

4.2.1 Numerical Procedure - Alternating Direction Implicit

In this section, the numerical procedure used to carry out the computation is discussed, after which the numerical results and analysis are presented. The numerical procedure, based on finite difference analysis in both space and time, was used to solve the coupled equations (4.4)-(4.6), which govern the film thickness, volumetric flow rate in radial and azimuthal directions. These equations are solved using finite difference method, with a second-order centred scheme in space and Runge-Kutta third order in time. The ADI method is applied here in order to

reduce the computational cost incurred by the multidimensional independent variables:

$$h_t = L_x(h, \partial x) + L_y(h, \partial y) + L_e(h, \partial x, \partial y)$$

$$\frac{h^{n+1} - h^n}{dt} = L_x(h^{n+1}) + L_y(h^{n+1}) - L_e(h^n)$$

$$(1 - dtL_x - dtL_y)h^{n+1} = (1 + dtL_e)h^n$$

$$(1 - dtL_x)(1 - dtL_y)h^{n+1} = (1 + dtL_e)h^n$$

These solutions are subjected to the following boundary conditions at the inlet region $r = r_{in}$:

$$h = 3^{1/3} r_{in}^{-2/3}, f = 1, g = 0 \tag{4.7}$$

and decay conditions at the periphery of the disk $r = r_{disk}$. Periodic boundary conditions are applied in the azimuthal direction in the finite difference scheme. The number of grid points used to carry out the computations is 1500. Details of convergence test carried out are in Appendix B.

Numerical solutions of h, f, g are obtained after assigning a set of initial conditions, applying the solutions of steady-state equations as seen below:

$$f = 1 \tag{4.8}$$

$$\frac{6}{5}\frac{d}{dr}\left(\frac{1}{rh}\right) - \frac{155}{126}\frac{g^2}{r^2 h} = \lambda^2 rh\left[\frac{1}{r}\frac{d}{dr}\left(r\frac{dh}{dr}\right)\right] - 3\frac{1}{h^2} + r^2 h + 2g \tag{4.9}$$

$$\frac{17}{14}\frac{1}{r}\frac{d}{dr}\left(\beta_{21}\frac{fg}{h}\right) = -\frac{5}{2}\frac{g}{h^2} - 2f \tag{4.10}$$

These equations are obtained by essentially removing transient terms and azimuthally-dependent terms from Eqn. (4.4) to (4.6), by assuming the flow starts axisymmetrically everywhere.

4.2.2 Computational Fluids Dynamics

We perform the CFD simulations for this type of flow, in order to cross validate the use of Integral Boundary Layer (IBL) theory and use of parabolic velocity closure.In this section, a CFD simulation has been setup as a comparative study with the IBL solution. To this end, the governing equations consisting of two continuity equations for the gas and liquid phases, and a single set of momentum equation have been discretized and solved simultaneously within the Finite Volume Method framework using the commercial code ANSYS Fluent ver. 17.0. To capture the gas-liquid interfaces evolving dynamically, a Volume-of-Fluid (VOF) approach is employed in this work. The pressure-velocity coupling was handled by the Semi-implicit Method for Pressure-linked Equation (SIMPLE) algorithm. A bounded central differencing scheme and a second order upwind scheme were used for the momentum equation and energy equations, respectively. The High Resolution Interface Capturing (HRIC) scheme was chosen for VOF and the second-order implicit method was used to advance the solution in time.

A 3D computational domain of a quarter spinning disk, consisting of 3 million unstructured hexadedral cells, was constructed using the commercial mesh generator ICEM CFD. To resolve the thin liquid layer adjacent to the wall surface, mesh gradients (fine grids near the wall, and coarse grids for the above region) were applied in the axial direction. A uniform grid size was used in the radial direction. The liquid flow is from the top to down (against the gravity vector) through a nozzle with a constant velocity inlet boundary condition. The boundary conditions for the top and the radial outer surface were imposed as pressure outlets. In the azimuthal direction, simulating the entire liquid annulus would yield very high computational costs. Thus, noting that the flow is statistically axisymmetric, only a 90° sector domain of the 3D spinning

disk and flow above the disk surface was adopted herein and the front and back surfaces on the boundary are taken as to be periodic planes accordingly. A no-slip wall boundary condition was imposed on the rotating disk surface with a constant angular velocity, which are the same as in the IBL model. Further details are provided in Appendix A.

4.3 Comparison of IBL and CFD Predictions

Direct comparison of the profile film thickness across the disk from IBL model is performed with the CFD simulation and experimental results from Woods [5] under the same conditions (rotational speed and inlet flow rate). As seen from Fig. 4.1, the film thickness from the three sources are directly compared at the same chosen time and the same radial region. In the region near the inlet where no waves start to emerge, all the sources simply produce analytical decay profile of film thickness (Nusselt solution h_N). Thus, our focus is the comparison at the region where large-amplitude waves emerge, usually from mid to end of the disk radius. As shown in Fig. 4.1 (a), full comparison of film thickness across the disk from IBL, CFD and experiment observations in three regions (loc1, loc2 and loc3 in the legends) are conducted, under the condition of $Q_c = 13$ ml/s and $\Omega = 400$ rpm. Generally, good agreement of h is found among three sources, and both IBL and CFD capture the waves observed in the experiment in those three regions.However, a discrepancy between film thickness observed in experimental results and that predicted by the IBL and CFD models occurs, in the mid radial range (i.e. location 2), possibly due to the inlet perturbations that arise naturally in the experiments for which there is no analogue in the models. Fig. 4.1 (b)-(d) depict specific regions of interest in the radial direction where the wave from experiment observation is directly compared with those generated by IBL and CFD. A good agreement can be found for the large-amplitude wave from different sources at these wave regions, and the differences in the values of thickness from the three sources are small compared with the initial inlet height of 1 mm. However, a small discrepancy exists in terms of the accompanied small-amplitude capillary waves. For the case of 19 ml/s and 100 rpm depicted in Fig. 4.1 (c)-(d), the IBL model captures the small capillary waves between 0.15 m and 0.154 m, in agreement with the experimental observations

from Woods [5], whereas they are absent in CFD simulation, possibly due to the insufficient resolution in the simulation setup.

(a) $Q_c = 13$ ml/s, $\Omega = 400$ rpm

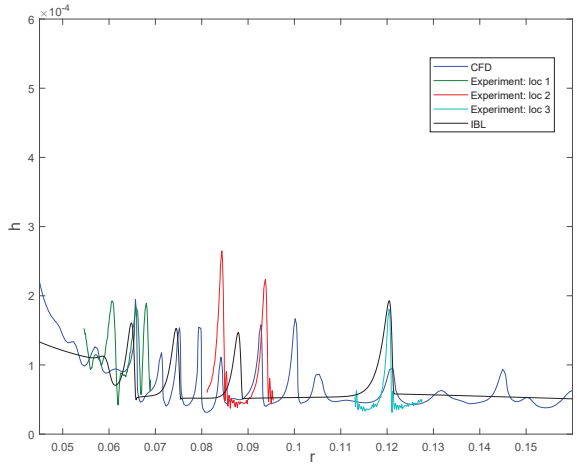

(b) $Q_c = 13$ ml/s, $\Omega = 400$ rpm

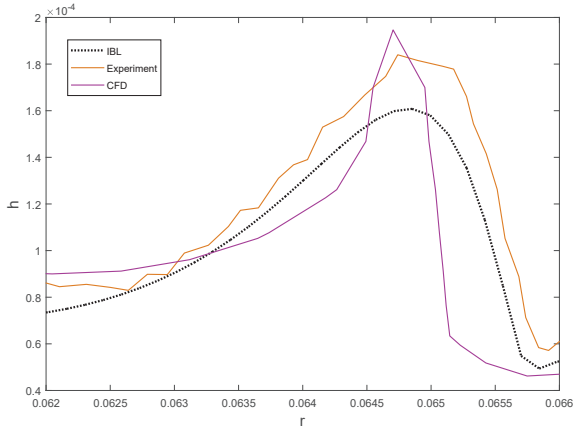

(c) $Q_c = 13$ ml/s, $\Omega = 100$ rpm

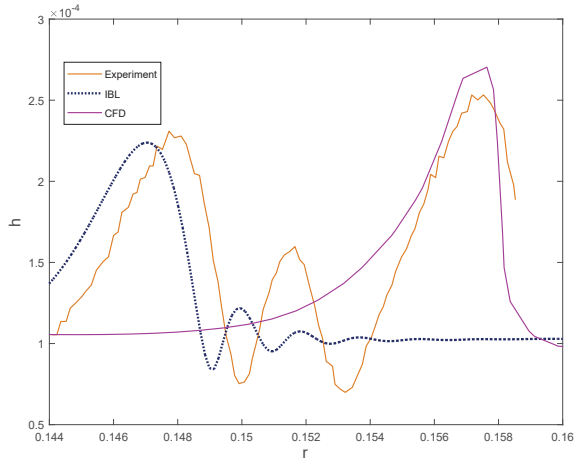

(d) $Q_c = 19$ ml/s, $\Omega = 100$ rpm

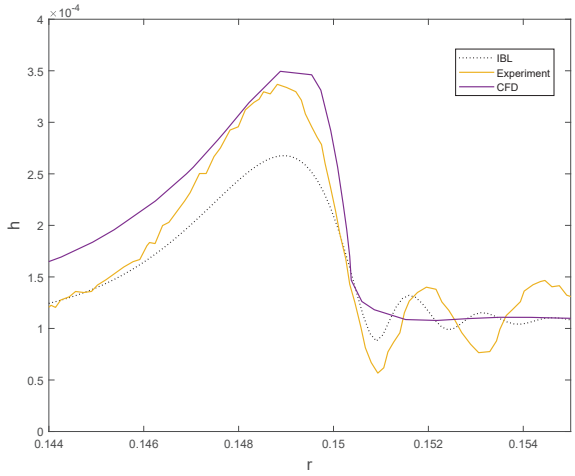

Figure 4.1: Comparison of film thickness (in metres) obtained from the IBL model, CFD simulations, and experimental observations [5]: (a) film thickness across the disk radius, with $\Omega = 400$ rpm , $Q_c = 13$ ml/s ($\lambda = 0.008$, $r_{disk} = 8.0$) (b) film thickness at $r = 0.062 - 0.066$ m where a specific wave is observed, with the same operation conditions (c) film thickness at $r = 0.144 - 0.16$ m, with $\Omega = 100$ rpm , $Q_c = 13$ ml/s ($\lambda = 0.02$, $r_{disk} = 8.0$) (d) film thickness at $r = 0.144 - 0.155$ m, with $\Omega = 100$ rpm , $Q_c = 19$ ml/s ($\lambda = 0.015$, $r_{disk} = 8.0$)

In order to quantify the deviation of film thickness values between IBL model and CFD simulation, interfacial waviness W is adopted here, which is defined below in one dimensional form:

$$W = \sqrt{\int_0^{t_{end}} \int_{r_{in}}^{r_{disk}} r(h - h_N)^2 dr dt}$$

where $h_N = 3^{1/3} r^{-2/3}$ is derived from approximation of steady solution at large value of r

(Nusselt solution) and the original form is $W(t) = \sqrt{\int_{r_{in}}^{r_{disk}} r(h - h_N)^2 dr}$ used by Matar [55]. As shown in Table 4.1, W from both CFD and IBL solutions is presented, with varying operating conditions i.e. rotational speed and inlet flow rate. Also, these W are computed by numerical integration of $W(t)$ with the last dimensionless time step $t_{end} = 10$. It can be seen here that CFD result is generally aligned with IBL solutions, however, it produces a higher level of waviness W than IBL model, as CFD simulation shows larger-amplitude waves in early stages of wave-propagation. Also, W increases with decreasing λ, due to generation of more large-amplitude waves from higher inertia terms incurred by lower λ value.

Table 4.1: W from CFD and IBL under different operating conditions

	$\lambda = 0.022$ (13 ml/s 100 rpm)	$\lambda = 0.015$ (19 ml/s 100 rpm)	$\lambda = 0.009$ (19 ml/s 200rpm)
IBL	3.36	5.20	6.50
CFD	3.57	5.31	6.78

In order to validate our IBL model assuming the semi-parabolic profile of velocity in the radial direction, a comparison between the velocity profile under the waves from IBL model and that of CFD model was performed at different radial locations near the wave, for a rotational speed 100 rpm and inlet flow rate 19 ml/s, as seen in Fig. 4.2. Good agreement between the velocity profiles under the waves is found under the radial locations ($r = 0.148, 0.149, 0.150, 0.151$ m) from Fig. 4.3. The red line shows the analytical parabolic velocity profile, in accordance with the assumption (e.g. $du/dz = 0$ at interface) in the integral boundary layer (IBL) model while the black line reveals the actual velocity profile from CFD simulation after resolving the full Navier-Stokes equation. In most of the regions, velocity profile from CFD simulations is very close to parabolic as assumed in the IBL model, especially in the smooth region and some degree of discrepancy occurs when the velocity is investigated right under the travelling waves. For example, in Fig. 4.3 at the same operation conditions ($Q_c = 19$ ml/s, $\Omega = 100$ rpm) at the disk radius $r = 0.148$ m and $r = 0.149$ m before the peak of waves the velocity profile from IBL and CFD almost overlaps, however, the CFD velocity profile starts to marginally deviate from analytic parabolic solution from $r = 0.150$ m right under the peak of wave, as shown in Fig. 4.1 due to the formation and propagation of large amplitude waves towards the disk periphery.

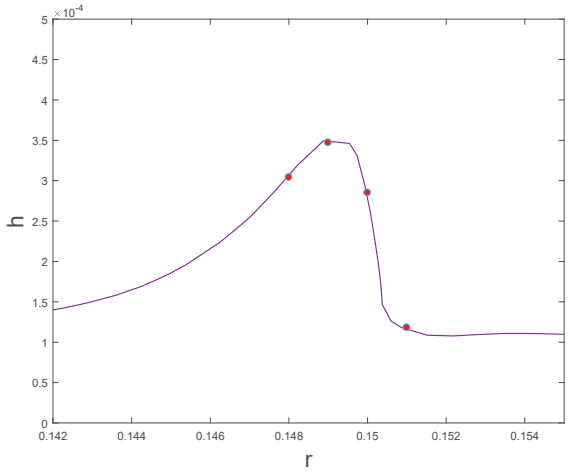

Figure 4.2: The locations where velocity profiles are taken, with $\Omega = 100$ rpm , $Q_c = 19$ ml/s ($\lambda = 0.015$, $r_{disk} = 8.0$)

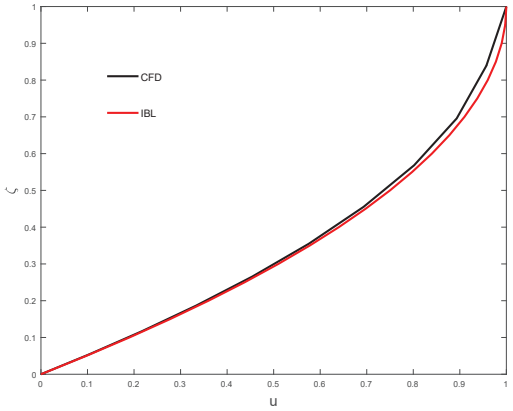

(a) $r = 0.148$ m

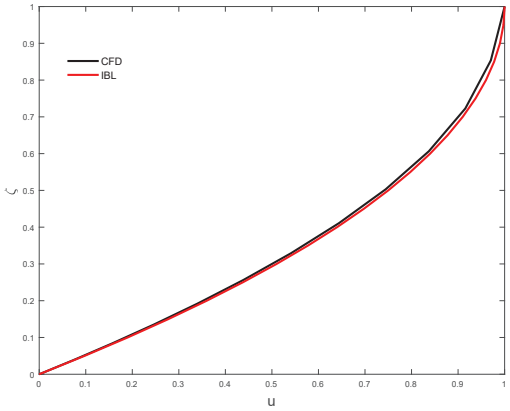

(b) $r = 0.149$ m

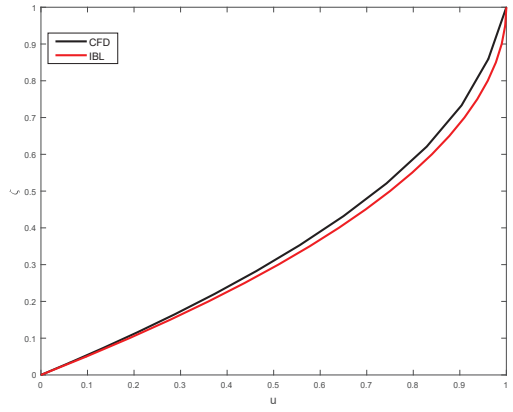

(c) $r = 0.150$ m

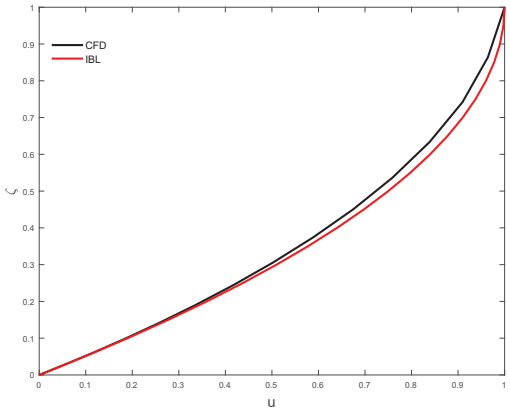

(d) $r = 0.151$ m

Figure 4.3: Comparison of radial velocity profile u under the waves from CFD (black line) and IBL model (red line) when flow rate is 19 ml/s and rotational speed is 100 rpm at different radial locations: (a) $r = 0.148$ m (b) $r = 0.149$ m (c) $r = 0.150$ m(d) $r = 0.151$ m

4.4 Parametric Study

4.4.1 Flow Structure over the Disk

According to earlier experimental studies [6, 5], several flow regimes can be observed: smooth, spiral, concentric, and break-up. The particular regimes can also be observed with the help of three-dimensional evolutionary model. We have produced a phase diagram to visualise the different regimes and the corresponding operation conditions for fluids with different properties. As can be seen from Fig. 4.4, the wave regimes can be determined by the dimensionless numbers in the IBL model i.e. λ and r_{disk}, which are characterised by rotational speed, fluid density, viscosity, and surface tension. An increase in λ value will tend to make the waves smooth, while a decrease in λ will further steepen the surface waves, eventually leading to wave breakup over the disk. The parameter λ is associated with relative significance of inertia and increasing λ corresponds to decreasing the effect of inertia, leading to smaller-amplitude waves and, for a sufficiently large value, even a smooth film.

Also, r_{disk} implicitly affects the wave evolution as it is proportional to the Ekman number due to the scaling presented in this paper, as can been seen in Siesoev *et al* [2] and Matar *et al* [26], where the Ekman number is defined as $Ek = \frac{\nu}{\Omega H_c^2}$, with a scaling based on Nusselt solution $H_c = \left(\frac{Q_C \nu}{2\pi\Omega^2 R_C^2}\right)^{1/3}$. If R_C is chosen to be the disk radius R_{disk}, then $r_{disk} = Ek^{3/4}$. Increasing the r_{disk} tends to produce concentric waves instead of spiral waves due to the increased effect of the Coriolis force.

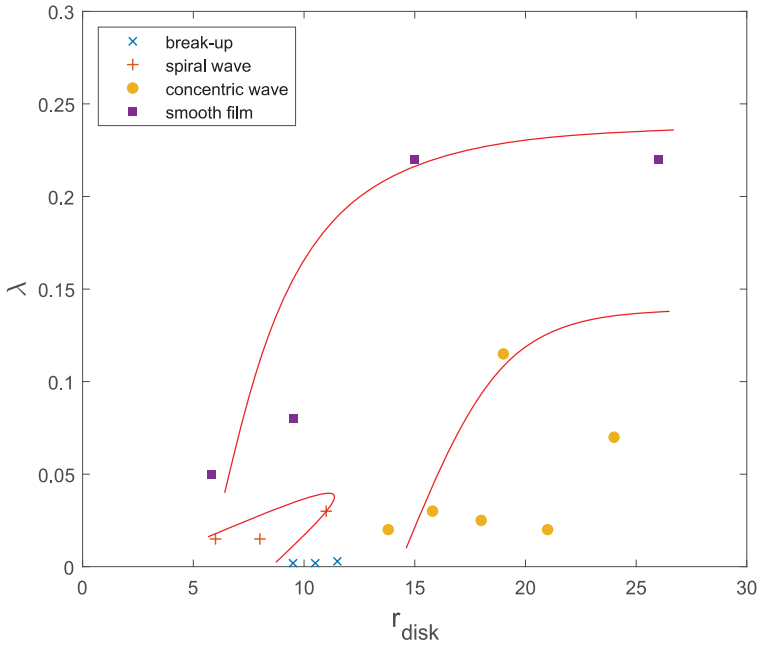

Figure 4.4: Phase diagram of flow patterns with varying dimensionless parameters: λ and r_{disk}

As in Fig. 4.4, different types of waves (and the corresponding operating condition) are observed: smooth films represented by purple squares, spiral waves by red vertical crosses circles, concentric waves by yellow circles and wave break-ups by blue crosses. Subject to the limitation of the model, the highest rotational speed is 600 rpm as higher rotational speed leads to numerical stability issues, resulting in difficulties in resolving high spatial derivatives associated with very low λ values. Typical waves observed are shown in Fig. 4.5 , with operation conditions corresponding to the phase diagram Fig. 4.4. More wave structures observed in the CFD simulations are presented in Appendix A.

Here the CFD results are referenced in order to present the three-dimensional wave structure in this section. The same wave structures are observed from numerical solutions of IBL model, as shown in Fig. 4.6 and 4.7, which is the focus of the analysis in this chapter.

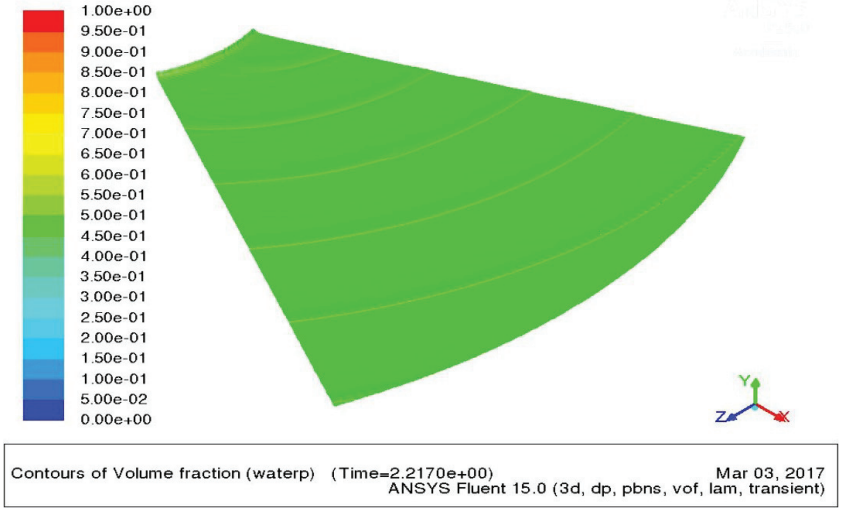

Figure 4.5: Examples of wave structures produced by CFD simulations, with $\lambda = 0.02$ and $r_{disk} = 7$

Spiral waves are one typical type of waves in experimental research and are observed in the numerical simulation of the non-axisymmetric model. As can be seen in this diagram, under certain operating conditions spiral waves are observed in numerical solutions e.g. flow rate of 12 ml/s and rotational speed of 160 rpm. The evolution of three-dimensional spiral wave is shown in Fig. 4.6: at earlier times, small-amplitude waves emerge and travel radially towards the disk periphery. These waves gradually steepen and become non-linear before forming spirals during the transit. These large-amplitude waves are followed by smaller capillary ripples and separated by flat films. Similar to the one-dimensional model [26], two distinct regions appear within the disk: a relatively smooth region near the inlet, and a steep wavy region further downstream near the periphery.

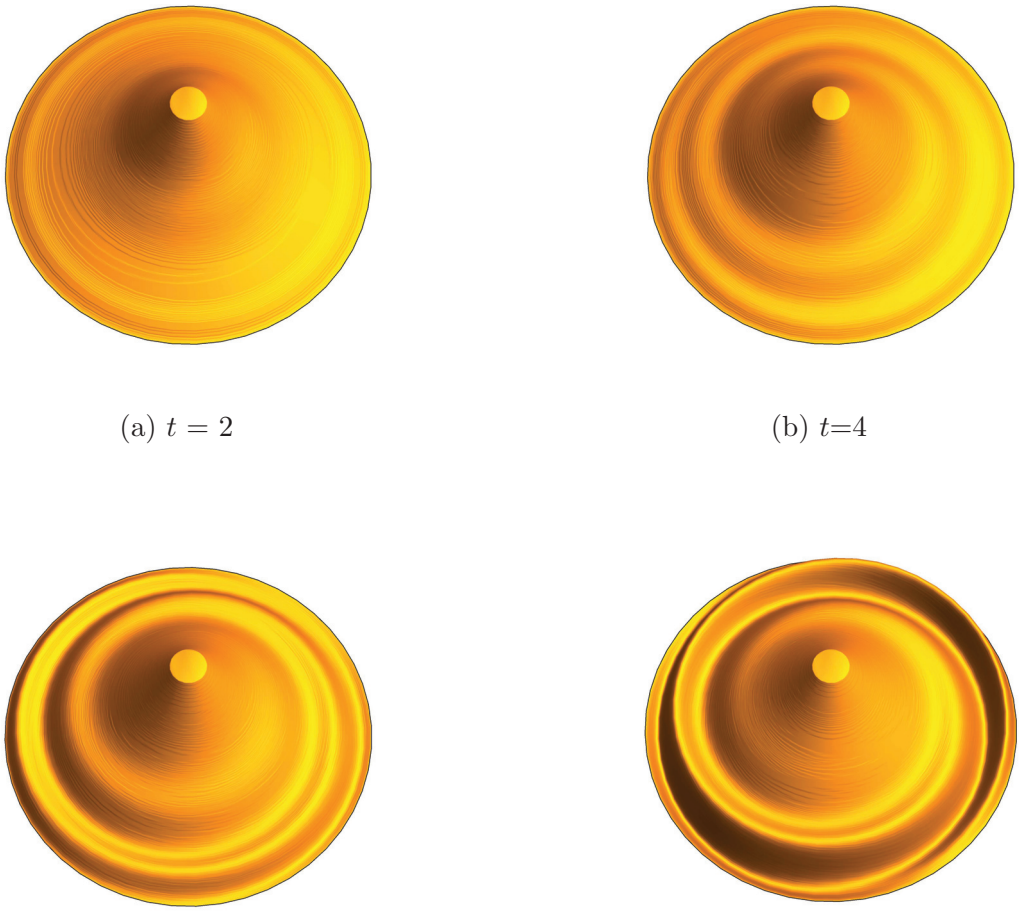

(a) $t = 2$ (b) t=4

(c) $t = 6$ (d) $t = 8$

Figure 4.6: Evolution of 3D spiral waves under the operating condition: 13 ml/s and 200 rpm at different dimensionless time steps, produced by IBL model solutions, for $\lambda = 0.02$ and $r_{disk} = 7.5$

Under certain operating conditions, usually moderate rotational speed and low initial flow rate, e.g. if the same combination of 7 ml/s and 150 rpm is applied in this model as in the paper Charwat et al. [6], which leads to $\lambda = 0.05$ and $r_{disk} = 9.0$, concentric waves are observed in Figure 4.7. The evolution of concentric waves is similar to that of spiral waves, in that they start from small-amplitude waves near the inlet region and gradually travel towards the disk periphery, and large amplitude-waves are accompanied by small-amplitude capillary ripples. However, instead of forming spirals, concentric rings emerge over the disk surface, separated by flat film in between. Also, compared to spiral waves, concentric waves tend to have smaller

amplitude, especially in the periphery of the disk.

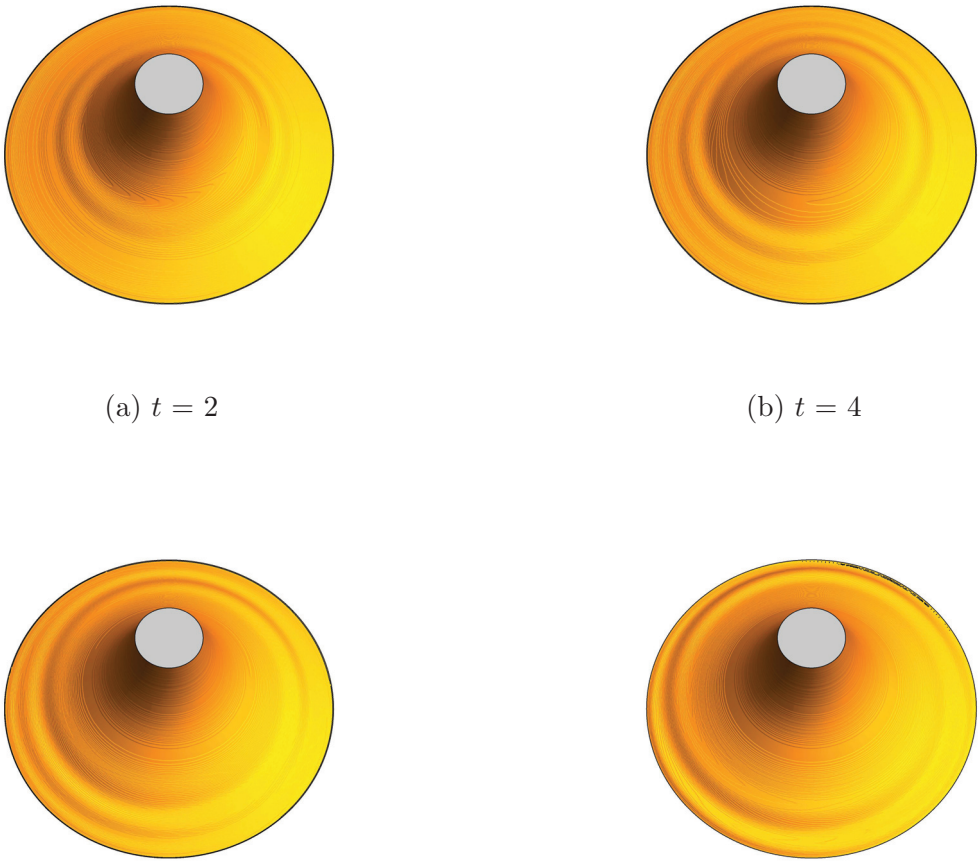

(a) $t = 2$ (b) $t = 4$

(c) t=6 (d) $t = 8$

Figure 4.7: Evolution of 3D concentric waves under the operating condition: 7 ml/s and 150 rpm at different dimensionless time steps, produced by IBL model solutions, for $\lambda = 0.05$ and $r_{disk} = 9$

4.4.2 Direct Comparison of Waves

Both numerical solutions of the IBL model (Eqn. (4.4)-(4.6)) and the CFD simulation predictions give a good qualitative agreement with the experiments in terms of wave structures. In Fig 4.8, the left panel shows concentric waves that were observed experimentally [6] for a rotational speed of 60 rpm and an inlet flow rate of 12 ml/s. The right panel depicts the concentric wave structure over the disk produced from the IBL model with dimensionless parameter $\lambda = 0.05$,

which characterises the experimental conditions. As found in the experiment and numerical solutions, gradually increasing the inlet flow rate leads to the transition from smooth films to concentric wave structure with small-amplitude waves.

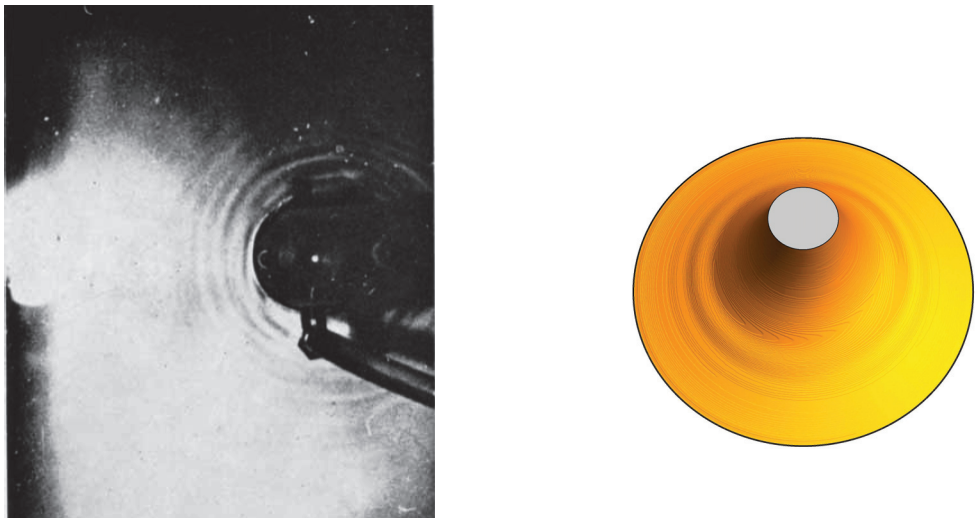

(a) (b)

Figure 4.8: Comparison of concentric waves from experimental result [6] (a) where rotational speed $\Omega = 60$ rpm and inlet flow rate $Q_c = 12$ ml/s and numerical solutions of Eqn. (4.4)-(4.6) (b) with $\lambda = 0.05$, $r_{disk} = 12$ translated from the same rotational speed and flow rate

In more recent research [11], irregular waves are observed with similar flow rate of 10.8 ml/s but a higher rotational speed of 600 rpm, which corresponds to $\lambda = 0.006$ and $r_{disk} = 10$. Due to the limitations of λ values in the three-dimensional IBL model, the IBL solutions are not valid under this experimental condition, which naturally leads to the application of CFD simulation. As shown in Fig 4.9, this irregular wave structure are also captured in the CFD simulation under the same experimental conditions. Spiral-like waves emerge close to the inlet region and the irregular waves begin to form near the disk periphery due to the interactions between waves induced by relatively high rotational speed.

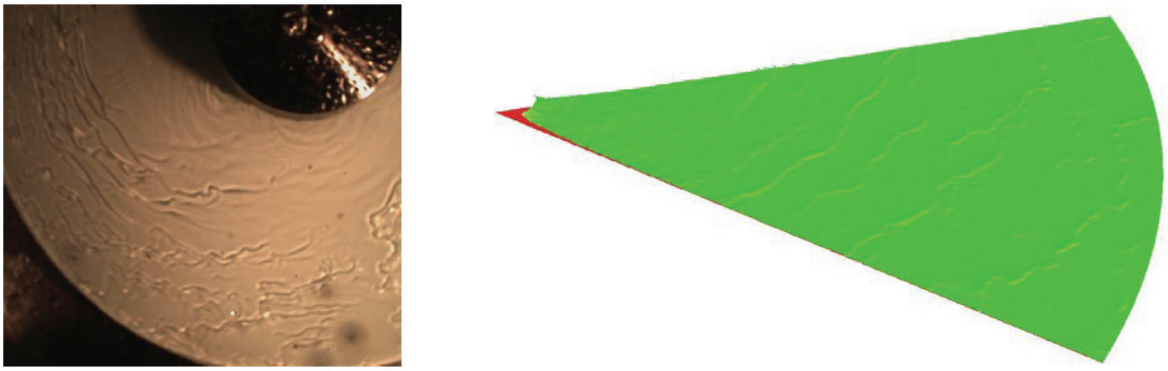

(a) (b)

Figure 4.9: Comparison of irregular waves from experiment [11] (left) with rotational speed $\Omega = 600$ rpm and inlet flow rate $Q_c = 10.8$ ml/s , and CFD simulation (b) under the same condition

4.4.3 Interfacial Waviness

In order to quantify the effect of different waves regimes on the flow dynamics, we apply the dimensionless, integral measure of three-dimensional interfacial waviness, extending from one-dimensional model of a thin film over spinning disks from Matar [55] :

$$W = \sqrt{\int_0^{t_{end}} \int_0^{2\pi} \int_{rin}^{rdisk} r(h - h_N)^2 dr d\theta dt} \tag{4.11}$$

where $h_N = 3^{1/3} r^{-2/3}$ is derived from an approximation of the steady solution at large value of r (Nusselt solution) and the original one-dimensional formula is $W(t) = \sqrt{\int_{r_{in}}^{r_{disk}} r(h - h_N)^2 dr}$.

In the regime of spiral waves, these wave shapes do not vary with radius in the steady-state solution, similar to the finding in the work of Sisoev *et al.*[62]. Thus, we consider the wave hump's projections onto the plane (r, θ) which are characterised by the Archimedean spiral equation $r = \alpha(\theta - \theta_0) + r_0$, where r_0 represents the centrepoint of the spiral from the origin and the parameter α controls the distance between the loops in the spiral (the spiral waves converge into concentric waves with $\alpha = 0$). In this case, the deviation angle β which characterises the spiral deviation from a circle is deduced from the Archimeadean equation and shown below:

$$\beta = \arctan\left(\frac{1}{r}\frac{dr}{d\theta}\right) = \arctan\left(\frac{\alpha}{r}\right) \tag{4.12}$$

Fig. 4.10 shows the dependence of spiral angle β on the disk radius, based on numerical simulations of the PDEs leading to spiral wave structures, with the λ and r_{disk} values in the spiral wave region in the phase map Fig. 4.4. More specifically, Fig. 4.10 (a)-(d) corresponds to the computations with $\lambda = 0.05$, $\lambda = 0.02$, $\lambda = 0.01$, $\lambda = 0.005$ respectively and $r_{disk} = 7.5$ in all cases. As seen Fig. 4.10, with fixed r_{disk} and decreasing λ values, the spiral deviation β increases, indicating that the wave regime transitions from concentric-like waves to spiral waves. Each spiral wave structure can be characterised by one single parameter α, which we use to associate the interfacial waviness W with one particular spiral wave structure.

Table 4.2: Three-dimensional interfacial waviness W of different spiral waves

α	0.1	0.8	1.2	1.5
W	1	1.33	1.53	1.7

As can be seen from the Table 4.2, different interfacial waviness are obtained under the spiral wave regime, and these figures are normalized against that of concentric-like wave regime (where $\alpha = 0.1$). The figure α from the top row of Table 4.2 is obtained by approximating the numerical solution of spiral shape with Archimedean spiral, using the formula in Eqn (4.12), while the corresponding W in each case is calculated via the integral in Eqn (4.11), based on the numerical solution $h(r, \theta, t)$ i.e. film thickness of spiral waves over the entire disk corresponding to the particular α, where the dimensionless parameters are: $r_{in} = 0.5$, $r_{disk} = 7.5$ and $t_{end} = 10$. Increased interfacial waviness is achieved during the transition from concentric waves to spiral waves, due to their being large-amplitude waves and increased interaction of neighbouring waves near the edge of the disk.

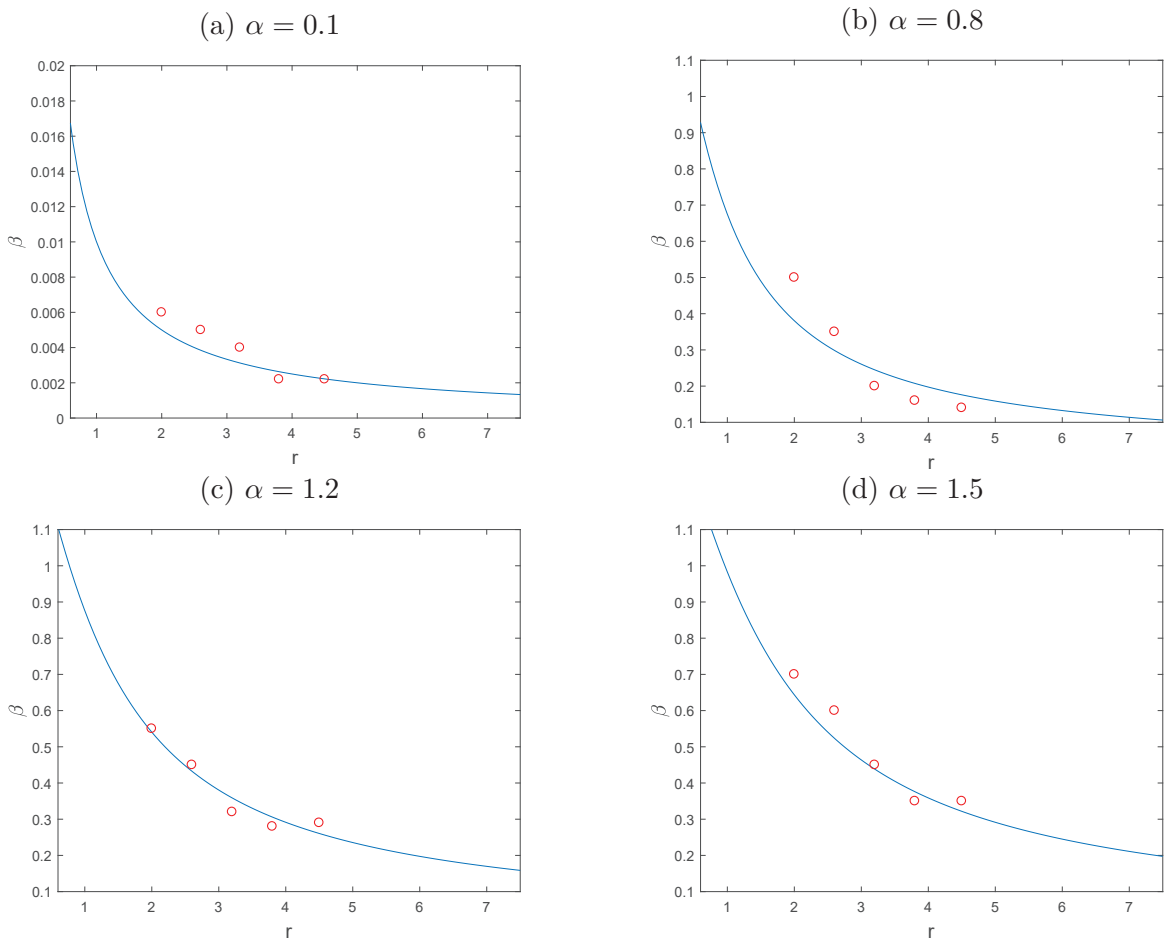

Figure 4.10: Spiral deviation from a circle, β, as a function of the radial coordinate for $\alpha = 0.1, 0.8, 1.2, 1.5$ from (a) to (d) in Eqn. 4.12, shown by the solid blue line, and β values measured directly from the projections of wave humps based on the numerical solution $h(r, \theta)$, shown by the open red circle, for $r_{disk} = 7.5$, $\lambda = 0.05, 0.02, 0.01, 0.005$ from (a) to (d)

4.5 Conclusion

The flow and dynamics of three-dimensional unsteady wavy liquid films over spinning disks were numerically analysed using integral boundary layer (IBL) method, assuming the semi-parabolic functions for the individual velocity components.

In the inner region in the radial direction, the waves remain smooth and flat due to the stabilizing effect from Coriolis force, similar to the result from axisymmetric model. As time evolves, numerical solutions of the three-dimensional IBL model reveal the development of wave regimes: the initial flat film can be transformed into concentric waves or spiral waves, depending on the

dimensionless number λ and r_{disk}, which are related to surface tension and Ekman number, and can lead to surface breakup under extreme conditions. It is found that reducing the value of λ leads to formation of wavy films and large-amplitude waves due to the increased relative importance of inertia, as well as reduced effect of surface tension which stabilises the fluid's surface. Also, the interfacial waviness reveals that an intensification during the transition from smooth films to concentric waves, then to spiral waves. Comparisons between our numerical predictions for film thickness in the radial direction and CFD and experiential data show a good agreement, so is the comparison between the velocity profile under the waves from CFD simulation and that of our assumption.

Chapter 5

Chemical Reactions

In this section, the dynamics of thin film flow over a spinning disk in the presence of first-order chemical reaction is studied, under the axisymmetric approximation. Also, comparison with previous studies is conducted, i.e. mass transport analysis associated with the flow from Matar *et al.* [26] and temperature profile induced by chemical reaction in the evolution equations from Prieling and Steiner [12].

5.1 Evolution Equations

The full set of equations is exactly the same as those in Chapter 3. However, due to the extra complexity introduced by chemical reactions, the evolution equations are reduced by removing the azimuthal dependencies, leading to:

$$h_t + \frac{1}{r} f_r = 0 \tag{5.1}$$

$$f_t + \left(\beta_{11} \frac{f^2}{rh}\right)_r - \beta_{13} \frac{g^2}{r^2 h} = \lambda^2 r h \kappa_r - \frac{3f}{h^2} + r^2 h + 2g \tag{5.2}$$

$$g_t + \frac{1}{r}\left(\beta_{21} \frac{fg}{h}\right)_r = -\frac{5}{2}\frac{g}{h^2} - 2f \tag{5.3}$$

$$C_{b_t} + \frac{3\beta_{41}}{2rh} C_{b_r} + \frac{3\beta_{41} - 2}{2rh} C_b f_r = -3Sc^{-1}\frac{c}{h^2} - \frac{3}{2} DaI \tag{5.4}$$

$$\Theta_t + \frac{3}{2rh}\beta_{51} f \Theta_r + \frac{3\beta_{51} - 2}{2rh}\Theta f_r = -Pe^{-1}\frac{3\Theta}{h^2} + \frac{3}{2}\frac{Da\Theta}{Pe}I \tag{5.5}$$

5.2 Results

In this section, we present a discussion of the steady and numerical solutions of the evolution equations that describe the non-isothermal flow and mass transfer in the film. This is preceded by a brief description of the numerical procedure used to carry out the computations. Note that the notation C_b represents concentration, and in order to distinguish from angle θ, we use the notation Θ for temperature.

5.2.1 Numerical Procedure

The numerical procedure is based on the use of the finite-difference method to discretise the spatial and temporal derivatives that appear in Eqs. (3.23)-(3.38), which govern the evolution of the film thickness, volumetric flow rates, concentration and temperature, respectively.

Numerical solutions for h, f, g, C, and θ starting from the following initial conditions:

$$h = 3^{1/3} r^{-2/3},\ f = 1,\ g = 0,\ C_b = -1, \Theta = 0. \tag{5.6}$$

These solutions are obtained subject to the following boundary conditions at the disc inlet, $r = r_{in}$:

$$h = 3^{1/3} r_{in}^{-2/3},\ f = 1,\ g = 0,\ C_b = -1,\ \Theta = 0, \tag{5.7}$$

and decay conditions at the periphery of the disc, $r = r_{disk}$. The set of parameters is within the typical range: $0 \leq Da \leq 10, 1 \leq Pe \leq 1000, 1 \leq Sc \leq 1000$, with fixed $\lambda = 0.01$ $r_{in} = 0.6$ and $r_{disc} = 7.5$ for all cases when investigating the effects of the dimensionless numbers. The Da from 1 to 10 generally corresponds to conversion of reaction from 10% to 90% [87]. The Sc range is set above as it is the typical range of values for gas-liquid diffusive system. The Peclet number Pe is the same as Prandtl number Pr in terms of value, due to $Re = 1$ in our

scalings. Pr is 0.71 for most common gases at room temperature, and liquids have higher Pr numbers, with values as high as 10^5 for some oils [88]. The number of grid points used to carry out the computations is 1500; convergence was achieved upon mesh refinement, with details in the Appendix B. The steady solutions of the evolution equations are presented next.

5.2.2 Steady Solutions

In this section, we present a set of steady solutions for Eqs.(5.1) - (5.5). These solutions are presented in the Fig. 5.1, obtained by solving the following equations (5.8) - (5.12)

$$f = 1, \tag{5.8}$$

$$\frac{d}{dr}\left(\beta_{11}\frac{1}{rh}\right) - \beta_{13}\frac{g^2}{r^2h} = (\beta_{15} - \beta_{14})\frac{1}{h^2} + r^2h + 2g, \tag{5.9}$$

$$\frac{1}{r}\frac{\partial}{\partial r}\left(\beta_{21}\frac{fg}{h}\right) = -\beta_{23}\frac{g}{h^2} - 2, \tag{5.10}$$

$$\frac{(3\beta_{41} - 2)}{2rh}\frac{dC_b}{dr} = \frac{-3C_b}{Sch^2} - \frac{3}{2}Da\ I, \tag{5.11}$$

$$\frac{(3\beta_{51} - 2)}{2rh}\frac{d\Theta}{dr} = \frac{-3\Theta}{Peh^2} - \frac{3Da\phi}{2Pe}Da\ I. \tag{5.12}$$

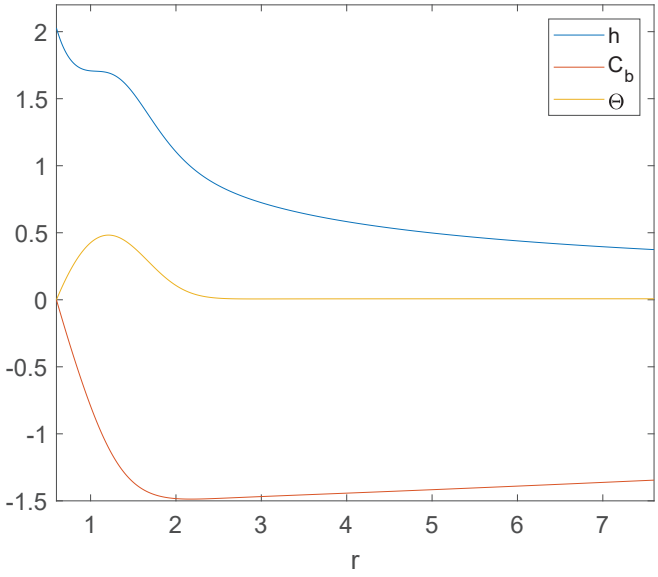

Figure 5.1: Waveless profile of film thickness, concentration and temperature, for $\lambda = 0.01$, $r_{disk} = 7.5$, $Da = 1$, $Pe = 1$ and $Sc = 556$

5.2.3 Parametric Study

We present the results of the film evolution in the presence of the first-order chemical reaction in the section, by solving the Eqns. (5.1) - (5.5). As shown in Figure 5.2, during the early stages of the flow small-amplitude waves emerge near the inlet, which travel across the disc towards its periphery, gaining in amplitude, and becoming nonlinear before reducing the amplitude and diminishing at later times. There is evidence of wave interaction between large-amplitude waves and smaller-amplitude waves downstream. Inspection of Fig. 5.3 also reveals the existence of two distinct regions: a smooth region near the inlet, whose shape remains steady following its evolution during the earliest stages of the flow; and, a wavy region downstream, near the disc periphery. Similar observations were made by [26, 60] who studied the film evolution in the absence of chemical reactions.

As seen in Fig. 5.2, the profile of volumetric flow rates f and g follows the same pattern as in the film thickness h, where they start with initial conditions ($f = 1$ and g from steady-state solutions) and gradually deviate due to the formation of waves, propagating towards the disk periphery. The amplitude of the flow rates initially start to increase, due to the wave induction,

and finally decreases and converges to waveless solutions. In Fig. 5.2 (c), the development of azimuthal volumetric flow rate is shown. Here, it is seen that this flow rate remains negative over the majority of the disk radius, suggesting that azimuthal flow rates act as retarding effect on the overall development of thin film flow across the disk. This is in agreement with the result in Matar *et al.*, who also mentioned decreasing Eckman number will further strengthen the effect.

The evolution of the concentration and temperature fields appears to follow that of the waves: large-amplitude waves are generated at an early stage in time near the inlet region, propagating towards the disc periphery with the accompany of smaller-amplitude waves. As shown in Fig. 5.3, a smooth profile for concentration and temperature is observed at early times and the profile exhibits large-amplitude wave structure in response of the formation of h. It is worth noting that a peak structure is formed relatively close to the inlet region in terms of temperature. This is due to combined effect of convective terms, which try to decrease the magnitude of the temperature due to decreased film thickness and conductive terms, which increase the temperature due to an increase in temperature gradient, in the momentum and energy conservation equation, accompanied by the source term I in Eqn. 5.5, introduced by the first order chemical reaction, which exerts a significant influence on the temperature. The value of I across the disk radius is shown in Fig. 5.4, the value varies significantly near the inlet region when $r < 2$, where the peak forms in the temperature profile. This observation of temperature profile Θ is different from Prieling and Steiner [12], where the temperature is monotonically growing w.r.t disk radius, as the source term in the heat convection-diffusion equation is ignored in their study.

(a)

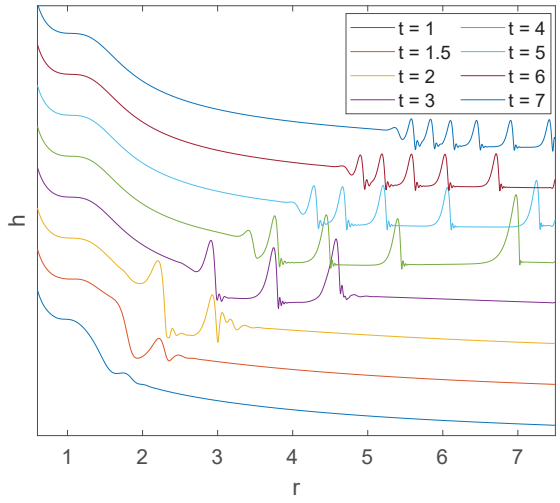

(b)

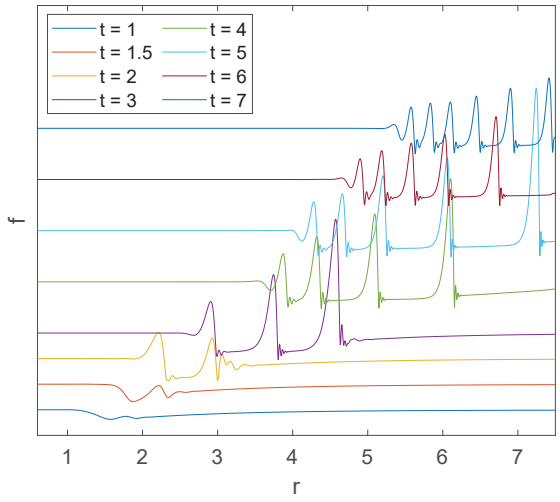

(c)

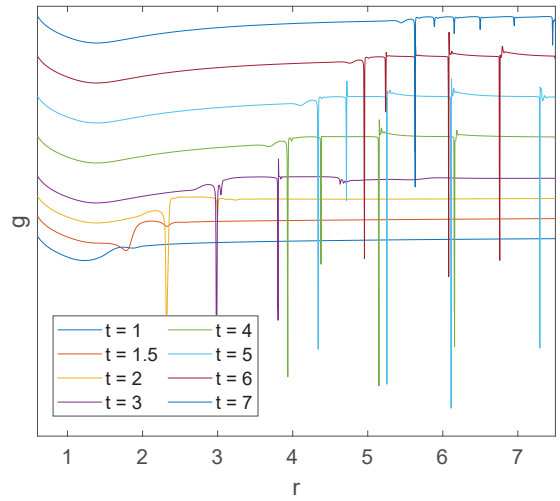

Figure 5.2: Spatio-temporal profile of the film thickness h and volumetric flow rates f and g, at dimensionless times $t = 1, 1.5, 2, 3, 4, 5, 6, 7$ respectively, where $\lambda = 0.01$, $Da = 5$, $Pe = 1$, $Sc = 556$

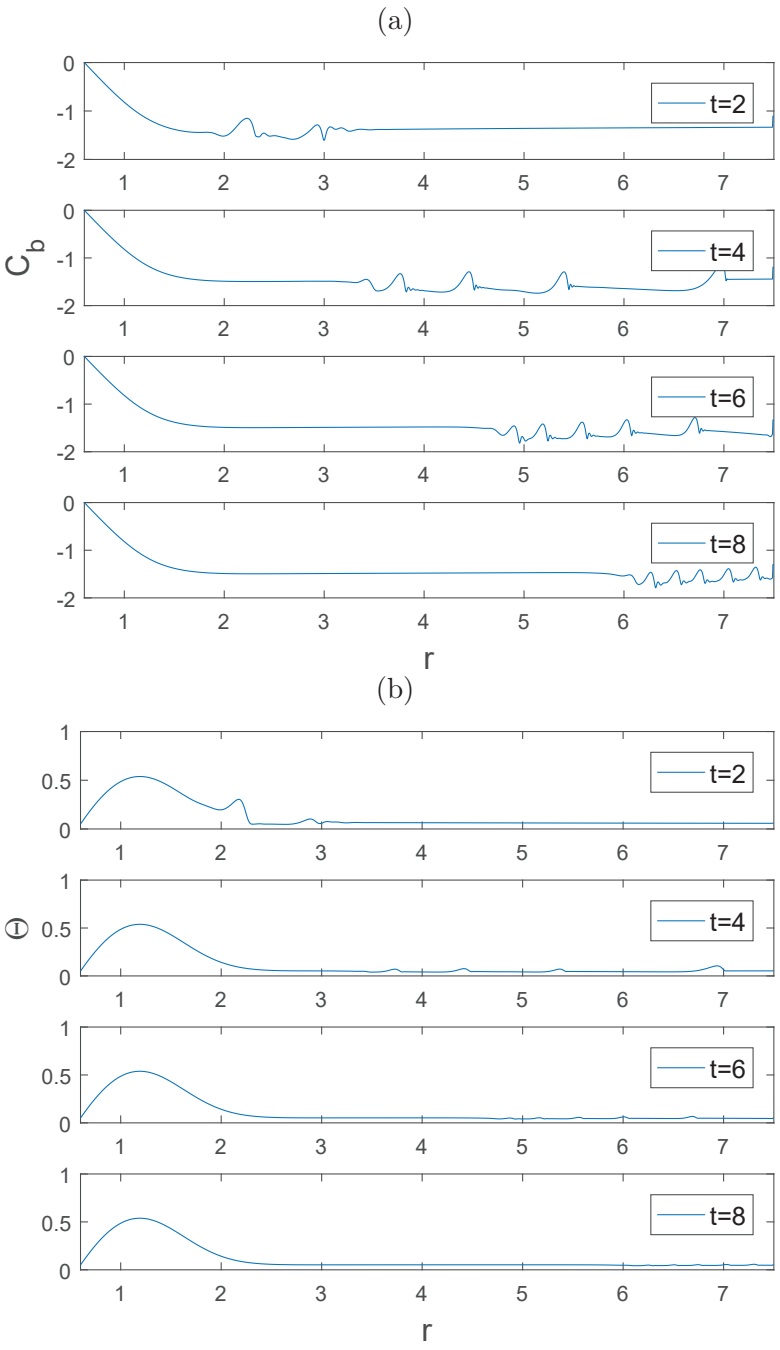

Figure 5.3: Spatio-temporal evolution of C_b and Θ generated using equations (21)-(24) at dimensionless time units $t = 2, 4, 6, 8$ respectively, where $\lambda = 0.01$, $Da = 5$, $Pe = 1$, $Sc = 556$

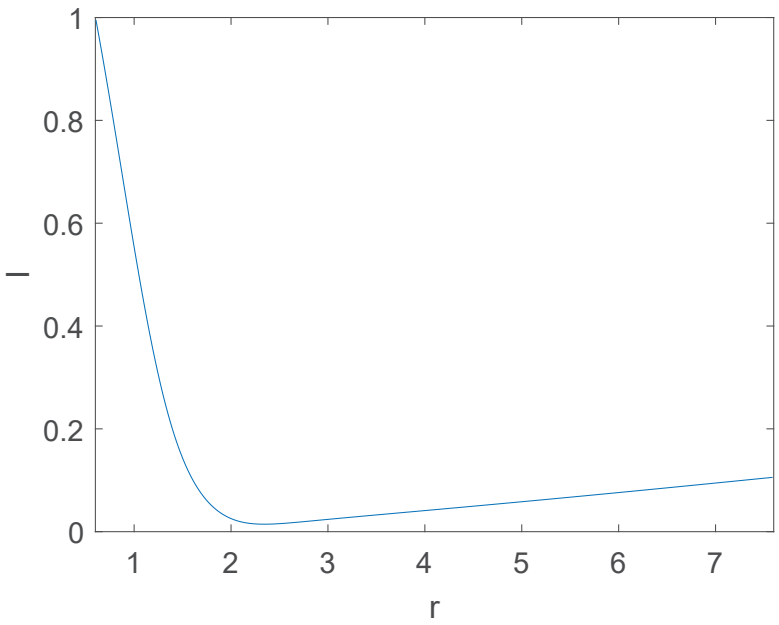

Figure 5.4: The source term I profile in the steady-state equation across the disk radius, where $\lambda = 0.01$, $Da = 5$, $Pe = 1$, $Sc = 556$

After presentation of the evolution of flow characteristics of interest (film thickness h, concentration C_b and temperature Θ profile), we examine the individual dimensionless numbers, i.e. Da, Pe, Sc and their effects on the flow evolution as they govern the chemical reaction, heat and mass transfer.

First, the effect of Damkohler number Da is examined, which represents a ratio of chemical reaction rate to convective mass transfer rate. In Fig. 5.5 (a)(c)(e), while increasing the Da, mean concentration C_b level is decreasing accordingly at different time steps, which means that due to the relative importance of chemical reaction, the reactant is consumed faster than it is transferred by convection and this leads to faster depletion of the reactant because of the reaction undergoing. Also, it is observed that the concentration decrease at a faster rate and reach the equilibrium at an earlier stage with $Da = 5$, compared with $Da = 1$. However, there is a limit on the decrease of concentration and in later stage with higher Da, which corresponds to the limited consumption of reactant in the film when concentration approaches its lower boundary.

Fig. 5.5 (b)(d)(f) shows the evolution profile for mean temperature with increasing Da, with high Da number the peak of the mean temperature is higher e.g. when Da is 1 the peak reaches

0.3 and when Da is 5, the temperature increases significantly to the level of 0.6 at a faster rate. Also, it is noted that the temperature is still higher where the waves occur at later stages when $Da = 5$, and the difference in the temperature profile caused by Da is greater than that of concentration profile where at later stages in time the concentration profiles with different Da almost overlap.

(a) $t = 2$ (b) $t = 2$

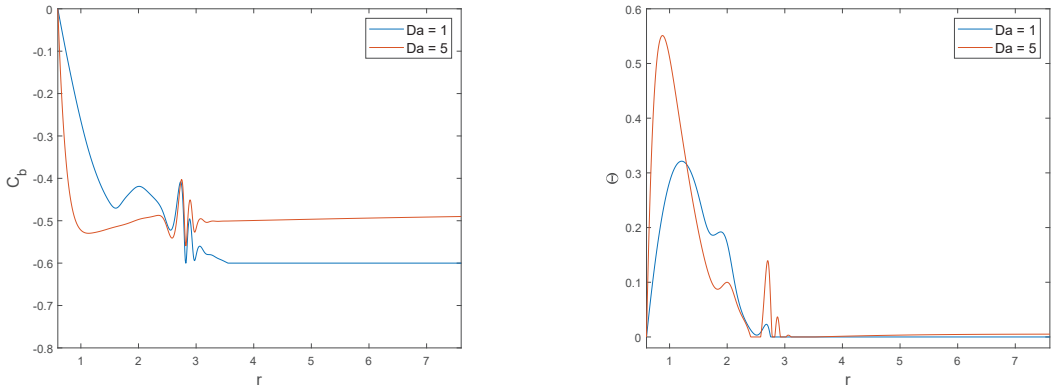

(c) $t = 4$ (d) $t = 4$

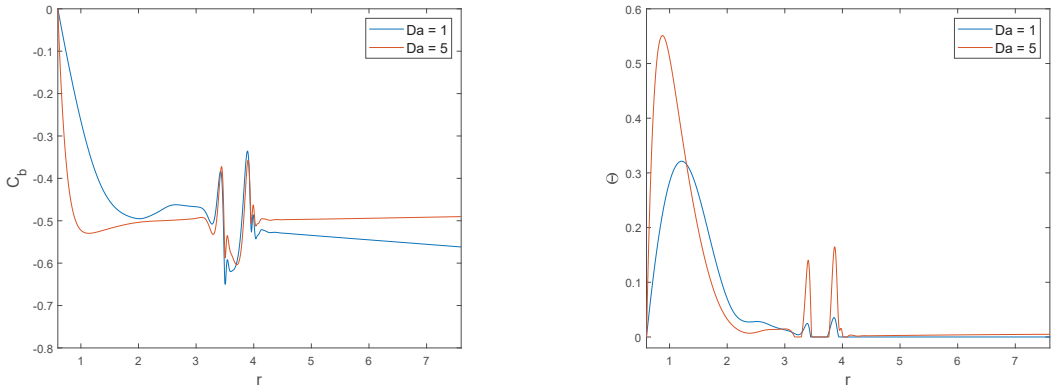

(e) $t = 6$ (f) $t = 6$

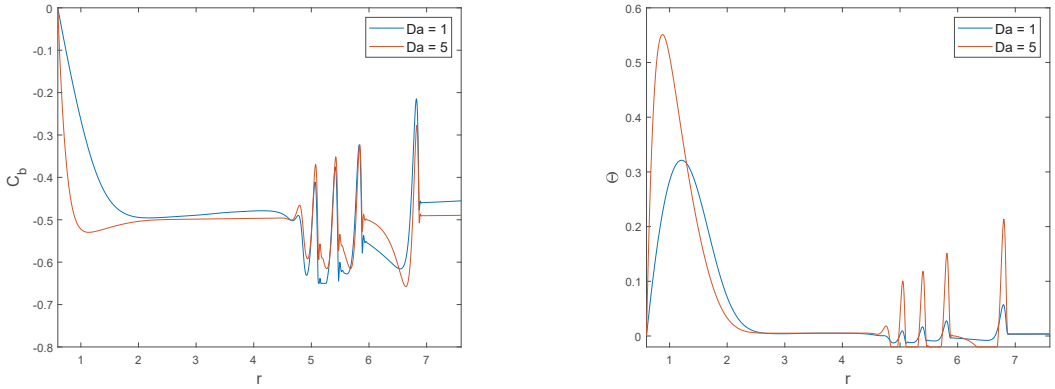

Figure 5.5: Evolution of mean concentration and temperature profile of the reactant at $t = 2, 4, 6$ with varying Da from 1 to 5 and other parameters fixed $Sc = 556$, $Pe = 1$

The effect of Schmidt number is investigated next. As demonstrated in Figure 5.6(a)(b)(c), the wavy evolutionary profile of concentration C_b formed with decreasing Schmidt number from 556 to 5. With the decrease of Schmidt number, the thickness of boundary layer increases, which strengthens the relative significance of diffusion, and this leads to an increase in the magnitude of concentration. Also, this accounts for the increase of concentration after the local minimum near the inlet region, due to the enhanced effect of diffusion as compared with convection. As Sc only determines the mass transfer, temperature profile remains insensitive to decreasing Sc although the momentum conservation and energy conservation equation are coupled, which can be seen in Figure 5.6(d).

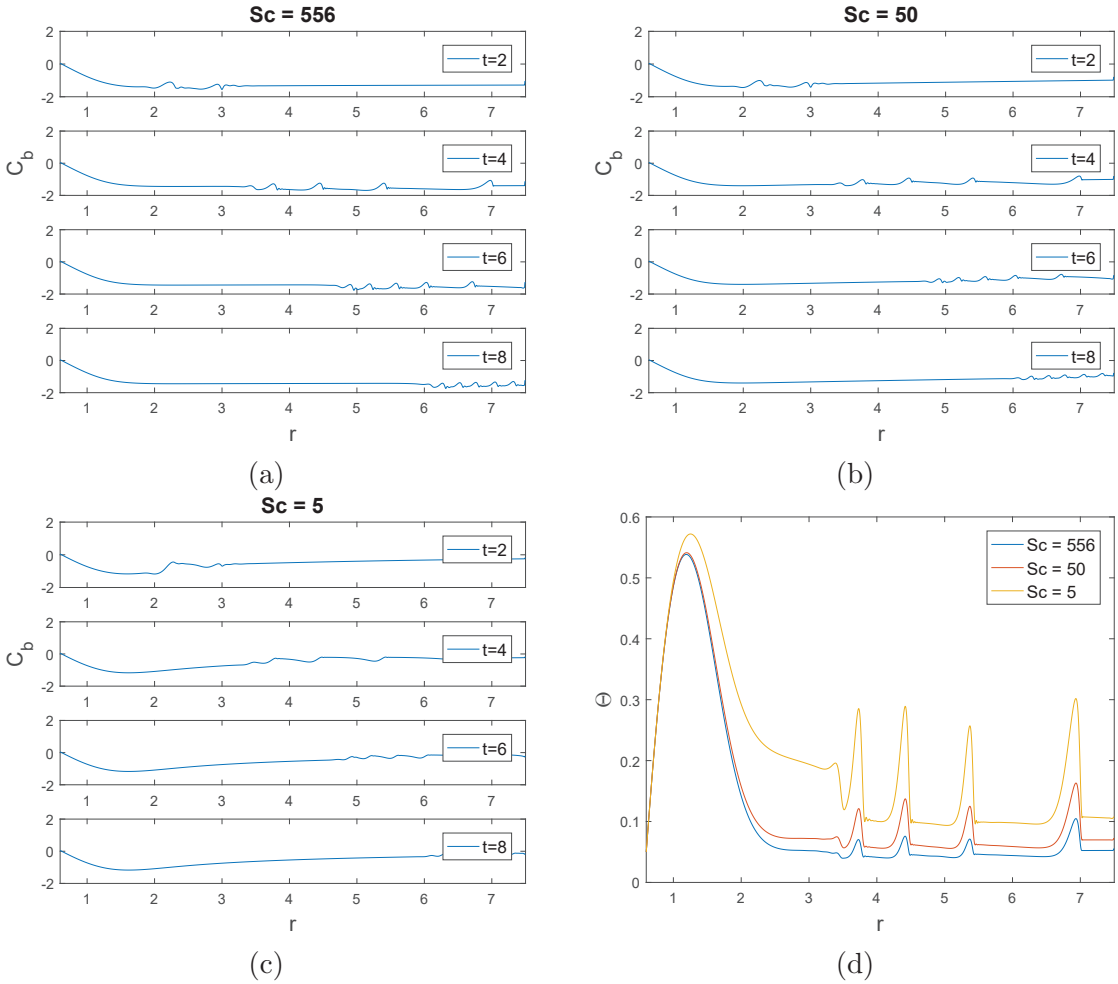

Figure 5.6: Evolution of mean concentration and temperature profile of the reactant at dimensionless time steps $t = 2, 4, 6, 8$ with varying Sc from 5 to 556 and other parameters fixed $Da = 5$, $Pe = 1$, $\lambda = 0.01$

Next, we demonstrate the effect of Peclet number Pe. Analogous to Sc number, Figure 5.7 shows

the spatio-temporal evolutionary profile of concentration and temperature with increasing Pe. 5.7(a) demonstrates that the concentration is almost unchanged with increasing thermal Pe number while 5.7(b)-(d)indicates that value of temperature decreases significantly with the increasing Pe: the peak of temperature decreases from 0.5 to 0.02 when the Pe rises from 1 to 100 because of the decrease of the relative significance of thermal diffusion as well as the heat source compared with convection, which can be proved by Equation (3.17),resulting in the decrease of local temperature accordingly.

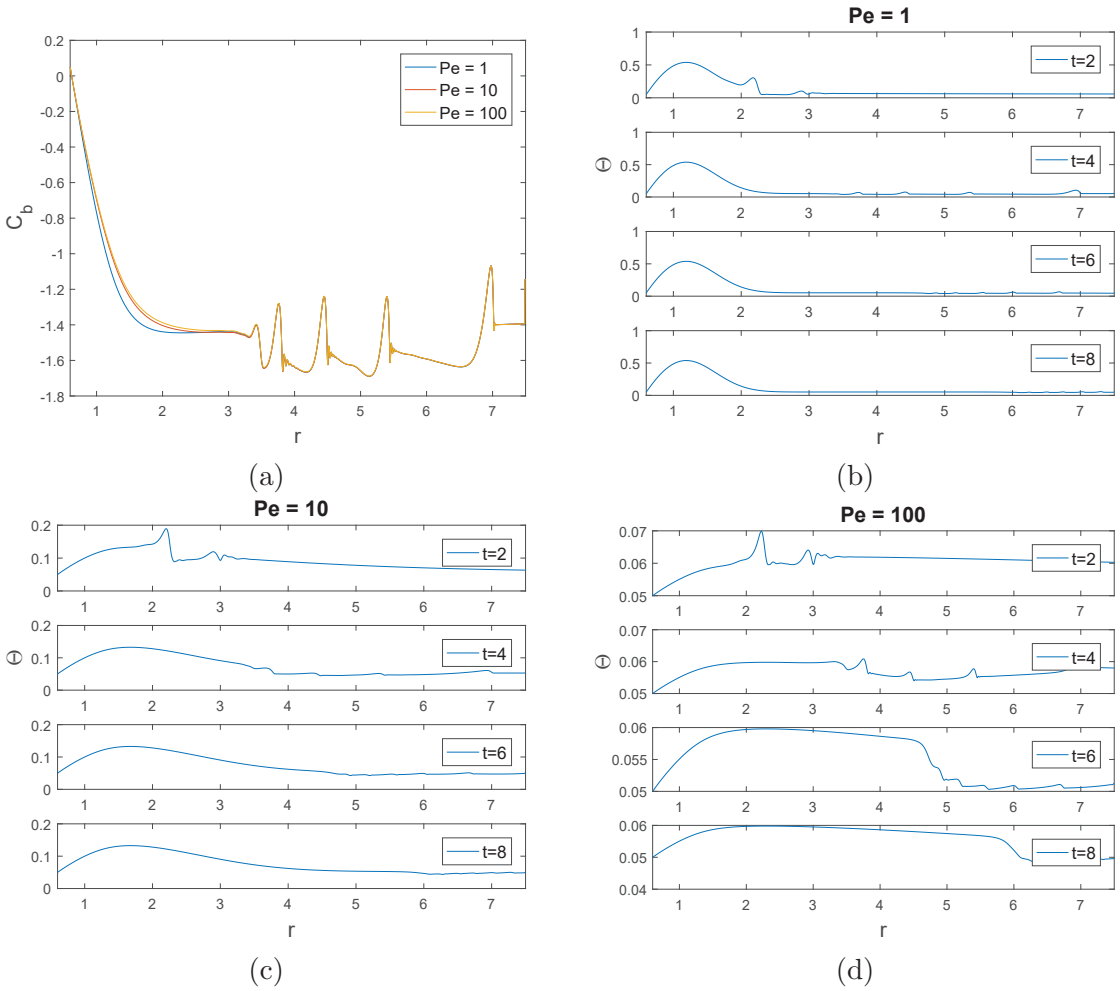

Figure 5.7: Evolution of mean concentration and temperature profile of the reactant at t=2,4,6 8 with varying Pe from 1 to 100 and other parameters fixed $Da = 5$, $Sc = 556$, $\lambda = 0.01$

Afterwards, we compare the time-dependent transient solutions with steady-state solutions, in terms of evolution of temperature and concentration of reactant across the disk radius, as shown in Fig. 5.8 below. It can be observed that due to the formation of travelling waves, the consumption of reactant and the temperature of the film increases compared to the waveless

solutions.

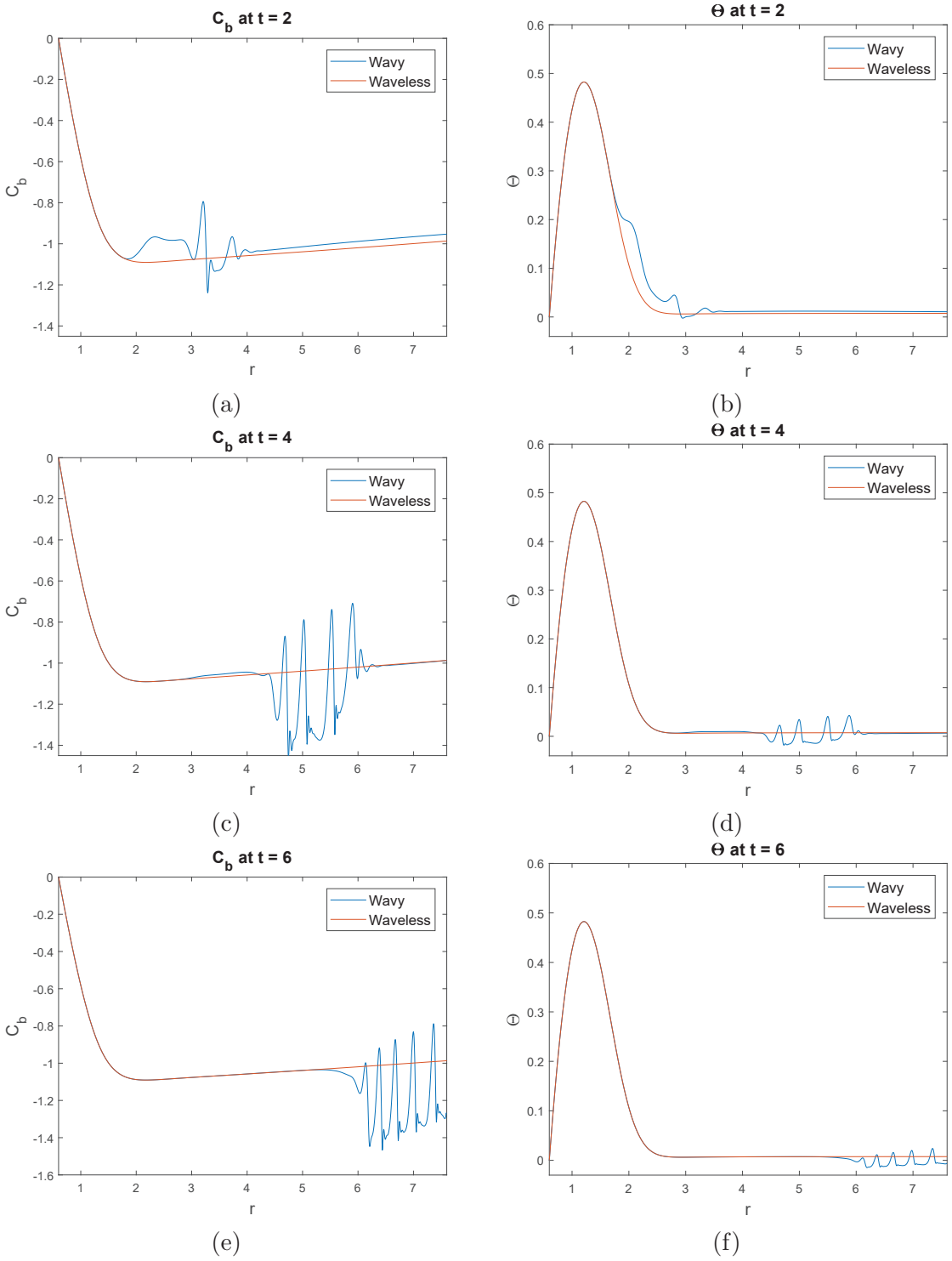

Figure 5.8: Evolution of mean concentration and temperature profile of the reactant, compared with their corresponding steady-steate solutions at dimensionless time units $t = 2, 4$ and 6, for $\lambda = 0.01$, $Sc = 556$, $Da = 5$, $Pe = 1$

In order to quantitatively describe the extent of enhancement mass and heat transfer, the solution of mass and heat transfer coefficient i.e.average Sherwood number (Sh_{avg}) and average Nusselt number (Nu_{avg}) are investigated in presence of first order chemical reaction. Sh_{avg} and Nu_{avg} are defined and derived as below:

The mass flux of solute through the surface is given by

$$\tilde{j} = K_L(C1 - \bar{C}) \tag{5.13}$$

where K_L is the local mass transfer coefficient, $C1$ is the concentration of the solute at equilibrium and $\bar{C}$ is the local average concentration of solute in the liquid film. Within the present model, the mass flux is also represented by:

$$\tilde{j} = D_i \left(\frac{\partial \tilde{C}}{\partial \tilde{z}}\right)_{\tilde{z}=\tilde{h}} \tag{5.14}$$

leading to:

$$K_L = \frac{D_i}{(C1 - \bar{C})} \left(\frac{\partial \tilde{C}}{\partial \tilde{z}}\right)_{\tilde{z}=\tilde{h}} \tag{5.15}$$

The mass transfer coefficient can also be presented in dimensionless form, in terms of local Sherwood number Sh_L:

$$Sh_L = \frac{K_L \tilde{h}}{D_i} = \frac{\tilde{h}}{C1 - \tilde{C}} \left(\frac{\partial \tilde{C}}{\partial \tilde{z}}\right)_{\tilde{z}=\tilde{h}} = \frac{h}{1 - C} \left(\frac{\partial C}{\partial z}\right)_{z=h} \tag{5.16}$$

The average mass transfer coefficient Sh_{avg} over the whole disk is given by:

$$Sh_{avg} = \frac{K_{avg} H_0}{D_i} = \frac{H_0}{(C1 - C)\pi \tilde{r}^2} \int_0^{\tilde{r}} \left(\frac{\partial \tilde{C}}{\partial \tilde{z}}\right)_{\tilde{z}=\tilde{h}} 2\pi \tilde{s} d\tilde{s} = \frac{2}{r^2} \left[Sh_{in} + \int_{r_{in}}^{r} \left(\frac{\partial C_b}{\partial z} s ds\right)\right] \tag{5.17}$$

where $Sh_{in} = \int_0^{r_{in}} \left(\frac{\partial C}{\partial z} s ds\right)$ accounts for the average mass transfer coefficient from disk centre to inlet region $r_{in} = 0.5$, which is computed from the steady state solutions of Eqn. 5.8 - 5.12, while the rest of the terms are from transient solutions of Eqn. 5.1 - 5.5.

Similar to dimensionless average Sherwood number Sh_{avg}, Nu_{avg} is presented to quantify the average heat transfer coefficient over the whole disk, which is defined as below:

$$Nu_{avg} = \frac{2}{r^2}\left[Nu_{in} + \int_{r_{in}}^{r}\left(\frac{\partial\Theta}{\partial z}\right)_{z=0} sds\right] \tag{5.18}$$

where Nu_{in} is Nusselt number at inlet region $r = 0$ to $r_{in} = 0.5$, the detailed derivation of Nu_{avg} is shown in Appendix C.

According to the definition in Eqn. 5.17 and 5.18 above, Sh_{avg} and Nu_{avg} are a function of disk radius and time, similar to other dependent variables in the evolution equations (e.g.h, C_b, Θ). These two measures are obtained via additional numerical integration in the finite difference scheme, using existing variables (r, C_b and Θ) in the evolution equations and stead-state equations.

Figure 5.9 shows the temporal profile of the ratio of wavy Sh and Nu number to waveless Sh and Nu at the outlet $r_{disc} = 7.5$. Increasing the relative importance of inertia, by decreasing the λ from 0.01 to 0.005, leads to the formation of larger amplitude waves and more interaction between waves, as seen in Fig. It is found by earlier researcher stating that the inertia is destabilising effect of the flow [59, 55, 26], and also visually observed in the Chapter 4 where the full three-dimensional wave structure is presented. This implies that the rate of heat and mass transfer increases following the decrease in λ. The dependence of heat/mass transfer characteristics on λ, with other parameters Da, Pe and Sc fixed, is also shown in Fig. 5.9, where the normalised heat/mass transfer coefficients when the flow of solute is leaving the disk, with $\lambda = 0.005$ and 0.01 respectively. For each λ, there is some period where the coefficients are smooth, indicating the waves have not reached the disk periphery and the profile is still waveless. This period is followed by a period of time in which the Sh and Nu exhibit strong large-amplitude oscillations, which shows the stage of the flow with large-amplitude waves passing the disk edge. By comparing the graphs in Fig. 5.9 (a)(b) and 5.9 (c)(d), it can be seen that decreasing λ from 0.01 to 0.005 leads to larger amplitude of Sh and Nu overall and more wave-induced temporal variations after initial smooth period.

Figure 5.10 demonstrates the average Sh and Nu against the steady solution at early, middle and late stages of travelling waves. The definition of Sh_{avg} and Nu_{avg} for steady-state solution is the same as that of transient solution, and the only difference is that the waveless concentration and temperature profile is applied in Eqn. (5.17) and (5.18) whereas in the transient version only the contribution from the inlet region is using the waveless concentration and temperature solution. It can be seen that due to the formation of non-linear travelling waves, mass and heat transfer coefficient are drastically enhanced due to the large-amplitude waves travelling towards the disc periphery compared to the waveless solutions. This reveals that simple analysis of the flow based on the Nusselt theory or steady-state solutions cannot predict the wave-induced enhancement effect on mass and heat transfer. The enhancement of heat transfer is also captured by the IBL model in the study of Prieling and Steiner [12], where they find out that increased waviness means thin liquid layer between surface waves are more easily heated up/cooled down, leading to the enhancement in heat/mass transfer.

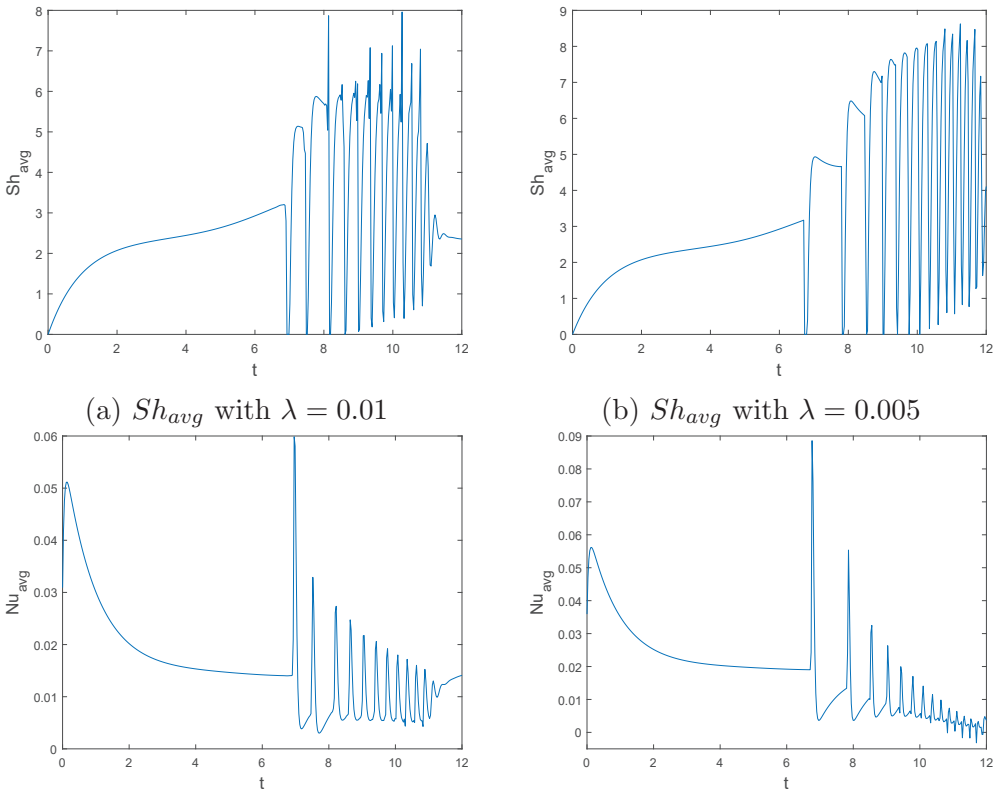

(a) Sh_{avg} with $\lambda = 0.01$ (b) Sh_{avg} with $\lambda = 0.005$

(c) Nu_{avg} with $\lambda = 0.01$ (d) Nu_{avg} with $\lambda = 0.005$

Figure 5.9: Average Sherwood number (Sh_{avg}) and Nusselt number Nu_{avg} with respect to dimensionless time units at the outlet ($r_{disk} = 7.5$), with $\lambda = 0.01$ (left panel) and $\lambda = 0.005$ (right panel) respectively, where $Da = 5$, $Sc = 556$, $Pe = 1$

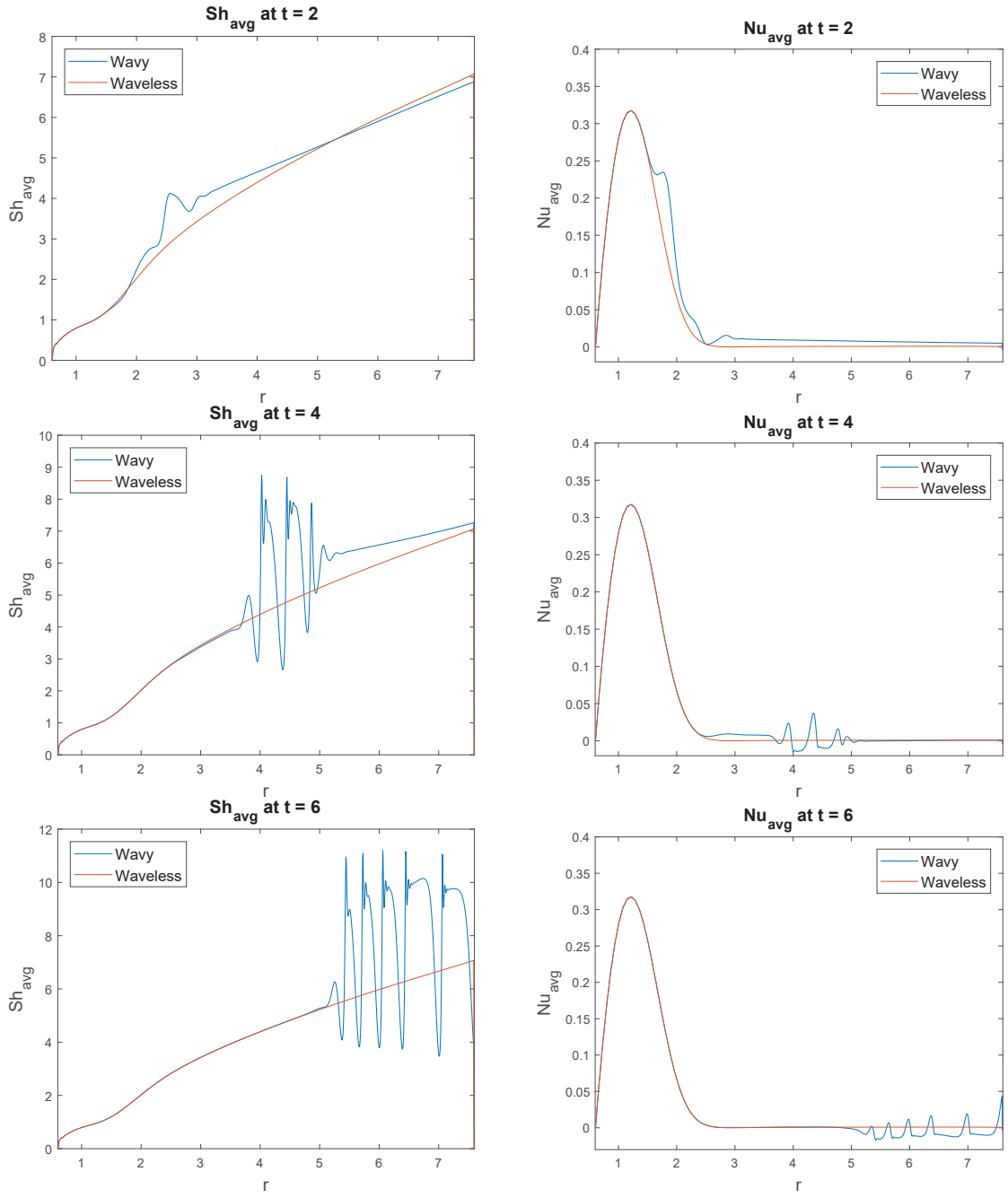

Figure 5.10: Evolution of average Sherwood number Sh_{avg} and Nusselt number Nu_{avg} across the disk radius at different time units $t = 2, 4, 6$, where $Da = 5$, $Sc = 556$, $Pe = 1$

5.3 Conclusion

In this chapter we have investigated the hydrodynamics, mass and heat transfer characteristics of a thin liquid film over a spinning disc, in presence of first order chemical reaction. Integral boundary layer method was applied to obtain a set of partial differential equations for film thickness, volumetric flow rate, concentration of the reactant and the temperature across the film originated from Navier-Stokes, assuming a parabolic profile of velocity, concentration and temperature in vertical direction. These coupled evolution equations were parametrised by dimensionless numbers: a Damkolher number, Da, a Schmidt number, Sc and a thermal Peclet number, Pe which reveal the relative significance of reaction rate, mass diffusion rate and thermal diffusion rate, respectively. A measure of enhancement of mass and heat transfer was characterized by dimensionless number Sherwood number,Sh and Nusselt number, Nu, respectively. Numerical solutions of the coupled partial differential equations were obtained using finite difference method and a parametric study was carried out on order to test the dependence of dynamics on the dimensionless group. The results indicate the formation of large amplitude waves travelling from the inlet region to disk periphery, which gives rise to a drastic enhancement of the mass and heat transfer. Large Da does not change the hydrodynamics of the film, but increase the consumption and reactant within the film and result in higher temperature profile accordingly. Increasing Sc and Pe leads to the decrease of concentration and temperature respectively, due to the change of relative importance of mass and heat diffusion rate. Dimensionless numbers Sh_{avg} and Nu_{avg} indicates that the intensification of heat and mass transfer due to the formation of large-amplitude waves, and this enhancement increases by decreasing the λ, which has a destabilising effect on the flow.

The temperature profile within this model is different from Prieling and Steiner [12], in which the temperature profile is monotonically increasing w.r.t disk radius. This is due to the negligence of the source term in the original heat diffusion convection equation, which acts as the opposite effect on the temperature, compared with the diffusion term. However, enhancement of heat/mass transfer due to the wave-induced flow is presented in both places despite the difference in the temperature profile.

Chapter 6

Artificial Neural Network

In this chapter, we discuss a short-cut towards the dynamics of the flow, by-passing the time-consuming implementation of finite-difference (FD) scheme, via performing neural-network simulation based on the results from existing FD-based runs. In the previous chapters, we discussed the chemical reactions and three-dimensional hydrodynamics of the flow over spinning disks, and the computation of numerical solutions (under IBL theory) is, even though a simplification compared with full Direct Numerical Simulation (DNS), expensive with running time from several hours to days, due to the number of dependent variables in the set of evolution equations (film thickness, flow rate, concentration and temperature), and the nature of multidimensional analysis, significantly leading to increasing number of grid points. One way to bypass this time-consuming computations is to train a "smart" neural network fed from existing FD simulation up to a certain time t_{mid}, and then apply the trained network to predict the evolution of desired variables from t_{mid} onwards.

6.1 Implementation of Neural Network

First, in order to let the neural network work, we need large amount of training data and these data are from previous finite-differences solutions under certain conditions, e.g. λ and r_{disk}. After training of the data, a trained network will be able to predict the evolution of waves

under these conditions. Afterwards, the comparison can be made between the results from neural network and new finite difference scheme directly for the model validation purpose.

We use the Finite Differences (FD) implementation results. The computational geometry is three-dimensional cylindrical system as sketched in Fig. 6.1. The boundary condition in azimuthal direction is periodic, regardless of the angle θ (0 to 2π) we use. The FD model output is film thickness h and volumetric flow rates f and g, which are functions of r, θ and time t.

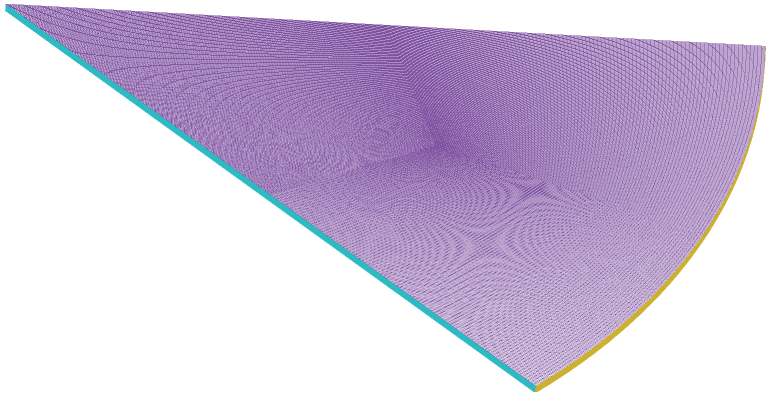

Figure 6.1: A sketch of the computational domain

In the simple case under axisymmetric assumption, the h,f,g are a function of r and t only.

These functional relationships can be obtained from predictions by many advanced regression methods [89], and various software packages [90]. In our spinning disk geometry with the periodic boundary condition in the azimuthal direction, we choose Artificial Neural Network to tackle this problem. The multilayer Neural Network is a powerful nonlinear regression technique, typically with a three-layer architecture: an input layer, hidden layer and an output layer. Each unit in the hidden layer is transformed by a nonlinear function of a linear combination of all the variables in the input layer. After the hidden units are defined, another layer of linear combination connects all the hidden units to the output units. Take Neural Network modelling of function for as an example: suppose there are m input units (samples) and n hidden units, then from input layer to hidden layer unit H_i:

$$H_i = s(a_{0i} + \sum_{j=1}^{m} r_j a_{ji}) \tag{6.1}$$

and the output O generated from hidden units is:

$$O = b_0 + \sum_{i=1}^{n} b_i H_i(r) \tag{6.2}$$

where the nonlinear transfer function s is smooth and usually between 0 and 1,typical examples include: the logistic sigmoid function $s = \frac{1}{1+e^{-x}}$, hyperbolic tangent function tanh $= \frac{e^{2x}-1}{e^{2x}+1}$. The adjustable coefficients a_{0i}; a_{ji}; b_0; b_i are consistently updated and eventually confirmed after consistent training of the NN. Software packages to train neural networks are widely available and we have used the neural network toolbox in Matlab [91] for the spinning disk geometry. The Matlab toolbox applies a three-layer neural network architecture with feed-forward back-propagation mechanism with the Levenberg-Marquardt method to optimize the weight coefficients, which connects the neurons in the input layer. A number of combinations of optimisation algorithms, number of hidden layers and neuron sizes have been experimented, we find out that for one single layer with ten neurons with Levenberg-Marquardt optimisation algorithm produces best results balanced between performance (convergence rate) and robustness.The starting values for the weights are chosen to be normally distributed random numbers close to zero. Too many hidden layers increase the accuracy of nonlinear fitting, however, leads to over-fitting problem. Once the training is finished, Matlab returns a network, which works as functions but doesn't have close-form analytical expression, with optimal weights that relate the input variables to the output and here. The final output (desired dependent variable) can be obtained using the trained network, with suitable inputs inserted.

6.2 Neural Network Training - Chemical Reactions

$$h_t + \frac{1}{r} f_r = 0 \tag{6.3}$$

$$\frac{\partial f}{\partial t} + \left(\beta_{11} \frac{f^2}{rh}\right)_r - \beta_{13} \frac{g^2}{r^2 h} = \lambda^2 r h \kappa_r - \frac{3f}{h^2} + r^2 h + 2g \tag{6.4}$$

$$g_t + \frac{1}{r}\left(\beta_{21} \frac{fg}{h}\right)_r = -\frac{5}{2}\frac{g}{h^2} - 2f \tag{6.5}$$

$$C_{b_t} + \frac{3\beta_{41}}{2rh} C_{b_r} + \frac{3\beta_{41} - 2}{2rh} C_b f_r = -3Sc^{-1} \frac{c}{h^2} - \frac{3}{2} DaI \tag{6.6}$$

$$\Theta_t + \frac{3}{2rh} \beta_{51} f \Theta_r + \frac{3\beta_{51} - 2}{2rh} \Theta f_r = -Pe^{-1} \frac{3\Theta}{h^2} + \frac{3}{2} \frac{Da\Theta}{Pe} I \tag{6.7}$$

As can be seen from the equations above, the film thickness, flow rate, concentration, and temperature are all a function of radial location r and passage of time t under asymmetric assumption.

In order to prepare the data for Neural Network training, we conduct a number of different finite difference implementations. The FD results are saved at equal time intervals in time $\delta t = 0.16$ with time running to $t = 8$ in total, and 1500 intervals in radial direction. Thus, there are 50*1500 =75000 total sample points available, each containing the information of velocity, film thickness, flow rate, concentration and temperature. Then, the data set is divided into three parts by random sampling before the neural network training, usually the most one for the fitting (60% or 45000 samples), another for validation (30% or 22500 samples), and the rest for testing (10% or 7500 samples). The fitting starts by iteratively adjusting the coefficients of the NN to fit the first inputs of the data to the target. Usually the fitting of the data set improves with the increasing number of iterations(epoch), but too many unnecessary iterations also result in over-fitting and degrade the ability of this trained network to make new predictions with new inputs. The validation data are used to detect when this starts to happen and stop the iterations if needed. Finally, the model is checked by comparing its predictions with the testing data(10%) of the whole data set. Different ways of splitting the whole data set have been exploited, including the 70%/15%/15% split by default, and we find out that the fitting performance is relatively insensitive to the split ratio, compared with the number of neurons and hidden layers.

To examine the performance of this nonlinear fitting, Fig.6.2 shows the distribution of the error (Target- Output) for both the concentration and the temperature. As shown in Fig. 6.2, the training, validation and testing data are labelled blue, green and red respectively. The vertical yellow line in the centre indicates zero error. The NN training has given good results from the fact that the level of error (x axis) is very small and most of errors centred around zero. This

is particularly true for training dataset, but the error distribution for validation and testing samples are also in agreement with that of the training data, with very few large errors far away from the centre. Figure 6.3 demonstrates the Mean Squared Error (MSE) with number of iterations (epochs). Both the MSE for concentration and temperature drop sharply with initial 200 iterations and slowly reach convergence in the end. Compared with the concentration profile, temperature profile converges faster initially but takes longer time (931 epochs) for final adjustment in the Neural Network training model, leading to a better fitting result, with final MSE 10^{-5}, which is around 10 times smaller than that of concentration.

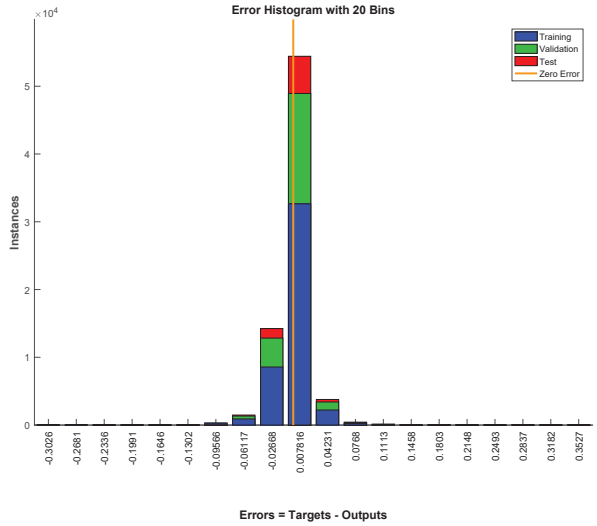

(a) Concentration

(b) Temperature

Figure 6.2: Error for concentration and temperature NN training

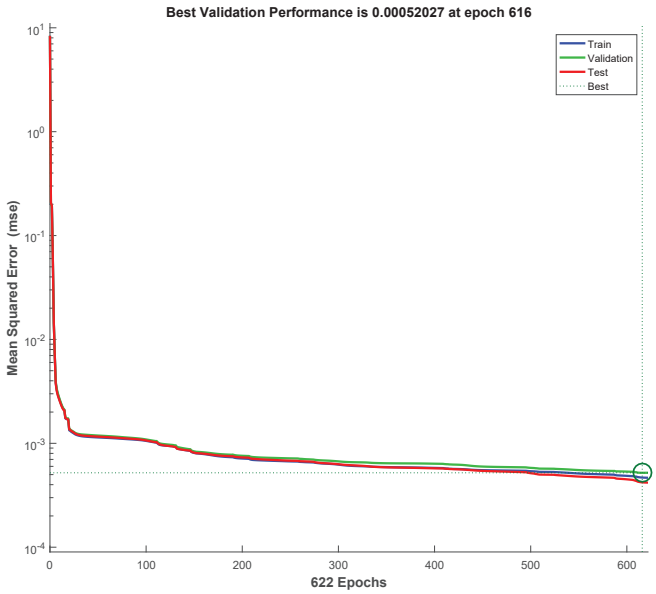

(a) Concentration

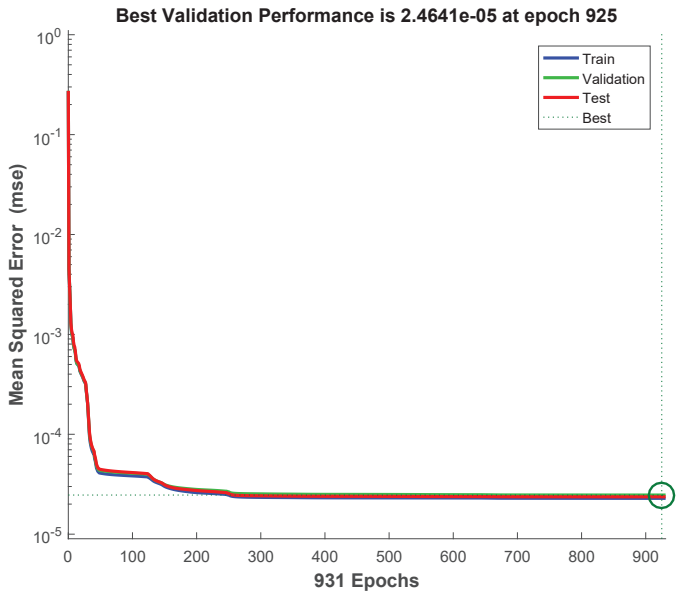

(b) Temperature

Figure 6.3: Mean Squared Error with increasing number of iterations for optimal profile of concentration and temperature NN training

If the Neural Network is trained perfectly to mimic the function for hydrodynamics, concentration and temperature, the NN model would produce exactly the same results as in the Finite Difference scheme. However, this is not the case and discrepancy between the FD simulation and NN model, as seen in Fig. 6.4 and Fig.6.5. In order to see the alignment of data, Fig.6.4 is a typical example of regression analysis of predicted concentration from NN compared with the

original concentration data from training, validation and test subset and overall performance. The dashed line is when there is a perfect match between the NN model and IBL model implementation where the concentration is exactly the same from both sources, and the coloured solid line is the fitting between the output and target. The performance of the fitting is very accurate, given that: 1). the solid fitting line is very close to the dashed diagonal line for perfect match 2). the correlation coefficient **R** is very close to one across all subsets of data.

After the training the NN is complete, this network is applied to predict the evolution of concentration and temperature up to the FD stopping time t_{mid} and even from t_{mid} onwards. This is particularly useful since the numerical solution FD takes much longer time in the time-stepping when forwarding in time, due to a source term present in the evolution equation of temperature in Eqn.(6.7) which is calculated in each time dt and space dr step in the finite difference scheme. Fig.6.5 demonstrate the evolution of concentration and temperature profile from FD implementation and the NN model, at four different times (t = 2,4,6,8). The concentration profile at different times is shown on the left panel and the temperature on the right. Since both concentration and temperature are associated with the flow hydrodynamics, they both are affected by propagation of dominant waves and subsequent smaller-amplitude waves in the FD implementation. This behaviour is presented in the NN model as well, where there is good agreement in smooth areas and some discrepancies in the smaller-amplitude region, induced by the non-linear behaviour of the system. Generally, NN modelling of temperature is more accurate than that of concentration, which can be found in the evolution profile in Fig. 6.5 and the level of MSE in Fig. 6.3. However, even for the concentration profile, the overall difference is small numerically , with $MSE = 10^{-4}$. As observed in Fig. 6.5, the differences in the concentration profile between the NN fitting and original IBL approach often lie in the peaks and troughs of the large-amplitude waves, as well as the accompanying smaller-amplitude waves, due to oscillation behaviour of the propagating waves and inter-wave mixing effects. These absolute differences are virtually impossible to avoid completely numerically, and the NN trained in this model is considered to reach a very good agreement with the original IBL results, based on the overall order of magnitude of the error.

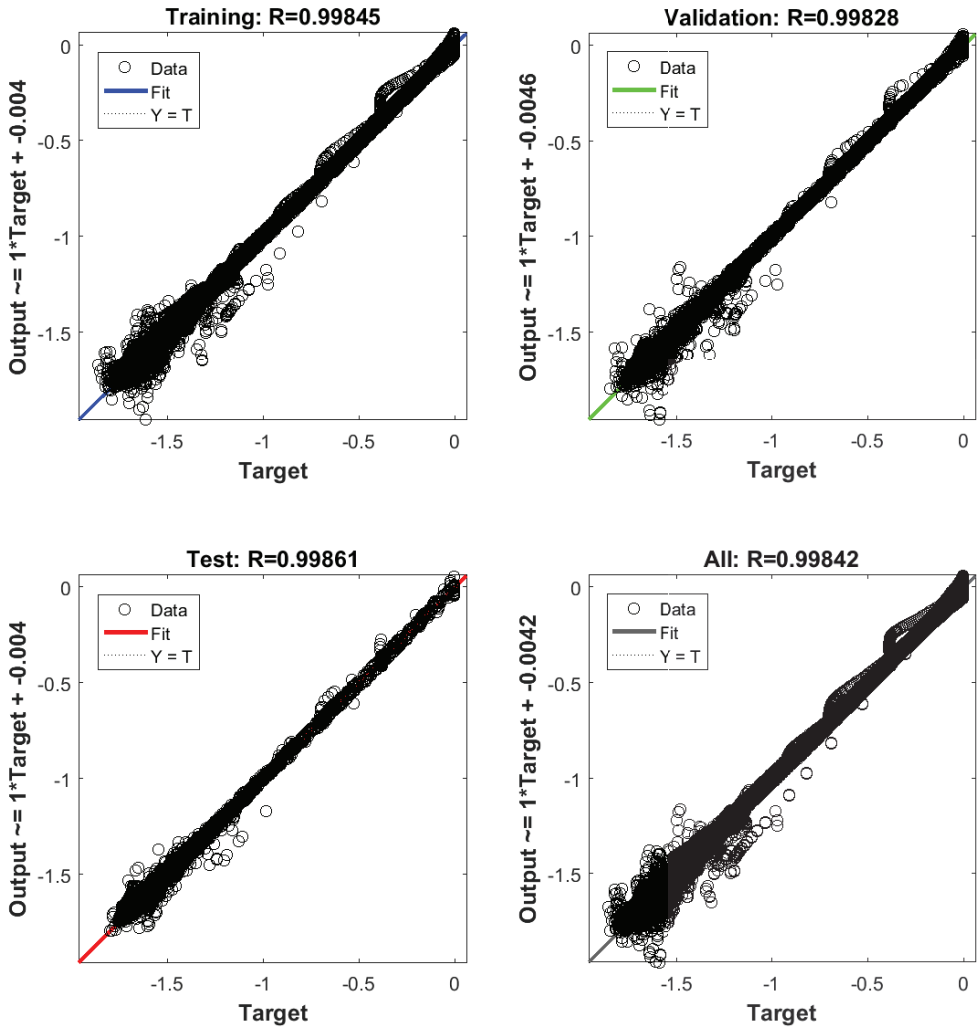

Figure 6.4: Regression for concentration NN training on training data, validation data, test data and overall data

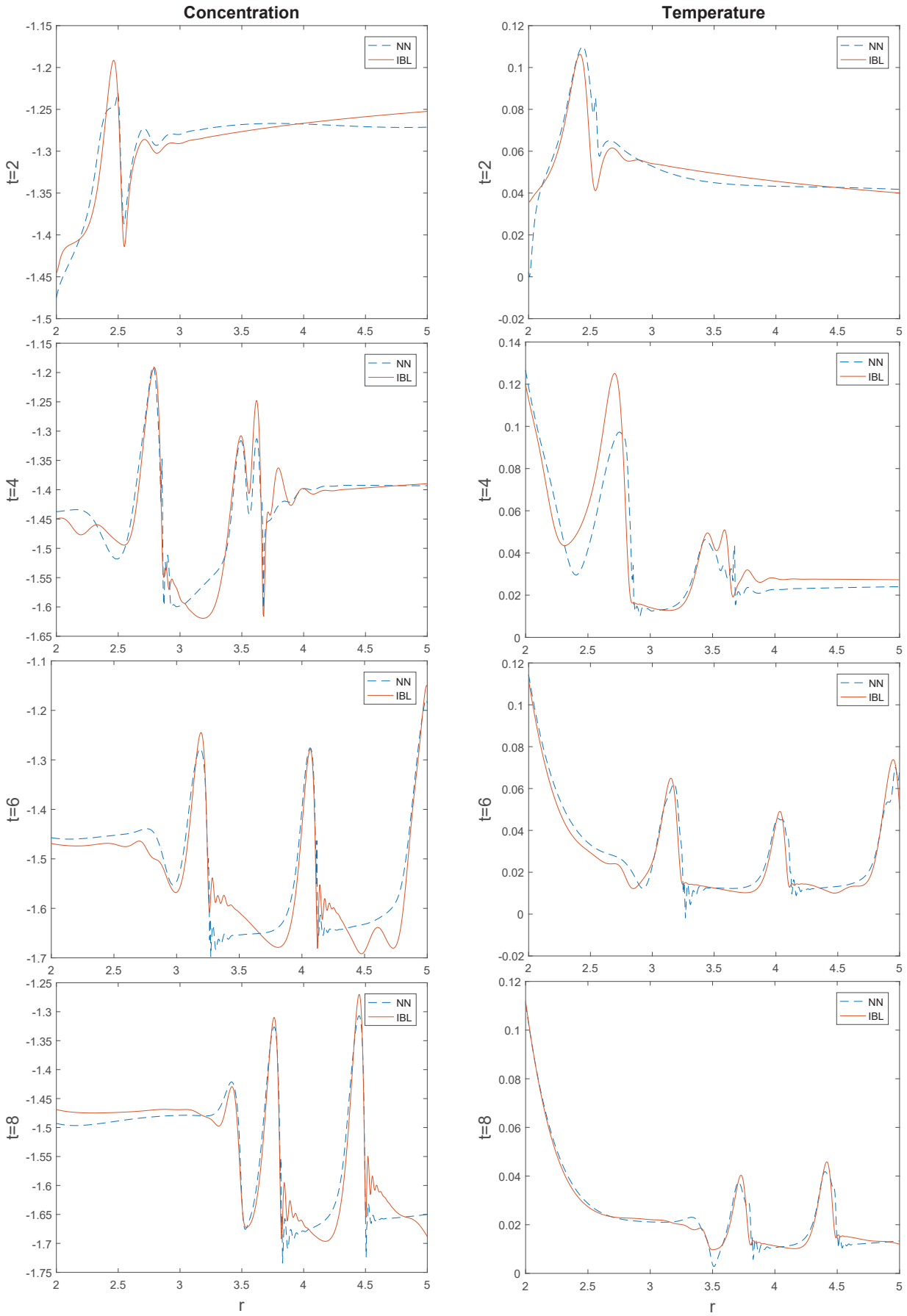

Figure 6.5: Comparison of NN regression and IBL implementation for concentration and temperature profile at different time units $t = 2, 4, 6, 8$

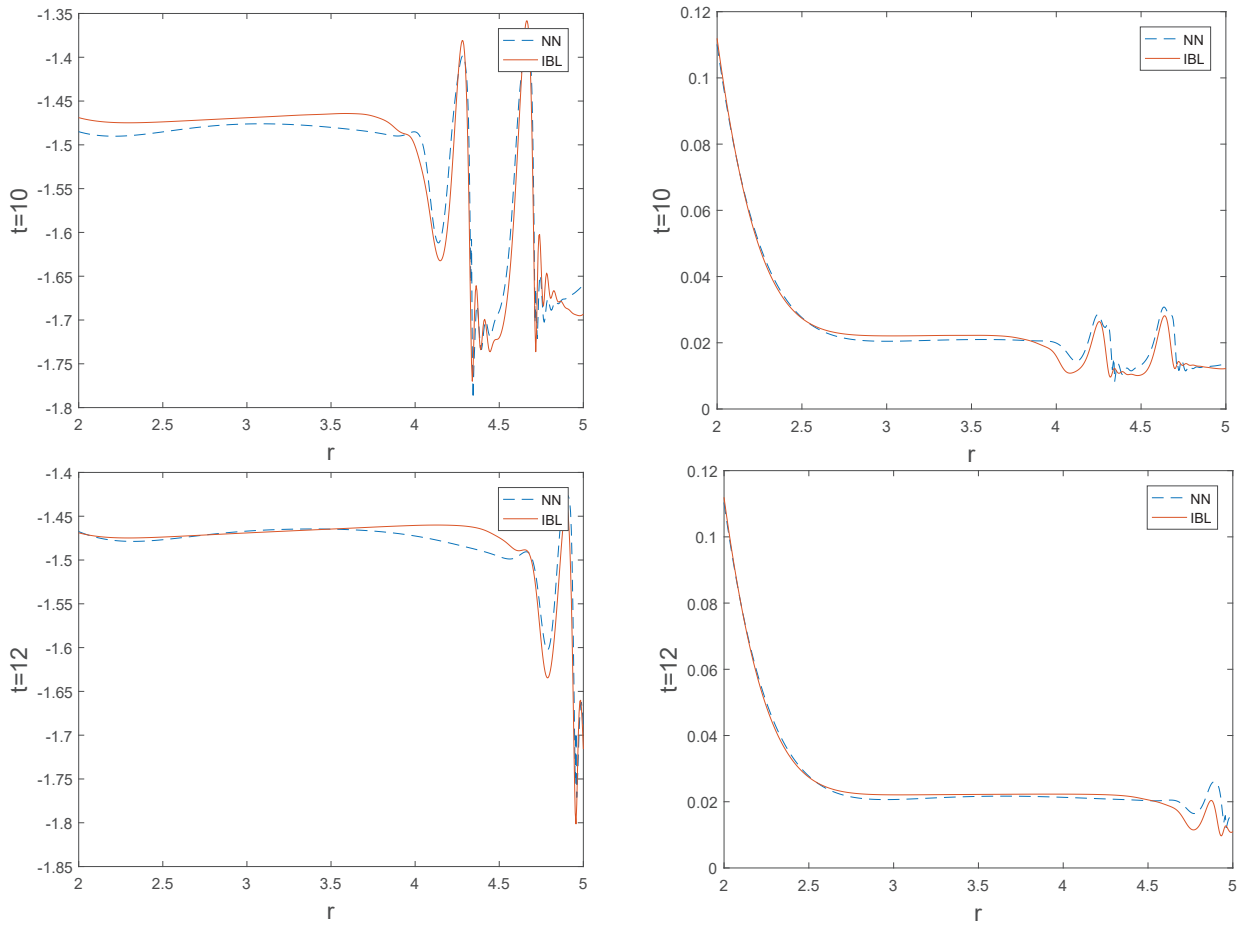

(a) Concentration

(b) Temperature

Figure 6.6: Prediction of concentration and temperature profile at t = 10,12 compared with the new FD implementation, with the same conditions ($\lambda = 0.01$, $r_{disk} = 7.5$)

As mentioned earlier in this chapter, one of the most important application of NN training i s to make predictions based on existing results. In this case, we stopped the FD scheme at $t_{mid} = 8$ in order to gather the training data for NN construction. After the NN is completed, we continue the FD scheme (or start a new instance under the same condition) and compare the NN predictions with FD scheme results after $t_{mid} = 8$ up to $t = 12$, in order to see if the function(network) has a general validity. Fig. 6.6 shows the prediction from NN compared with results from separate FD scheme under same operational conditions. We find good agreement between the NN model output and FD results in terms of both concentration and temperature profile, with smaller-amplitude waves generated at a very similar location following the dominant waves. The prediction result is particularly accurate for temperature, which is in line with a better fitting result for the temperature profile and lower level of error, due to more iterations

experienced.

In order to quantify the differences between the NN model and the conventional FD results, we apply one statistical measure called Root Mean Squared Error (RMSE) between the FD and NN results for both concentration (C_b) and temperature(Θ). It is an integral measure of the difference across the domain, versus time. More specifically, defined as:

$$RMS_b = \sqrt{\frac{1}{l}\int (C_{b_{NN}} - \hat{C_{b_{FD}}})^2 dr} \tag{6.8}$$

$$RMS_\Theta = \sqrt{\frac{1}{l}\int (\Theta_{NN} - \hat{\Theta}_{NN})^2 dr} \tag{6.9}$$

where b and Θ denote concentration and temperature respectively, consistent with previous chapter 5, and l is the length of radial direction r. A hat symbol on the b and Θ indicates the average value. As in Fig.6.7, the agreement of root mean square is reasonably good for both concentration and temperature, and the reason of narrow discrepancy is that only small-amplitude waves account for the differences between NN and FD implementation during the evolution of waves. Fig. 6.7 also shows that the rms is increasing with time in FD, and NN model reproduces this result reasonably well.

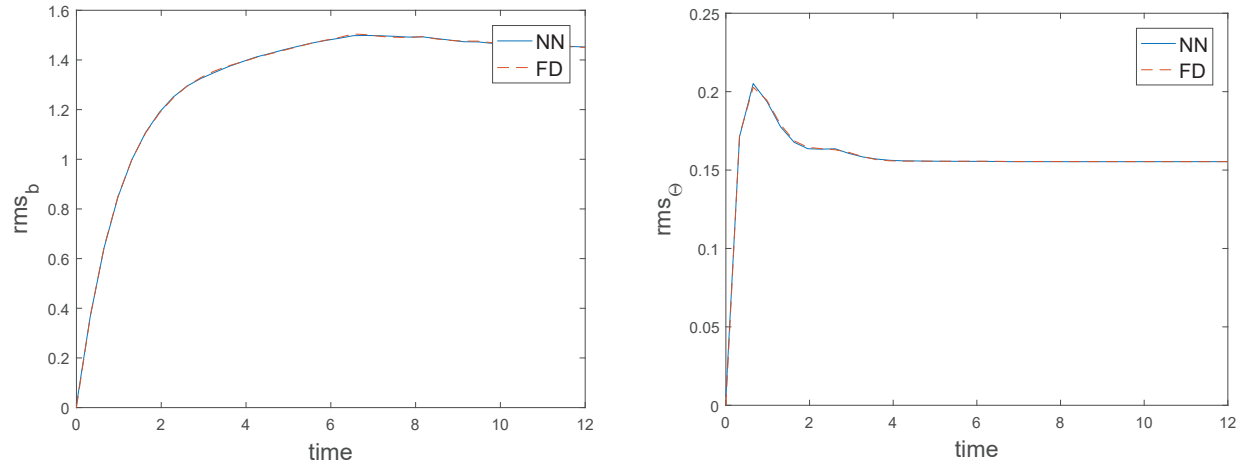

Figure 6.7: Comparison of radial velocity at a fixed point in time where $r = 3.5$, $\theta = \pi/16$ and $t = 12$

6.3 Neural Network Training - 3D Hydrodynamics

$$h_t + \frac{1}{r} f_r + \frac{1}{r^2} g_\theta = 0 \tag{6.10}$$

$$f_t + \frac{6}{5}\left(\frac{f^2}{rh}\right)_r - \frac{155}{126}\frac{g^2}{r^2 h} + f_\theta - \frac{3f}{2h} h_\theta + \frac{17}{14}\frac{1}{r}\left(\frac{fg}{h}\right)_\theta = \lambda^2 r h \kappa_r - \frac{3f}{h^2} + r^2 h + 2g \tag{6.11}$$

$$g_t + \frac{17}{14}\frac{1}{r}\left(\frac{fg}{h}\right)_r + g_\theta + \frac{25}{16}\frac{g}{h} h_\theta + \frac{155}{126}\frac{1}{r^2}\left(\frac{g^2}{h}\right)_\theta = \lambda^2 h \kappa_\theta - \frac{5}{2}\frac{g}{h^2} - 2f \tag{6.12}$$

The same logic can be applied when considering the three-dimensional hydrodynamics for the film flow, considering that film thickness and flow rates are a function of spatial location r,θ and time t. These solutions are impossible to solve analytically and time-consuming to solve numerically, thus NN method is a reasonable approach towards the traditional problem-solving.

In order to gather the training data for this analysis, we firstly run a FD simulation with the same inputs and operation conditions $\lambda = 0.05$ and $r_{disk} = 10$. With the stopping time being $t = 8$, we choose a time interval that there are totally 150 points in time, also the interval in radial and azimuthal direction is chosen such that there are 1500 points in r and 100 points in θ. Thus, the total sample number of sample points is 150*100*1500 = 22,500,000 sample points, each containing the information of hydrodynamics and flow rates.In order for NN training to work, we split the whole dataset into three subsets: 60% (12,500,000) of training , 30% (6,750,000) of validation and 10% (2,250,000) of testing sets, which is consistent with the previous case for chemical reactions.

To examine the performance of this nonlinear fitting, Fig. 6.2 shows the distribution of the error (Target- Output) for both the three dimensional hydrodynamics. The training, validation and testing data are labelled blue, green and red respectively, same as the previous case. The vertical yellow line in the centre indicates zero error. The NN training has given good results from the fact that the level of error (x axis) is very small and the most of errors centred around

zero. This is particularly true for training dataset, but the error distribution for validation and testing samples are also in agreement with that of the training data, with very few large errors far away from the centre. Figure 6.3 demonstrates the Mean Squared Error (MSE) with number of iterations(epochs). The MSE for film thickness drops sharply with initial 200 iterations and slowly reaches convergence in the end.

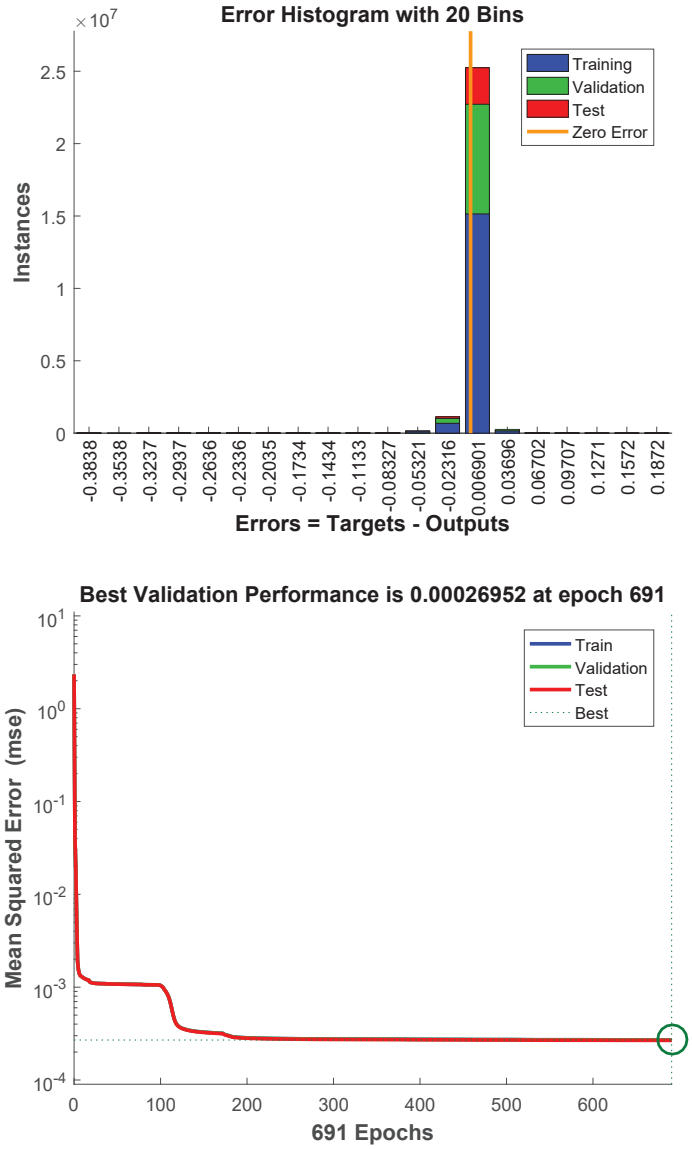

Figure 6.8: Final error distribution and Mean Squared Error evolution of three dimensional film thickness with increasing number of iterations(epochs)

The regression analysis is very similar to the NN model for chemical reactions and is shown in the Appendix D.1, where the regression shows that the NN model output has a very high correlation coefficient with the perfect diagonal line. After the training the NN is complete, we

apply this trained network to simulate the evolution of three-dimensional hydrodynamics up to the FD stopping time t_{mid} and from t_{mid} onwards for prediction, in order to bypassing the large amount of time for FD scheme implementation for multidimensional . Fig.6.9 demonstrates the evolution of the three-dimensional film thickness h from NN in comparison with result from original FD on the left panel; The evolution of film thickness from NN model has a good fit towards the original FD outcome in terms of the propagation of large-amplitude waves from disk centre to disk periphery, the following smaller-amplitude waves look similar but not visible from the three-dimensional h plot and these waves are the cause of discrepancy between the two model results. In order to further clarify the difference between the NN and FD model, we also present the difference between those two film thickness results $\Delta h = h_{FD} - h_{NN}$ on the right panel in the same figure. The difference Δh is sufficiently small compared with the h itself, showing that the NN model produces a reasonably accurate fitting and that the Δh is induced by the smaller-amplitude waves due to the higher-order derivatives terms in the original system of PDEs.

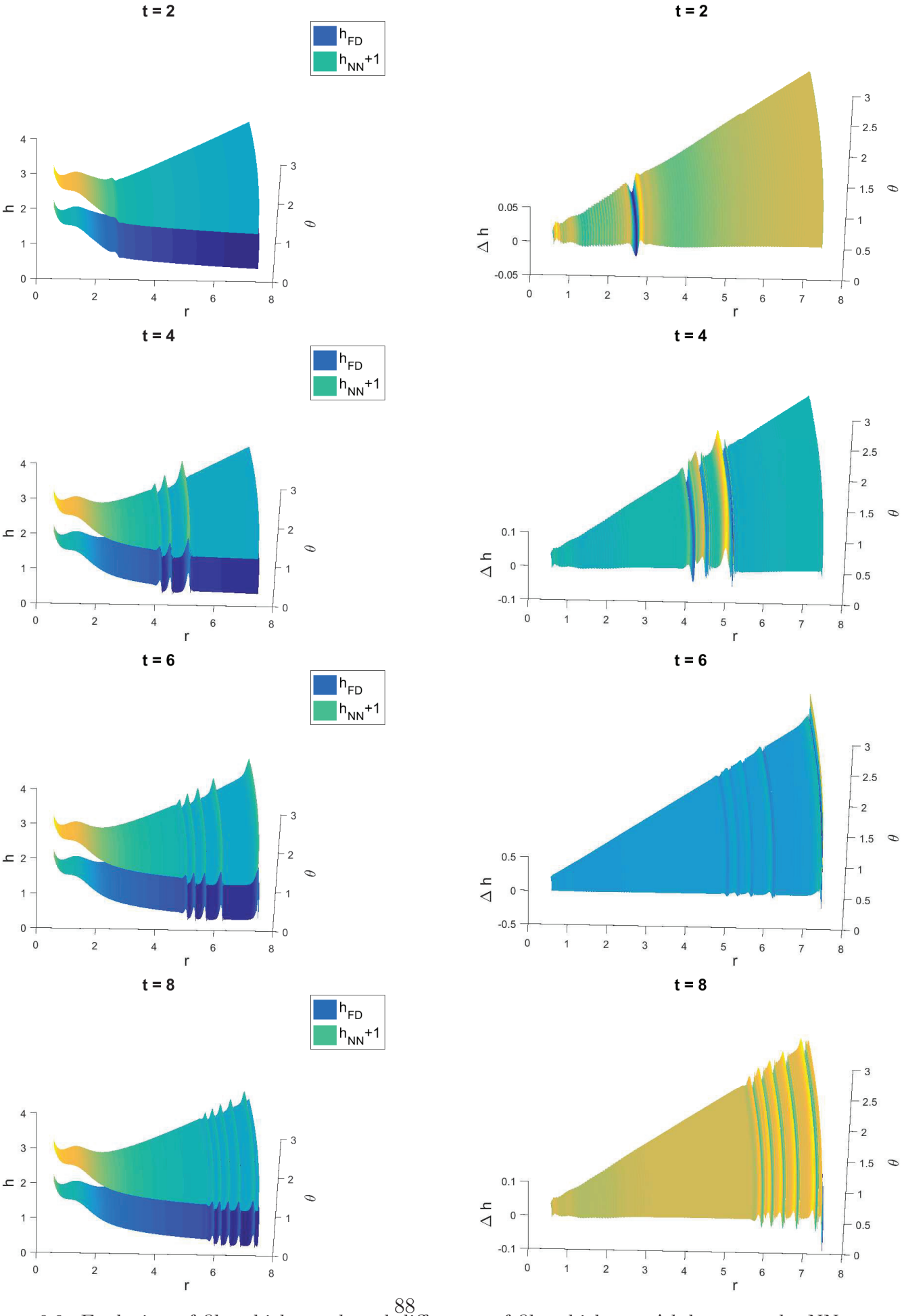

Figure 6.9: Evolution of film thickness h and difference of film thickness Δh between the NN model and original FD results, at time $t = 2, 4, 6, 8$

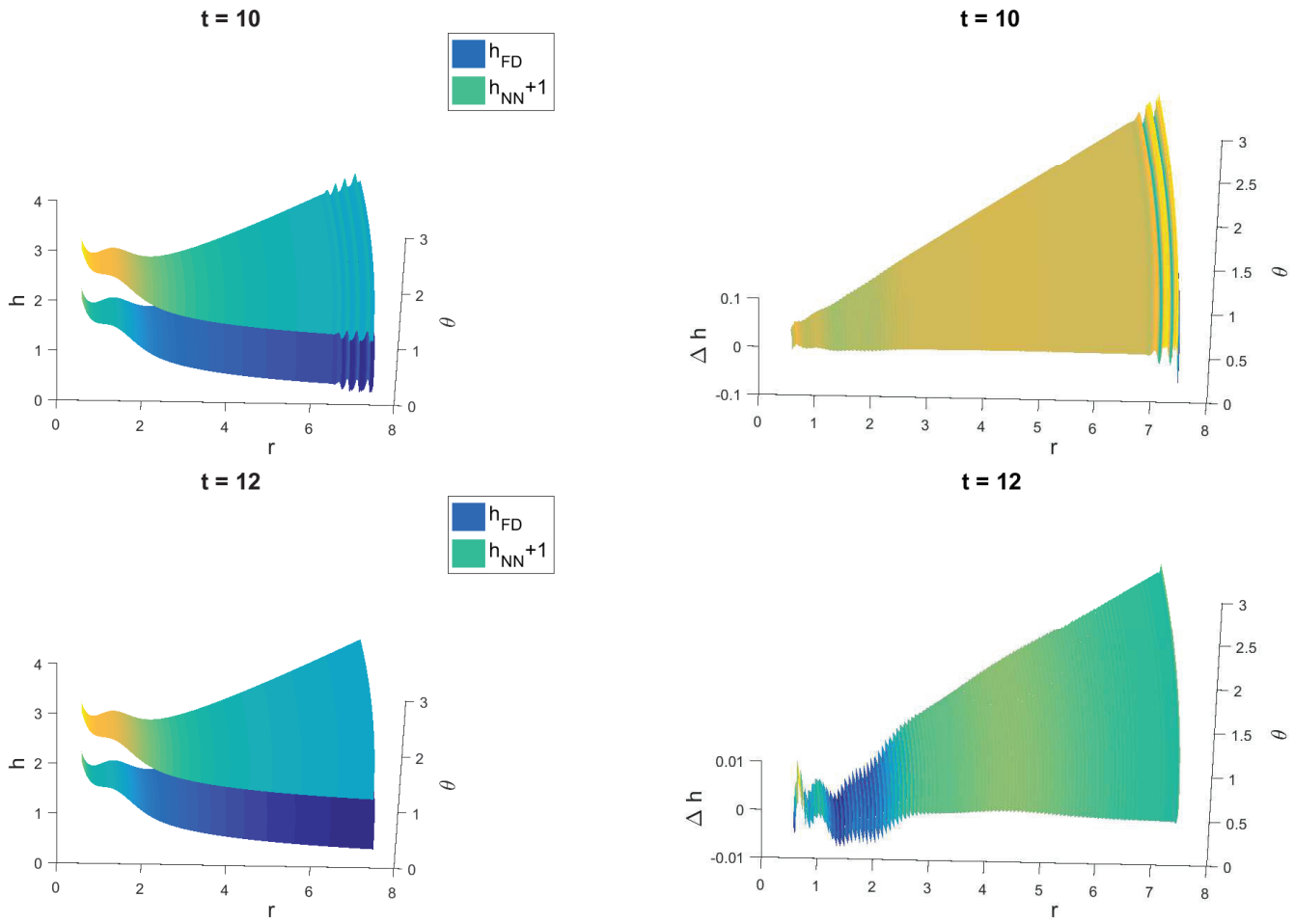

Figure 6.10: Prediction of film thickness h using NN compared with FD(left),and difference of film thickness Δh between the NN model and original FD results, at time $t = 10, 12$

Also, we include the prediction of three-dimensional film thickness in future time, compared with a new FD simulation under the same condition in Fig. 6.10. At the late stage of propagation $t = 10, 12$ the waves are mostly approaching disk periphery before returning to the waveless steady-state, so is the difference Δh. It shows that the trained NN produces a very accurate prediction of three-dimensional hydrodynamics at future times based on the information up to a certain time.

In order to further validate the accuracy of the NN model, we test it with radial velocity profile u extracted from both FD and NN model. As in Fig. 6.11, the radial velocity at $r = 3.5$, $\theta = \pi/16$ and $t = 4$ from both sources exhibit a parabolic profile in the vertical direction, which is in line with the formulation section where the radial and azimuthal velocities are assumed parabolic.

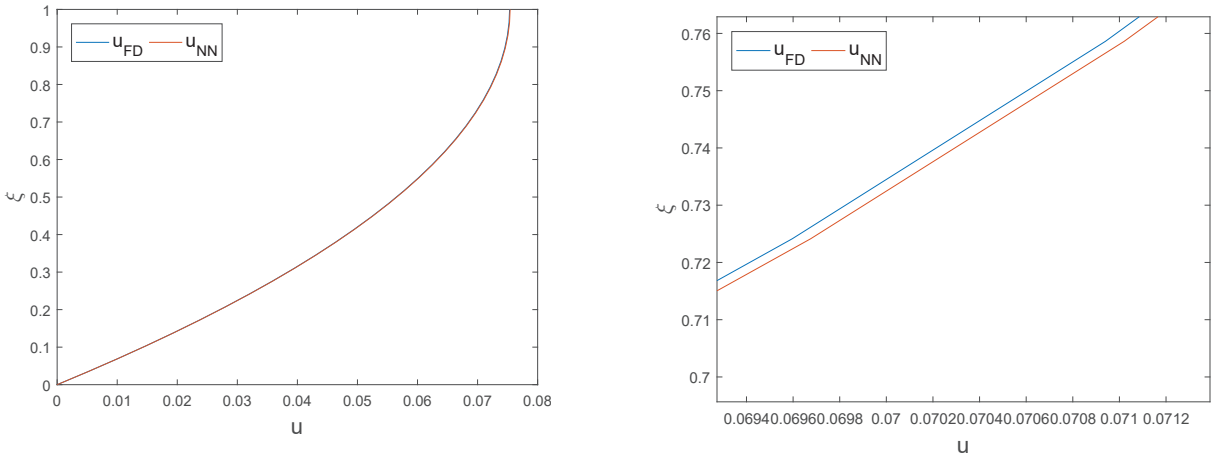

Figure 6.11: Comparison of radial velocity at a fixed point in time where $r = 3.5$, $\theta = \pi/16$ and $t = 12$

6.4 Conclusion

Following the discussion of three-dimensional hydrodynamics and presence of first-order chemical reaction associated with the flow over spinning disks. However, the computation of finite difference scheme for both cases consumes a substantial amount of time, even after local code parallelisation with operator splitting method, due to additional dimensional involved and the presence of the integral term which needs to be calculated in every time and space step. Neural network is a modern technique to associate the implicit function(relationships) between the inputs and targets, and is fit for the purpose of computational simplification and efficiency in our model as it builds a smart network which can learn from previous existing FD results and produce optimal fitting and prediction results via consistently updating the weights and bias linking the inputs and outputs.

This chapter demonstrate the accuracy and general validity of NN training for both concentration and temperature profile, leading to a significantly reduction in time for simulation: mins to hours compared with hours to days in typical FD scheme implementation, while maintaining highly accurate results very close to original FD simulation. The Mean Square Error can be reduced to the order of 10^{-4}-10^{-5} after optimal number of iterations achieved. The NN model also predicts the evolution of wave and associated concentration and temperature pro-

file in future time accurately, so it can potentially replace the relatively time-consuming FD implementation (especially in multidimensional scenario).

Chapter 7

Conclusions

7.1 Conclusions

This dissertation focuses on the low-order modelling of the dynamics of thin liquid film over spinning disks, including:

- Derivation of three-dimensional IBL model for non-axisymmetric condition and system of PDEs in presence of chemical reactions
- CFD Simulation for full Navier-Stokes
- Comparison of film thickness and velocity profile underneath the films with CFD and experimental results for cross validation
- ANN model based on the FD implementation for computational simplicity

The derivation of the evolution equations for such flows in this geometry is in Chapter 3, including the hydrodynamics and chemical reactions. This was done by a combination of application of long-wave theory to the original Navier-Stokes equations and Integral Boundary Layer approach where the velocities are integrated in axial direction, taking into account of suitable boundary conditions.

In Chapter 4, we delve into the three-dimensional waves, dropping the axisymmetric assumptions that the majority of literature makes. It can be seen from the model that the whole structure of waves over the disk can be observed from the solutions of the system of PDEs. Also the non-axisymmetric model gives us a better insight into the flow of the film, including the flow regimes corresponding operation conditions and fluid property (λ,r_{disk}). These flow regimes and film thickness/velocity are then directly compared with CFD full simulation and experimental observations, which show good agreement. Due to the full wave structure observed in the three-dimensional evolution equations, the intensification of mass and heat transfer associated with the flow can be quantified using interfacial waviness W, which increases during the transition from smooth film and concentric waves to spiral wave structure.

In Chapter 5, the focus is thin liquid film dynamics over spinning disk, with the presence of first-order chemical reaction. The most obvious change introduced by chemical reaction is the additional dependent variables,i.e.concentration and temperature which are affected by the hydrodynamics. While this area of research is significant, few researchers have included the reaction in the flow dynamics. Compared with Stein group [12], in the thesis the source term in the diffusion-convection equations in considered, which is numerically integral of both temperature and concentration profile. We presented the parametrisation following the solution of PDE, with dimensionless numbers Sc, Pe and Da representing diffusion and chemical reaction. These dimensionless numbers are then discussed in detail regarding the effect on the flow evolution and corresponding heat/mass transfer:

- Higher Da means higher reaction rate, leading to the faster consumption of the reactant and release of heat correspondingly, i.e. faster reduction in concentration profile C_b and overall higher temperature Θ.
- Higher Sc leads to the decrease in the magnitude of concentration, but it has limited impact on temperature
- High Pe results in the decrease in the temperature profile, but it has limit impact on concentration profile

Numerical measure of average Sherwood and Nusselt number was introduced in order to quantify the wave-induced intensification in mass/heat transfer. Comparison between steady-state solution and time-dependent transient solution proves the increase in Sherwood and Nusselt due to the mixing effect of the waves, and also this intensification is further strengthened by the decrease in λ, which is the combination of inertial and surface tension.

Chapter 6 was proposed based on the fact that traditional FD implementation of lower-order model consumes large amount of computational time (even though it is already an improvement compared with DNS). We apply the modern NN training in this model based on existing FD results in order to predict the evolution of hydrodynamic, concentration and temperature in future time without running the relatively time-consuming FD scheme. By comparison with existing FD scheme up to its stopping time and new FD in future time, it is shown that NN model produces results in good agreement with the original FD implementation, both in uni-dimensional and multidimensional scenarios.

7.2 Limitations and Future Work

The main limitation is the numerical solution of three-dimensional evolution equations, as λ decreases, the waves become more unstable, which artificially creates numerical instability in the code. This directly reduces value of λ (0.01 and above) where the numerical results can be obtained, translating to the reduction in the range of operational conditions (the rotational speed can only reach 600 rpm with $\lambda = 0.01$).

There are naturally many possible extensions to this low-order model, both in the theoretical model development and implementation of numerical solutions.

From the theoretical viewpoint, the low-order model can be extended to cover non-Newtonian fluids, with the pursuit of one single parameter characterising the fluid property and inclusion of this parameter into the original PDEs. In addition, other considerations can be taken in terms of extension.

From the implementation viewpoint, efficient algorithms need to be discovered in order to solve the system of PDEs with multi-dimensional independent variables (Initial Value Problem) , including the source term induced by chemical reactions which needs to be calculated at every grid point in space time, significantly increasing the computation time. Neural Network is a sensible approach, but it need the original training data feed from FD. Also, under very low level of λ, the FD scheme is very unstable and a more robust algorithm/code implementation can be done in the future.

Appendices

Appendix A

CFD Simulation

A.1 Setup

The CFD simulation of the dynamics of thin film flow over a spinning disk is conducted using a uniform mesh size of 30 micron on a rotating reference frame, as shown in Fig. A.1. A no-slip wall boundary condition was imposed on the rotating disk surface with a constant angular velocity.

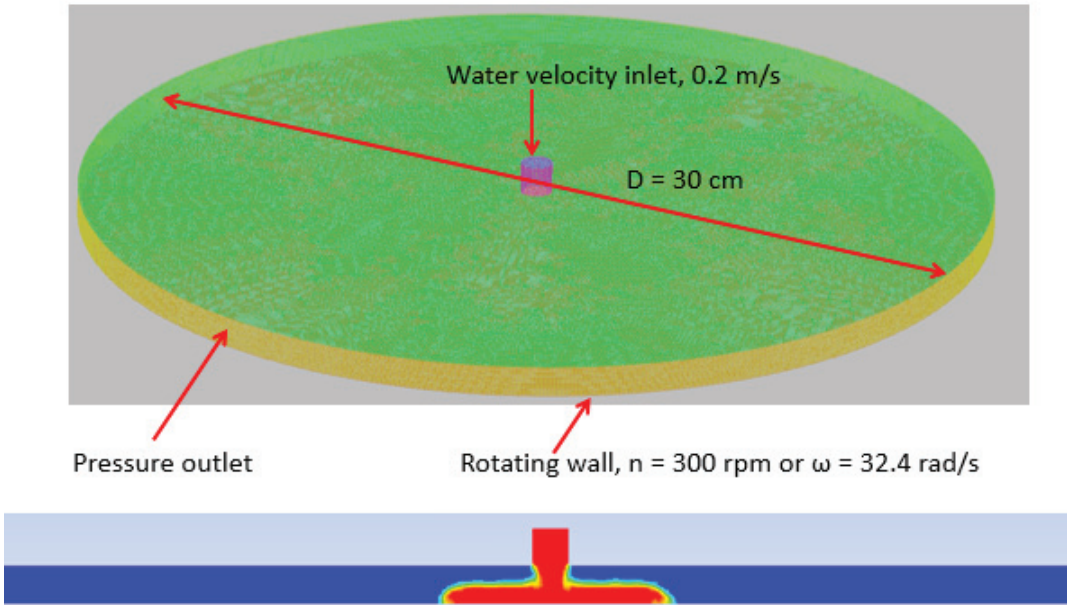

Figure A.1: CFD Geometry of Thin Liquid Film over Spinning Disks

A.2 CFD Results

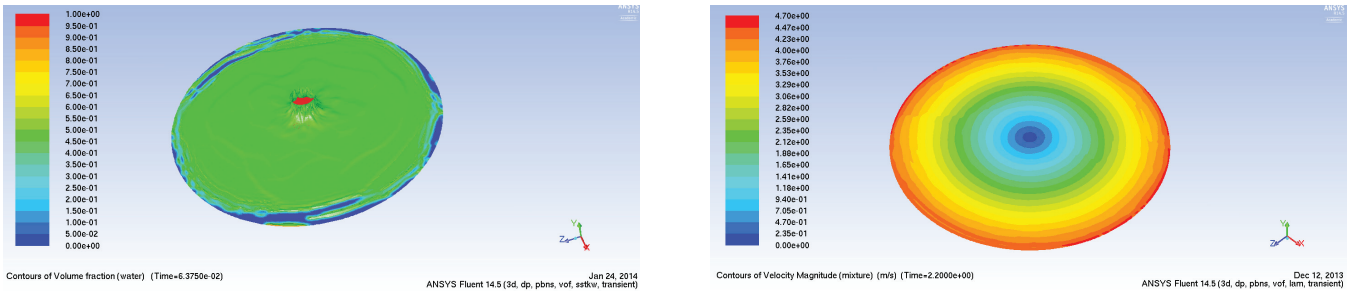

Figure A.2: Flow regime and wave structure in CFD simulation, with $Q_c = 13ml/s$ and $\Omega = 100rpm$

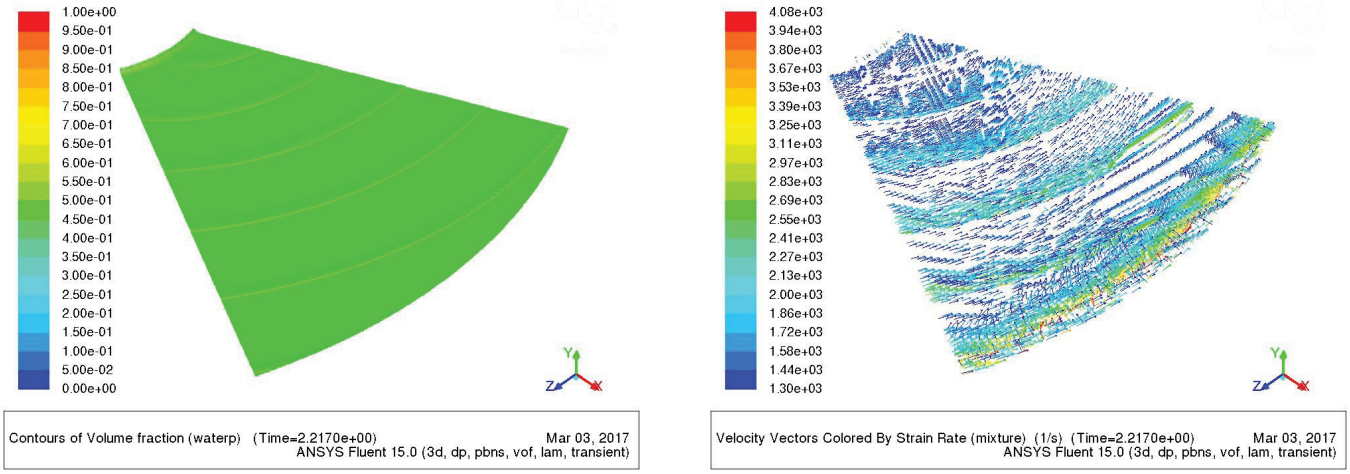

Figure A.3: Irregular and spiral waves and their respective velocity and stress from CFD simulation

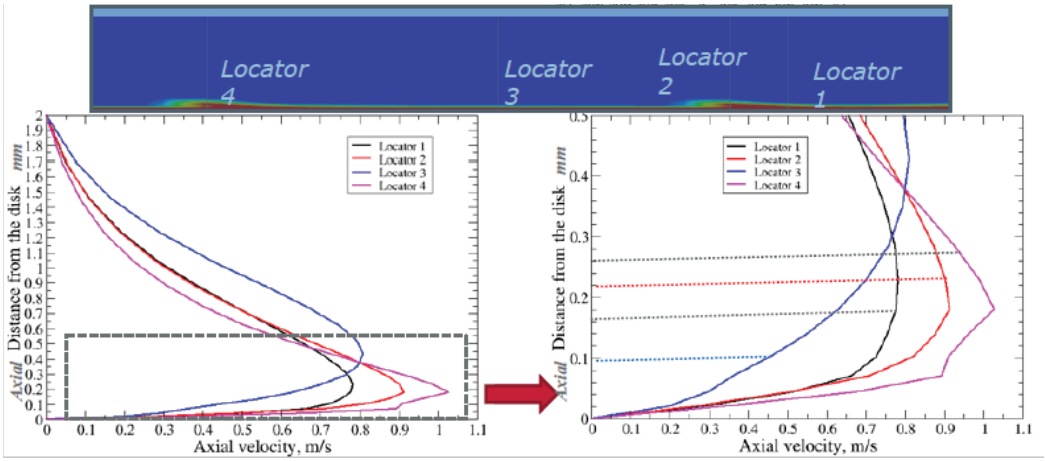

Figure A.4: Axial velocity underneath the film across radial direction when $Q_c = 13ml/s$ and $\Omega = 100rpm$

The CFD simulation also investigate:

1. Flow regime and structure over the entire disk

2. Wave patterns and velocity/stress

3. Axial velocity profile underneath the films across the location.

Appendix B

Convergence Test

The convergence test has been performed, in order to determine the optimal grid points required to solve the set of partial differential equations Eqn. (5.1) - (5.5) using finite difference scheme. The final number grid points used is 1500, given the time consumed and achievement of the fine mesh. As shown in Fig. B.1 - B.2, further increasing the number grid points beyond 1500 does not have significant impact on the solutions to the equations.

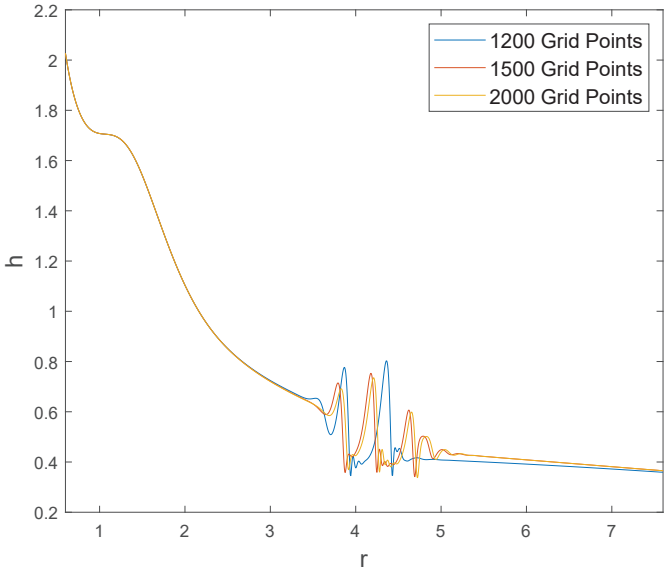

Figure B.1: Profile of film thickness h, with number of grid points from 1200 to 2000, where $\lambda = 0.01$, $r_{disk} = 7.5$

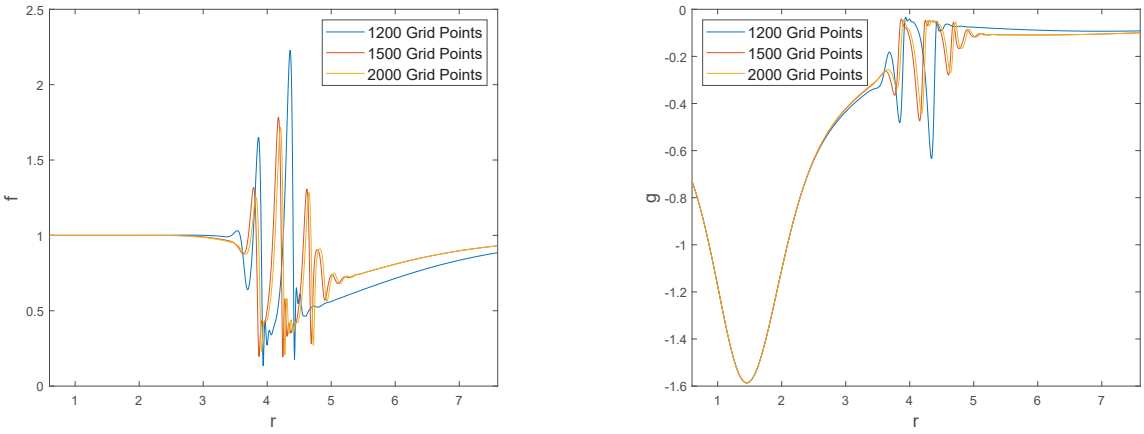

(a) (b)

Figure B.2: Profile of flow rates f (a) and g (b), with varying number of grid points from 1200 to 2000, under the same condition as in Fig.B.1

Appendix C

Average Nusselt Number

The derivation of average Nusselt number Nu_{avg} is shown in this section, with the tildes indicating dimensional variables. The local heat flux $\tilde{q}$ is represented by the equation:

$$\tilde{q} = -\lambda_L(T1 - \bar{T}) \tag{C.1}$$

Similar to mass transfer coefficients, λ_L is the local heat transfer coefficient, $T1$ is the temperature of the solute at equilibrium and $\bar{T}$ is the local average temperature of solute in the liquid film. Within the present model, the heat flux is also characterised by:

$$\tilde{q} = -k\left(\frac{\partial \tilde{T}}{\partial \tilde{z}}\right)_{\tilde{z}=0} \tag{C.2}$$

where k is local thermal conductivity, leading to:

$$\lambda_L = \frac{-k}{T1 - \bar{\bar{T}}}\left(\frac{\partial \tilde{T}}{\partial \tilde{z}}\right)_{\tilde{z}=0} \tag{C.3}$$

The average heat transfer coefficient over the whole disk can be represented by dimensionless Nusselt number Nu_{avg}:

$$Nu_{avg} = \frac{\lambda_{avg} H_0}{k} = \frac{H_0}{(T1 - \bar{T})\pi\tilde{r}^2} \int_0^{\tilde{r}} \left(\frac{\partial \tilde{T}}{\partial \tilde{z}}\right)_{\tilde{z}=0} 2\pi\tilde{s}d\tilde{s} = \frac{2}{r^2}\left[Nu_{in} + \int_{r_{in}}^{r} \left(\frac{\partial \Theta}{\partial z}\right)_{z=0} sds\right] \tag{C.4}$$

Appendix D

Neural Network

D.1 NN Training Regression Analysis

The regression analysis has been performed in the training, as part of the feed-forward NN structure. Fig. D.1 and D.2 show the NN regression analysis of all partitions of data, for temperature Θ and film thickness h from IBL solutions respectively.

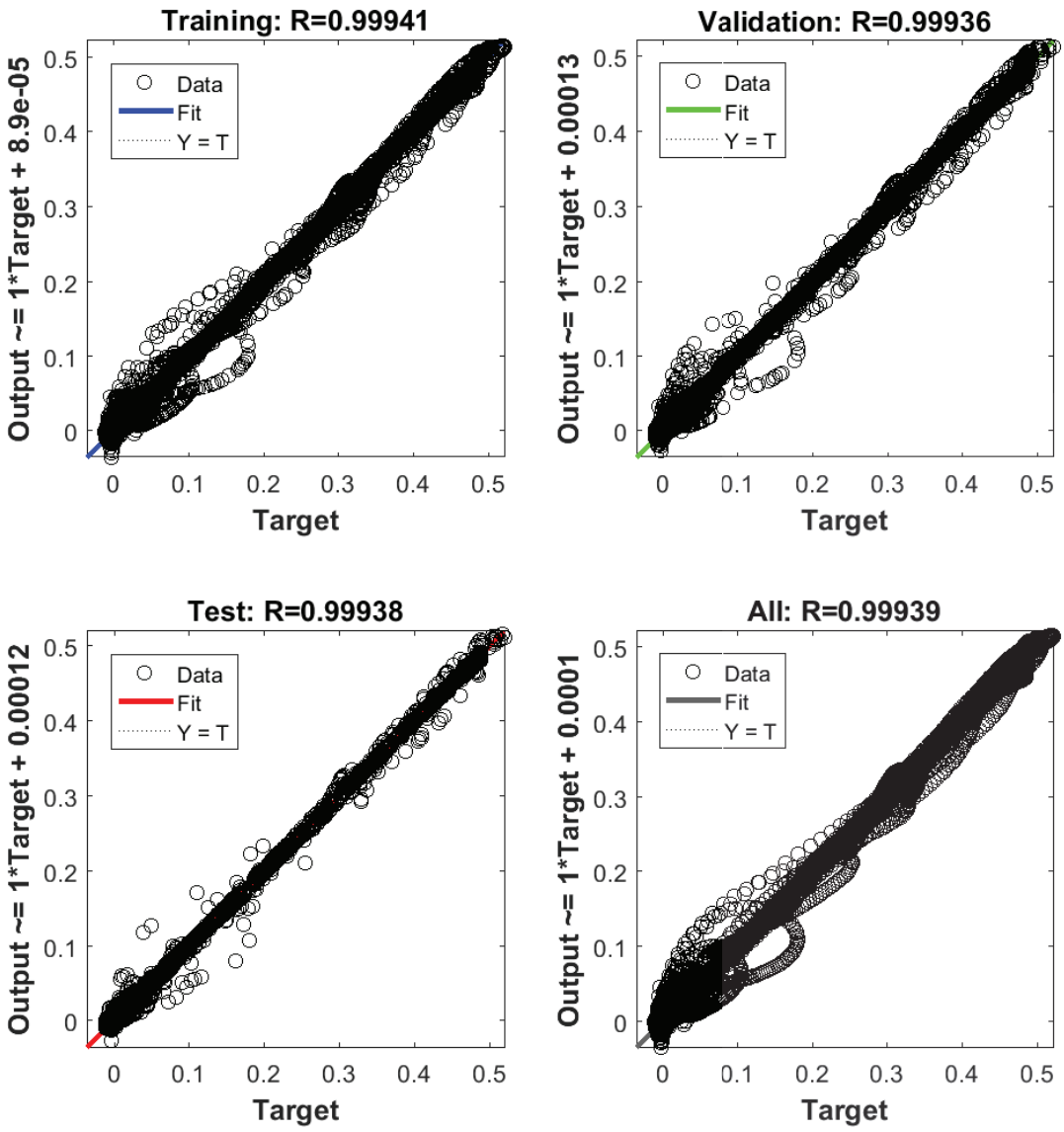

Figure D.1: Regression for temperature NN training on training data, validation data, test data and overall data

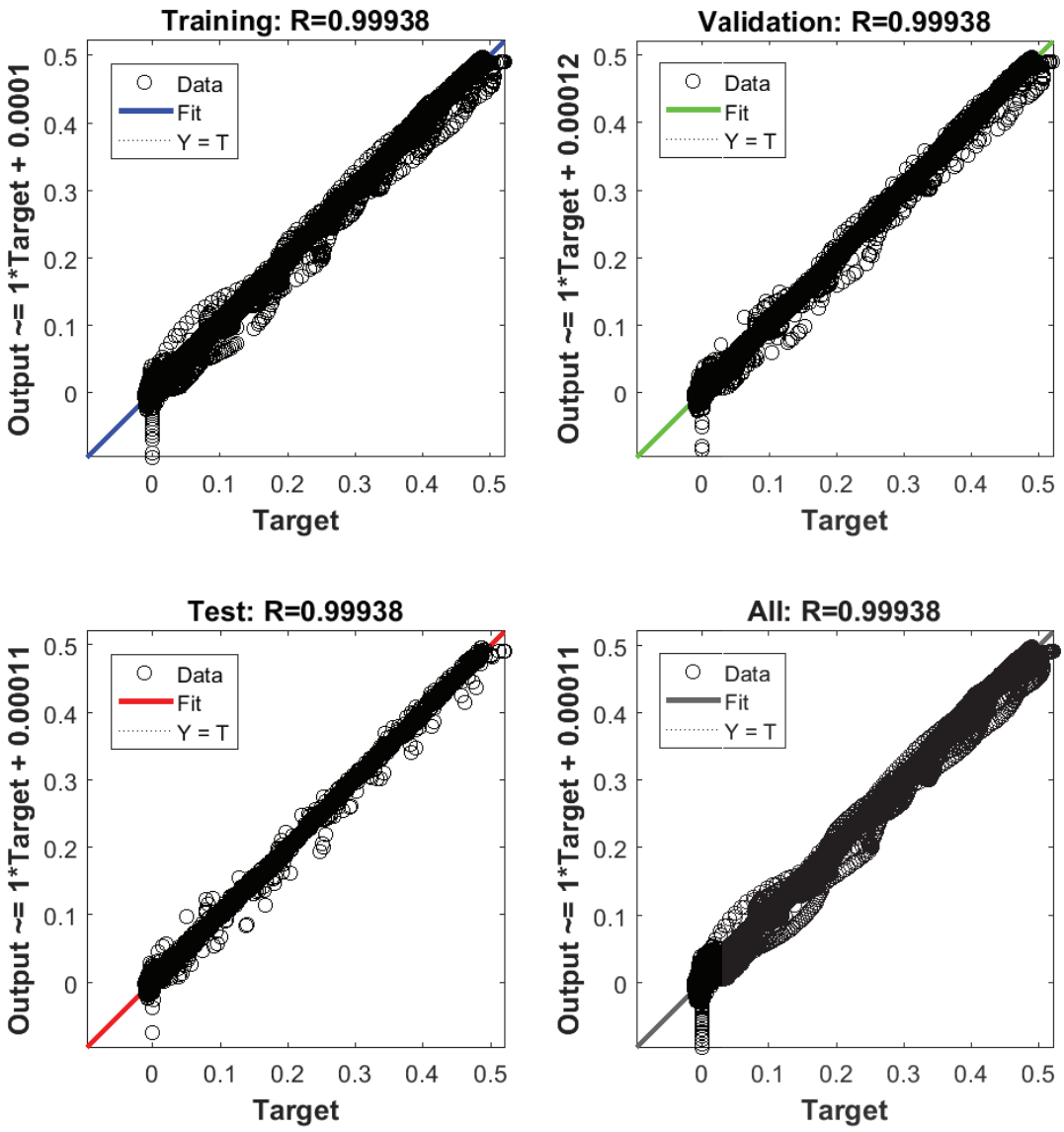

Figure D.2: Regression for three-dimensional film thickness NN training on training data, validation data, test data and overall data

D.2 NN Performance in Matlab Toolbox

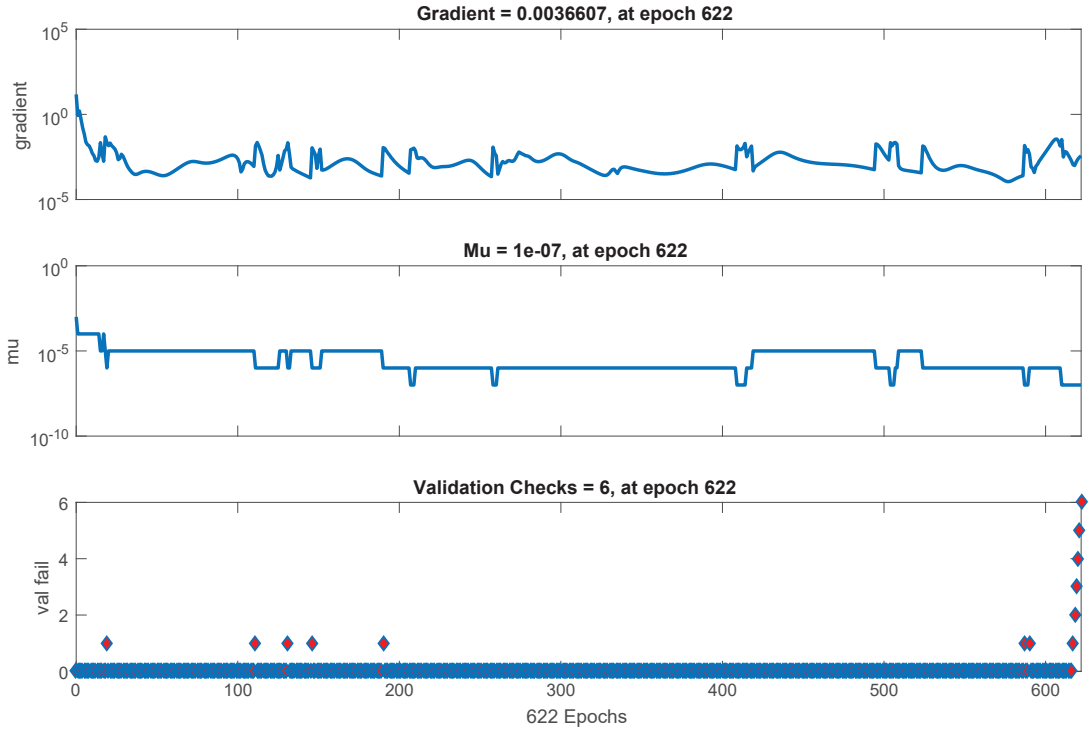

Figure D.3: Training State of NN model in terms of concentration

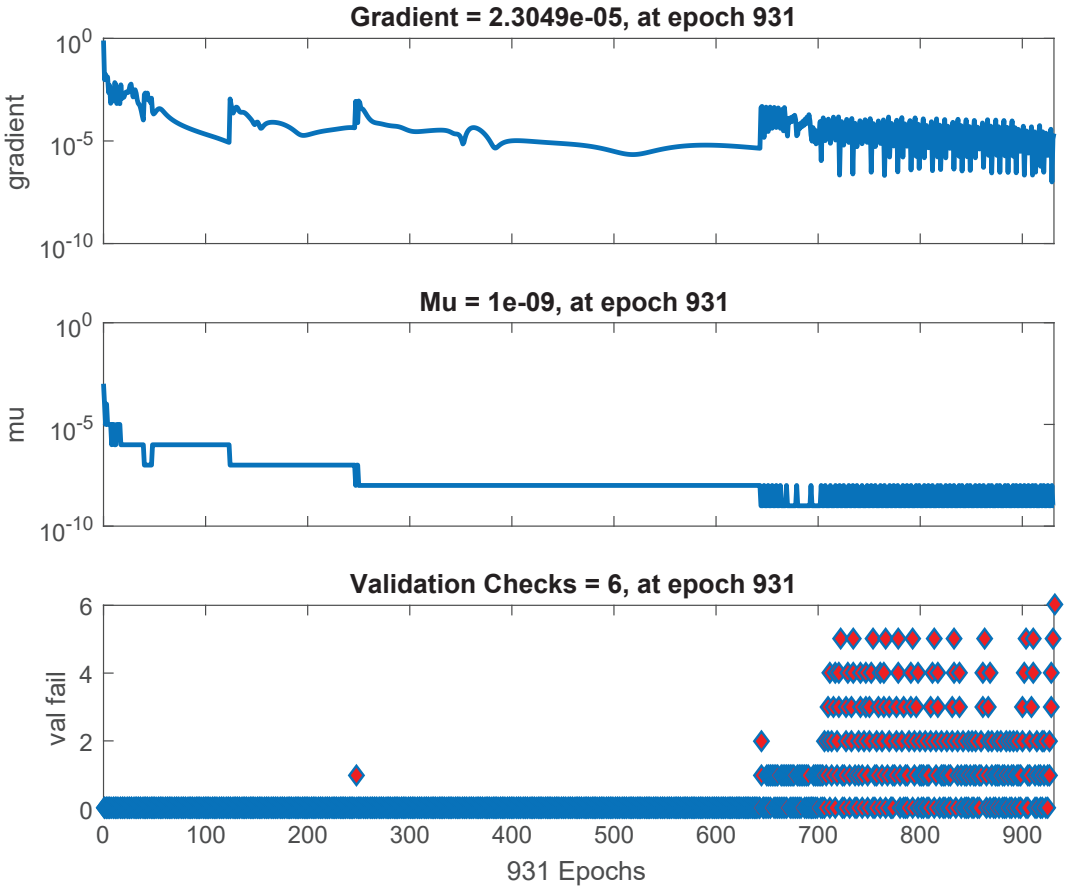

Figure D.4: Training State of NN model in terms of temperature

Appendix E

Matlab Code

E.1 Finite Difference Runge-Kutta 3

```
%solve hydrodynamic eqns(system of PDEs)with finite difference
    method
clear; clc; close all
%rin=0.1; rdisk = 1; T=2; M =500; N=200000;
rin=0.2;
rdisk = 1;
T =1.7;
M =500; %1000
N =80000; %200000
dr = (rdisk-rin)/M;
r = linspace(rin,rdisk,M+1);
dt = T/N;
t = linspace(0,T,N+1);
E=10;
We=1e8;
Sc=556;
```

```
16
17 hin=3.^(1/3)*rin.^(-2/3);
18 %initial condition h = 3^(1/3).*r.^(-2/3);f=1;g=0
19 h = 3.^(1/3)*r.^(-2/3);
20 f = r*0 + 1;
21 g = r*0;
22 B = r*0;
23 Nplot=100;
24 FF=zeros(N/Nplot,M+1);
25 GG=zeros(N/Nplot,M+1);
26 HH=zeros(N/Nplot,M+1);
27 BB=zeros(N/Nplot,M+1);
28
29 NRK=3;
30 % iteration of time
31 for  jTime = 1:N
32
33     h_old = h;
34     f_old = f;
35     g_old = g;
36     B_old = B;
37     for iRK=1:NRK
38         h(1) = hin+2*rand;
39         f(1) = 1 ;
40         g(1) = 0 ;
41         B(1) = 0 ;
42         f(M)=f(M-1);
43         f(M+1)=f(M);
44         g(M)=g(M-1);
```

```
45          g(M+1)=g(M);
46          B(M+1)=B(M);
47
48          h(M)=h(M-1);
49          h(M+1)=h(M);
50
51          for i= 2:M-1
52              h(i) = h(i)- (dt/dr)*(f(i)-f(i-1))-dt*(f(i)/r(i));
53
54              f(i) = f(i)-(dt/(h(i)*r(i)))*(18*f(i)^2/5-155*g(i)
                    ^2/126)...
55                  -6*dt*r(i)^2/(5*dr).*(f(i)^2/(h(i)*r(i)^2)-f(i-1)
                        ^2/(h(i-1)*r(i-1)^2))...
56                  +2*E*dt*g(i)+E^2*dt*(r(i)*h(i)+1.0/We*h(i)*((h(i+2)
                        -3*h(i+1)+3*h(i)-h(i-1))/(dr^3)...
57                  +1/r(i)*(h(i+1)-2*h(i)+h(i-1))/(dr^2)-1/r(i)^2.*(h(i
                        )-h(i-1))/dr)-3*f(i)/h(i)^2);
58
59              g(i) = g(i)-34*dt/7.*(f(i)*g(i)/(h(i)*r(i)))-2*E*dt*f(i)
                    ...
60                  -(17/14)*(dt/dr)*(r(i).^2)*(f(i)*g(i)/(h(i)*r(i).^2)
                        -f(i-1)*g(i-1)/(h(i-1)*r(i-1).^2))...
61                  -5/2*E^2*dt*g(i)/(h(i)^2);
62
63              B(i) = B(i)-(3*f(i)*dt)/(2*h(i)*r(i)*dr)*(1-3*B(i)^2/10)
                    *(B(i)-B(i-1))...
64              +6*dt/(Sc*B(i)*h(i)^2)-(B(i)*dt)/(2*dr*h(i)*r(i))*(1-3*B
                    (i)^2/10)*(f(i)-f(i-1));
```

```
65          %-(B(i,j)*dt)/(2*dr*h(i,j)*r(i))*(1-3*B(i,j)^2/10)*(f(i,j)-f
                (i-1,j))
66          end
67
68          if iRK==2
69              h =h*0.25+h_old*0.75;
70              f =f*0.25+f_old*0.75;
71              g =g*0.25+g_old*0.25;
72              B =B*0.25+B_old*0.25;
73          elseif(iRK==3)
74              h =h*(2/3)+h_old/3;
75              f =f*(2/3)+f_old/3;
76              g =g*(2/3)+g_old/3;
77              B =B*(2/3)+B_old/3;
78          end
79
80      end
81
82      if(mod(jTime,Nplot)==0)
83          plot(r,h,r,f,r,g*100,r,B);
84          title(['jTime=' num2str(jTime)])
85          legend('h','f','g*1000','B')
86          pause(0.1)
87
88          HH(jTime/Nplot,:)=h;
89          FF(jTime/Nplot,:)=f;
90          GG(jTime/Nplot,:)=g;
91          BB(jTime/Nplot,:)=B;
92      end
```

```
93
94 end
95
96
97
98 %FIGURE
99
100 % subplot(8,1,1);
101 % plot(r,GG(20,:));
102 % subplot(8,1,2);
103 % plot(r,GG(40,:));
104 % subplot(8,1,3);
105 % plot(r,GG(60,:));
106 % subplot(8,1,4);
107 % plot(r,GG(80,:));
108 % subplot(8,1,5);
109 % plot(r,GG(100,:));
110 % subplot(8,1,6);
111 % plot(r,GG(120,:));
112 % subplot(8,1,7);
113 % plot(r,GG(150,:));
114 % subplot(8,1,8);
115 % plot(r,GG(180,:));
```

Bibliography

[1] Hen-hong Chang and Evgeny A Demekhin. *Complex wave dynamics on thin films*, volume 14. Elsevier, 2002.

[2] Grigori M Sisoev, Omar K Matar, and Christopher J Lawrence. Modelling of film flow over a spinning disk. *Journal of Chemical Technology and Biotechnology*, 78(2-3):151–155, 2003.

[3] Hao Peng, Na Wang, Dongxiang Wang, and Xiang Ling. Experimental study on the critical characteristics of liquid atomization by a spinning disk. *Industrial & Engineering Chemistry Research*, 55(21):6175–6185, 2016.

[4] KVK Boodhoo and RJ Jachuck. Process intensification: spinning disk reactor for styrene polymerisation. *Applied Thermal Engineering*, 20(12):1127–1146, 2000.

[5] William Paul Woods. The hydrodynamics of thin liquid films flowing over a rotating disc. 1995.

[6] AF Charwat, RE Kelly, and C Gazley. The flow and stability of thin liquid films on a rotating disk. *Journal of Fluid Mechanics*, 53(02):227–255, 1972.

[7] AI Butuzov and II Puhovoi. On regimes of liquid film flows over a rotating surface. *J. Eng. Phys*, 31:217–224, 1976.

[8] A Aoune and C Ramshaw. Process intensification: heat and mass transfer characteristics of liquid films on rotating discs. *International Journal of Heat and Mass Transfer*, 42(14):2543–2556, 1999.

[9] Benoit Scheid, Christian Ruyer-Quil, and Paul Manneville. Wave patterns in film flows: modelling and three-dimensional waves. *Journal of Fluid Mechanics*, 562:183–222, 2006.

[10] Kamelia VK Boodhoo, William AE Dunk, Marija Vicevic, Roshan J Jachuck, Valerie Sage, Duncan J Macquarrie, and James H Clark. Classical cationic polymerization of styrene in a spinning disc reactor using silica-supported bf3 catalyst. *Journal of applied polymer science*, 101(1):8–19, 2006.

[11] Irina Boiarkina. *Investigation of a spinning disc as a thin film photocatalytic reactor for the degradation of recalcitrant wastewaters*. PhD thesis, ResearchSpace@ Auckland, 2013.

[12] Doris Prieling and Helfried Steiner. Unsteady thin film flow on spinning disks at large ekman numbers using an integral boundary layer method. *International Journal of Heat and Mass Transfer*, 65:10–22, 2013.

[13] Philip MJ Trevelyan, Serafim Kalliadasis, John H Merkin, and Stephen K Scott. Dynamics of a vertically falling film in the presence of a first-order chemical reaction. *Physics of Fluids (1994-present)*, 14(7):2402–2421, 2002.

[14] Philip MJ Trevelyan and Serafim Kalliadasis. Dynamics of a reactive falling film at large péclet numbers. i. long-wave approximation. *Physics of Fluids (1994-present)*, 16(8):3191–3208, 2004.

[15] Doris Prieling and Helfried Steiner. Unsteady thin film flow on spinning disks at large ekman numbers using an integral boundary layer method. *International Journal of Heat and Mass Transfer*, 65:10 – 22, 2013.

[16] Doris Prieling and Helfried Steiner. Analysis of the wall mass transfer on spinning disks using an integral boundary layer method. *Chemical Engineering Science*, 101:109 – 119, 2013.

[17] Isaac E Lagaris, Aristidis Likas, and Dimitrios I Fotiadis. Artificial neural networks for solving ordinary and partial differential equations. *IEEE Transactions on Neural Networks*, 9(5):987–1000, 1998.

[18] Grigori M Sisoev, Omar K Matar, and Chris J Lawrence. The flow of thin liquid films over spinning discs. *The Canadian Journal of Chemical Engineering*, 84(6):625–642, 2006.

[19] RV Craster and OK Matar. Dynamics and stability of thin liquid films. *Reviews of modern physics*, 81(3):1131, 2009.

[20] H Chang. Wave evolution on a falling film. *Annual review of fluid mechanics*, 26(1):103–136, 1994.

[21] Alexander Oron, Stephen H Davis, and S George Bankoff. Long-scale evolution of thin liquid films. *Reviews of modern physics*, 69(3):931, 1997.

[22] MRE Warner, RV Craster, and OK Matar. Fingering phenomena associated with insoluble surfactant spreading on thin liquid films. *Journal of Fluid Mechanics*, 510:169–200, 2004.

[23] Christophe Ancey. Plasticity and geophysical flows: a review. *Journal of Non-Newtonian Fluid Mechanics*, 142(1):4–35, 2007.

[24] Dambaru Raj Baral, Kolumban Hutter, and Ralf Greve. Asymptotic theories of large-scale motion, temperature, and moisture distribution in land-based polythermas fee sheets-a critical review and new developments. *Appl Mech Rev*, 54(3):215, 2001.

[25] Harris Wong, Irving Fatt, and CJ Radke. Deposition and thinning of the human tear film. *Journal of colloid and interface science*, 184(1):44–51, 1996.

[26] Omar K Matar, Chris J Lawrence, and Grigori M Sisoev. The flow of thin liquid films over spinning disks: Hydrodynamics and mass transfer. *Physics of Fluids (1994-present)*, 17(5):052102, 2005.

[27] Howard A Stone, Abraham D Stroock, and Armand Ajdari. Engineering flows in small devices: microfluidics toward a lab-on-a-chip. *Annu. Rev. Fluid Mech.*, 36:381–411, 2004.

[28] Jan CT Eijkel and Albert Van Den Berg. Nanofluidics: what is it and what can we expect from it? *Microfluidics and Nanofluidics*, 1(3):249–267, 2005.

[29] Philipp Adomeit and Ulrich Renz. Hydrodynamics of three-dimensional waves in laminar falling films. *International journal of multiphase flow*, 26(7):1183–1208, 2000.

[30] Christian Ruyer-Quil and Paul Manneville. Improved modeling of flows down inclined planes. *The European Physical Journal B-Condensed Matter and Complex Systems*, 15(2):357–369, 2000.

[31] V Ya Shkadov. Wave flow regimes of a thin layer of viscous fluid subject to gravity. *Fluid Dynamics*, 2(1):29–34, 1967.

[32] William M'F Orr. The stability or instability of the steady motions of a perfect liquid and of a viscous liquid. part ii: A viscous liquid. In *Proceedings of the Royal Irish Academy. Section A: Mathematical and Physical Sciences*, volume 27, pages 69–138. JSTOR, 1907.

[33] KJ Chu and AE Dukler. Statistical characteristics of thin, wavy films: Part ii. studies of the substrate and its wave structure. *AIChE Journal*, 20(4):695–706, 1974.

[34] Piotr Leonidovich Kapitza. Wave flow of thin viscous liquid films. iii. experimental study of wave regime of a flow. *J. Exp. Theor. Phys.*, 19(2):105–120, 1949.

[35] Serge Vladimirovich Alekseenko, Vladimir Eliferevich Nakoryakov, and Boris Grigorevich Pokusaev. *Wave flow of liquid films*. Begell House New York, 1994.

[36] Jun Liu, JB Schneider, and Jerry P Gollub. Three-dimensional instabilities of film flows. *Physics of Fluids*, 7(1):55–67, 1995.

[37] CD Park and T Nosoko. Three-dimensional wave dynamics on a falling film and associated mass transfer. *AIChE Journal*, 49(11):2715–2727, 2003.

[38] Arnold Sommerfeld. Ein beitrag zur hydrodynamischen erklaerung der turbulenten fluessigkeitsbewegungen. *Atti del*, 4:116–124, 1908.

[39] DJ Benney. Long waves on liquid films. *Studies in Applied Mathematics*, 45(1-4):150–155, 1966.

[40] V Ya Shkadov. Solitary waves in a layer of viscous liquid. *Fluid Dynamics*, 12(1):52–55, 1977.

[41] Waves induced by instability in falling films of finite thickness. *Fluid Dynamics Research*, 35(5):357 – 389, 2004.

[42] H-C Chang, EA Demekhin, and DI Kopelevich. Nonlinear evolution of waves on a vertically falling film. *Journal of Fluid Mechanics*, 250:433–480, 1993.

[43] L Kondic and J Diez. Pattern formation in the flow of thin films down an incline: Constant flux configuration. *Physics of Fluids*, 13(11):3168–3184, 2001.

[44] N. J. BALMFORTH, R. V. CRASTER, and R. SASSI. Shallow viscoplastic flow on an inclined plane. *Journal of Fluid Mechanics*, 470:1–29, 2002.

[45] Neil Balmforth, Shilpa Ghadge, and Tim Myers. Surface tension driven fingering of a viscoplastic film. *Journal of non-newtonian fluid mechanics*, 142(1):143–149, 2007.

[46] Hans Espig and Russell Hoyle. Waves in a thin liquid layer on a rotating disk. *Journal of Fluid Mechanics*, 22(04):671–677, 1965.

[47] Samson A Jenekhe and Spencer B Schuldt. Coating flow of non-newtonian fluids on a flat rotating disk. *Industrial & engineering chemistry fundamentals*, 23(4):432–436, 1984.

[48] JR Burns, C Ramshaw, and RJ Jachuck. Measurement of liquid film thickness and the determination of spin-up radius on a rotating disc using an electrical resistance technique. *Chemical engineering science*, 58(11):2245–2253, 2003.

[49] JR Burns and RJJ Jachuck. Determination of liquid–solid mass transfer coefficients for a spinning disc reactor using a limiting current technique. *International journal of heat and mass transfer*, 48(12):2540–2547, 2005.

[50] Clemens Brechtelsbauer, Norman Lewis, Paul Oxley, Francois Ricard, and Colin Ramshaw. Evaluation of a spinning disc reactor for continuous processing1. *Organic Process Research & Development*, 5(1):65–68, 2001.

[51] M Vicevic, K Novakovic, KVK Boodhoo, and AJ Morris. Kinetics of styrene free radical polymerisation in the spinning disc reactor. *Chemical Engineering Journal*, 135(1-2):78–82, 2008.

[52] KVK Boodhoo, WAE Dunk, MS Jassim, and RJ Jachuck. Thin film solvent-free photopolymerization of n-butyl acrylate. i. static film studies. *Journal of applied polymer science*, 91(4):2079–2095, 2004.

[53] M Vicevic, RJJ Jachuck, K Scott, JH Clark, and Karen Wilson. Rearrangement of α-pinene oxide using a surface catalysed spinning disc reactor (sdr). *Green Chemistry*, 6(10):533–537, 2004.

[54] Tae-Sung Kim and Moon-Uhn Kim. The flow and hydrodynamic stability of a liquid film on a rotating disc. *Fluid dynamics research*, 41(3):035504, 2009.

[55] OK Matar, GM Sisoev, and CJ Lawrence. Thin film flow over spinning discs: The effect of surface topography and flow rate modulation. *Chemical Engineering Science*, 63(8):2225–2232, 2008.

[56] V Ya Shkadov. Some methods and problems of the theory of hydrodynamic stability. In *Scientific Proceedings*, volume 25, 1973.

[57] GM Sisoev and V Ya SBKADOV. Development of dominating waves from small disturbances in falling viscous-liquid films. *Fluid dynamics*, 32(6):784–792, 1997.

[58] GM Sisoev, OK Matar, and CJ Lawrence. Axisymmetric wave regimes in viscous liquid film flow over a spinning disk. *Journal of Fluid Mechanics*, 495:385–411, 2003.

[59] Omar K Matar, Grigori M Sisoev, and Chris J Lawrence. Evolution scales for wave regimes in liquid film flow over a spinning disk. *Physics of Fluids*, 16(5):1532–1545, 2004.

[60] Omar K Matar and Chris J Lawrence. The effect of surfactant on the flow of a thin liquid film over a spinning disc. *Chemical engineering science*, 61(4):1074–1091, 2006.

[61] G Leneweit, KG Roesner, and R Koehler. Surface instabilities of thin liquid film flow on a rotating disk. *Experiments in Fluids*, 26(1-2):75–85, 1999.

[62] GM Sisoev, DB Goldgof, and VN Korzhova. Stationary spiral waves in film flow over a spinning disk. *Physics of Fluids (1994-present)*, 22(5):052106, 2010.

[63] Tejas J Bhatelia, Ranjeet P Utikar, Vishnu K Pareek, and Moses O Tade. Characterizing liquid film thickness in spinning disc reactors. In *Proceedings of the Seventh International Conference on CFD in the Minerals and Process Industries, CSIRO, Melbourne, Australia*, pages 9–11, 2009.

[64] B De Caprariis, M Di Rita, M Stoller, N Verdone, and A Chianese. Reaction-precipitation by a spinning disc reactor: Influence of hydrodynamics on nanoparticles production. *Chemical Engineering Science*, 76:73–80, 2012.

[65] Mohd Fadhil Majnis, Nurhazwani Yusoff Azudin, Syamsul Rizal Abd Shukor, and Abdul Latif Ahmad. A study on the mixing characteristics of thin liquid film flows over horizontal spinning disk surface. *Procedia Engineering*, 148:957 – 962, 2016. Proceeding of 4th International Conference on Process Engineering and Advanced Materials (ICPEAM 2016).

[66] I Tsibranska, D Peshev, G Peev, and A Nikolova. Modelling of mass transfer in film flow of shear thinning liquid on a horizontal rotating disk. *Chemical Engineering and Processing: Process Intensification*, 48(3):823–827, 2009.

[67] Y.-S. Park and S. Lek. Chapter 7 - artificial neural networks: Multilayer perceptron for ecological modeling. In Sven Erik Jørgensen, editor, *Ecological Model Types*, volume 28 of *Developments in Environmental Modelling*, pages 123 – 140. Elsevier, 2016.

[68] Asghar Esmaeeli and Grétar Tryggvason. A direct numerical simulation study of the buoyant rise of bubbles at o (100) reynolds number. *Physics of Fluids*, 17(9):093303, 2005.

[69] Martin Anton van der Hoef, M Ye, M van Sint Annaland, AT Andrews, S Sundaresan, and JAM Kuipers. Multiscale modeling of gas-fluidized beds. *Advances in chemical engineering*, 31:65–149, 2006.

[70] Jiacai Lu and Gretar Tryggvason. Dynamics of nearly spherical bubbles in a turbulent channel upflow. *Journal of Fluid Mechanics*, 732:166–189, 2013.

[71] Michele Milano and Petros Koumoutsakos. Neural network modeling for near wall turbulent flow. *Journal of Computational Physics*, 182(1):1–26, 2002.

[72] Elham Rajabi and Mohammad R Kavianpour. Intelligent prediction of turbulent flow over backward-facing step using direct numerical simulation data. *Engineering Applications of Computational Fluid Mechanics*, 6(4):490–503, 2012.

[73] F Sarghini, G De Felice, and S Santini. Neural networks based subgrid scale modeling in large eddy simulations. *Computers & fluids*, 32(1):97–108, 2003.

[74] S Moreau, D Neal, Y Khalighi, M Wang, and G Iaccarino. Validation of unstructured-mesh les of the trailing-edge flow and noise of a controlled-diffusion airfoil. In *Proceedings of the Summer Program*, page 1, 2006.

[75] Igor Esau. On application of artificial neural network methods in large-eddy simulations with unresolved urban surfaces. *Modern Applied Science*, 4(8):3, 2010.

[76] S Yarlanki, B Rajendran, and H Hamann. Estimation of turbulence closure coefficients for data centers using machine learning algorithms. In *Thermal and Thermomechanical Phenomena in Electronic Systems (ITherm), 2012 13th IEEE Intersociety Conference on*, pages 38–42. IEEE, 2012.

[77] Brendan Tracey, Karthik Duraisamy, and Juan J Alonso. A machine learning strategy to assist turbulence model development. *AIAA Paper*, 1287:2015, 2015.

[78] Eric J Parish and Karthik Duraisamy. A paradigm for data-driven predictive modeling using field inversion and machine learning. *Journal of Computational Physics*, 305:758–774, 2016.

[79] Anand Pratap Singh and Karthik Duraisamy. Using field inversion to quantify functional errors in turbulence closures. *Physics of Fluids*, 28(4):045110, 2016.

[80] Julia Ling, Reese Jones, and Jeremy Templeton. Machine learning strategies for systems with invariance properties. *Journal of Computational Physics*, 318:22–35, 2016.

[81] Masataka Gamahara and Yuji Hattori. Searching for turbulence models by artificial neural network. *Physical Review Fluids*, 2(5):054604, 2017.

[82] Christopher Lu. *Artificial neural network for behavior learning from meso-scale simulations, application to multi-scale multimaterial flows*. The University of Iowa, 2010.

[83] Oishik Sen, Sean Davis, Gustaaf Jacobs, and HS Udaykumar. Evaluation of convergence behavior of metamodeling techniques for bridging scales in multi-scale multimaterial simulation. *Journal of Computational Physics*, 294:585–604, 2015.

[84] Ming Ma, Jiacai Lu, and Gretar Tryggvason. Using statistical learning to close two-fluid multiphase flow equations for bubbly flows in vertical channels. *International Journal of Multiphase Flow*, 85:336–347, 2016.

[85] Ming Ma, Jiacai Lu, and Gretar Tryggvason. Using statistical learning to close two-fluid multiphase flow equations for a simple bubbly system. *Physics of Fluids*, 27(9):092101, 2015.

[86] Tatiana Gambaryan-Roisman, Martin Freystein, and Peter Stephan. Hydrodynamics and heat transfer in a liquid film flowing over a spinning disk with wall topography. *Heat Transfer Engineering*, 34(2-3):266–278, 2013.

[87] H Scott Fogler. *Essentials of Chemical Reaction Engineering: Essenti Chemica Reactio Engi*. Pearson Education, 2010.

[88] Geoffrey Frederick Hewitt, George L Shires, and Theodore Reginald Bott. *Process heat transfer*, volume 113. CRC press Boca Raton, 1994.

[89] Max Kuhn and Kjell Johnson. *Applied predictive modeling*, volume 810. Springer, 2013.

[90] Max Kuhn. A short introduction to the caret package. *URL: https://cran. r-project. org/web/packages/caret/vignettes/caret. pdf*, 2016.

[91] MATLAB. Neural network toolbox, 2017. *URL: https://www.mathworks.com/products/neural-network.htm*, 2017.